Université catholique de Louvain
Faculté des Sciences
Département de Physique
Unité de physique théorique et de physique mathématique
Centre for Particle Physics and Phenomenology

Top quark phenomenology at hadron colliders

Doctoral dissertation presented by

Rikkert Frederix

in fulfilment of the requirements for the degree of Doctor in Sciences

Prof. Fabio Maltoni (Adviser)	UCL
Prof. Denis Favart (Chairman)	UCL
Prof. Werner Bernreuther	RTWH Aachen
Prof. Jorgen D'Hondt	VUB Brussels
Prof. Stefano Frixione	EPFL Lausanne
Prof. Jean-Marc Gérard	UCL
Prof. Vincent Lemaître	UCL

September 2009

ABSTRACT

It has been almost fifteen years ago that the top quark, the heaviest and most intriguing among the six known quarks, was observed at the Tevatron experiments at Fermilab. Some of its properties, such as the mass and the production cross sections are by now quite well known. Other important aspects, however, such as the top quark invariant mass distribution, the structure of the tWb coupling, the single top cross sections, are still subject of an intense research activity. As more data will become available and with the start-up of the LHC more precise measurements will become possible. To compare the observed data with the Standard Model (SM) and to search for effects that cannot be explained within this theory, detailed predictions are needed.

In this thesis new measurements are proposed and improvements to existing predictions are presented. First, the top quark pair invariant mass distribution within the SM is studied as well as the effects of general "model independent" new physics resonances that affect this distribution. Second, a method to set model independent bounds on the third row of the CKM matrix is proposed based on both indirect and direct measurements. Third, a new next-to-leading order prediction for t-channel single top cross section is presented in detail that allows for the first time to describe reliably some key features of the production mechanism.

ACKNOWLEDGEMENTS

First and foremost I would like to thank my supervisor, Fabio Maltoni, for making my Ph.D. such an enjoyable experience. His unstoppable optimism and enthusiasm has been very inspiring. His office has always been open, ready to step in to ask any questions. I am indebted to him for showing how Monte Carlo's are supposed to work and improved, and more importantly, how they can be used to make detailed predictions for high energy particle physics experiments. I would also like to thank him for encouraging me to work with external collaborators, to give talks at international workshops and conferences and for sending me to CERN. It truly showed me how international this field of research is and helped me to get recognition from many colleagues.

I would also like to thank Stefano Frixione for being my adviser during my year at CERN. I have learned a lot from him about fixed order QCD calculations and how to write a proper computer code. His professional way of working, with clear goals and a quick working pace, meant that we could get a lot of work done.

The other members of the jury of my thesis, Denis Favart, Werner Bernreuther, Jorgen D'Hondt, Jean-Marc Gérard and Vincent Lemaître, deserve a thank you too for showing, among other things, that there is still much to learn and study even after having completed this thesis.

Furthermore I would also like to thank my other collaborators. Thanks, John Campbell and especially Francesco Tramontano, for spending many hours explaining me how to do a complicated NLO computation. Thank you, Massimiliano Grazzini, for helping with resumming large logarithms. Also many thanks to you, Thomas Gehrmann and, in particular, Nicolas Greiner for discussing all about the dipoles. Also, a great thank you to all the members of the MadGraph team.

I owe a thank you to all my friends at the CP3 institute who have made my time in Belgium so much more enjoyable. In particular to Claude (for being such a fantastic office mate), Simon (for always being ready to help), Christophe (for the many snooker evenings), Antonio (for all non-physics related discussions), Keith (for all our discussions), Vincent (for the many times we played cards) and Pierre (for helping out with all the little things). If it weren't for you guys, I wouldn't have had such a great time in Louvain. Also thanks Andy, Ben, Bob, Jeppe and Jure for having all the lunches and afternoon coffees at the CERN canteen together.

I am also grateful for the CP3 and CERN hospitality, Pavel and the IT staff for the computing support and the CP3 secretaries, Cathy, Carine and Ginette, for their help with all practical matters.

Als laatste wil ik graag mijn ouders, Fried en Lily, en broers, Floris en Gijs, en Lonneke bedanken voor hun steun en hulp bij weer een verhuizing...

CONTENTS

1 Introduction **1**

1.1 Top quarks in the Standard Model 3

1.1.1 The need for the top quark 5

1.2 Top quark production in the Standard Model 7

1.2.1 Top quark pair production 7

1.2.2 Single top quark production 10

1.3 Top quarks relation to BSM physics 12

1.3.1 Weakly coupled models at the TeV scale 13

1.3.2 Strongly coupled models at the TeV scale 14

1.3.3 New space-time structures 14

1.3.4 Other models 15

2 Top quark pair invariant mass **17**

2.1 Theoretical uncertainties in the top quark pair invariant mass . 18

2.2 Top quark mass dependence 22

2.2.1 Threshold effects 29

2.3 Effects from BSM resonances 31

2.3.1 Spin-0 resonances 32

2.3.2 Spin-1 resonances 37
2.3.3 Spin-2 resonances 40
2.4 Spin information from (anti-)top quark directions 42
2.4.1 Standard Model 43
2.4.2 Spin-0 resonances 44
2.4.3 Spin-1 resonances 44
2.4.4 Spin-2 resonances 46
2.5 Spin correlations in (anti-)top-quark decays 46
2.6 Non-resonant BSM effects 49
2.6.1 Invisible (pseudo-)scalar 51
2.6.2 $pp \to \tilde{t_1}\bar{\tilde{t}_1} \to t\bar{t}\tilde{\chi}_1^0\tilde{\chi}_1^0$ 55
2.7 Reconstruction issues in $t\bar{t}$ events 57
2.8 Conclusions 59

3 Constraints on the CKM matrix 61
3.1 Introduction 61
3.2 Minimal New Physics models with extended CKM matrices . . 62
3.2.1 Vector-like t' 62
3.2.2 Fourth generation 64
3.3 Direct constraints on $|V_{tb}|$ 64
3.3.1 Top quark decay 65
3.3.2 Single top production 65
3.4 Bounds on $|V_{tb}|$ from direct measurements 67
3.5 Discussion 70

4 t-channel single top at NLO 71
4.1 Born contributions 73
4.2 NLO corrections 74

4.3 Real corrections 74
4.3.1 Interference between t- and s-channel diagrams 75
4.3.2 Interference with W associated single top production . . 76
4.3.3 Interference between heavy and light quark lines 76
4.4 Virtual corrections 77
4.4.1 Dimensional reduction 79
4.4.2 Renormalization of UV divergences 79
4.4.3 Finite renormalization from γ_5 in the coupling 81
4.4.4 Scalar integrals 84
4.4.5 Top quark decay 84
4.5 Subtraction terms 85
4.5.1 Dipole subtraction 85
4.6 Checks of the calculation 86
4.7 Comparison $2 \to 2$ with $2 \to 3$ 87
4.7.1 PDF sets 87
4.7.2 Total cross section and scale dependence 88
4.7.3 Differential distributions 93
4.8 From SM single top to a fourth generation 101
4.8.1 tb' and $t'b'$ cross sections and uncertainties 109
4.9 Conclusions 110

5 Conclusions **115**
5.1 Outlook 117

Appendices

A Automation of the dipole subtraction for NLO computations 119

A.1 Construction of dipole terms 121

A.1.1 Color and helicity management 121

A.1.2 Massive particles 122

A.1.3 Phase space restriction 123

A.2 Checks 125

A.3 Conclusions 131

B t-channel single top and fourth generation quarks 133

CHAPTER

ONE

INTRODUCTION

The discovery of the τ lepton at SLAC-LBL in 1975 [1] was the first evidence for the existence of a third generation of fundamental fermions. Just two years later at Fermilab with the discovery of the bottom quark [2] the extension of the third generation into the quark sector was established. Due to symmetry considerations this immediately raised the question of the existence of a weak isospin partner of the bottom quark: the top quark.

Within the Standard Model (SM) of elementary particle physics the existence of the top quark is a necessity for the self-consistency of the Model. Electroweak precision measurements, mainly from the LEP experiments at CERN, allowed for the prediction of the mass of the top quark and just before the direct observation its mass was constrained to $178 \pm 11^{+18}_{-19}$ GeV [3].

In 1995 the top quark was finally discovered by the CDF and DØ collaborations at Fermilab [4, 5] in the mass range predicted by the Standard Model. This demonstrated the predictive power of the Standard Model and completed it up to the elusive Higgs boson, the remnant of the mechanism of electroweak symmetry breaking. Now, the mass has been measured with a precision better than 1%, $m_{\text{top}} = 172.4 \pm 1.2$ GeV [6], making it the heaviest fundamental particle known to date. Due to its heavy mass the lifetime of the top quark, which is determined by the weak interactions, is extremely small, approximately $5 \cdot 10^{-25}$ s. This is shorter than the hadronization time, making it impossible for the top quark to form bound states. On the other hand, it gives us a handle to study of bare quarks, unperturbed by hadronization.

Although the top quark mass is very well measured by the two Tevatron experiments, information on other aspects, such as the top quark pair invariant mass distribution, W boson helicity in its decay, the structure of the tWb coupling, etc., are open to much improvements. With time more data at the Tevatron should become available and with the start-up of the LHC more precise measurements will become possible allowing for a better comparison with SM predictions, and for possible effects from "new" physics. In particular, the large top quark mass, very close to the scale of electroweak symmetry breaking (EWSB), $m_{\text{top}} \simeq v/\sqrt{2}$, implies a naturally strong coupling, $\lambda_{\text{top}} \simeq 1$, to the Higgs boson and therefore might suggest a special role within the Standard Model and in models beyond: it is because of this large coupling that the Higgs boson mass can be predicted via precision measurements, and the Higgs boson can be copiously produced at hadron colliders operating at the TeV scale, via its top quark-loop mediated interactions to gluons. Furthermore, thanks to its large mass, the top quark has also been exploited in many scenarios that go beyond the Standard Model (BSM). The simplest one is SUSY, where top has the important role of triggering EWSB and the historical merit of having escorted the MSSM to the LHC era by allowing the Higgs boson mass to survive the LEP bounds.

Very recently also "single" top quark production has been observed [7,8]. Contrary to top quark pair production, which is governed by the strong interaction at hadron colliders, single top quarks are produced by the electroweak interaction. This allows for the first time to directly measure the CKM element $|V_{tb}|$.

Apart from the introduction and appendices this thesis is divided into three main sections. The first part is about top quark pair production. Here we discuss the $t\bar{t}$ invariant mass distribution and how beyond the Standard Model physics resonances could affect this distribution. We will describe a three step analysis that could allow a discovery and establish the quantum numbers of these new states. In Chapter 3 the direct measurement of the CKM matrix element V_{tb} is discussed. In the fourth chapter the calculation and results of the NLO predictions in t-channel single top quark production are outlined in detail. Besides these three main parts, the conclusions and outlook can be found in Chapter 5 and in the appendix A a tool, `MadDipole`, that we have developed to automate the subtracted real emission part of any QCD NLO computation, is presented. But we start with a review of the top quark within the SM in the next sections.

The work presented in the thesis is based on the following publications:

- R. Frederix and F. Maltoni, "Top pair invariant mass distribution: a window on new physics," *JHEP* **01** (2009) 047 [arXiv:0712.2355 [hep-ph]]
- J. Alwall *et. al.*, "Is $V_{tb} \simeq 1$?," *Eur. Phys. J.* **C49** (2007) 791–801 [hep-ph/0607115]
- J. M. Campbell, R. Frederix, F. Maltoni and F. Tramontano, "t-channel single top production at hadron colliders," *Phys. Rev. Lett.* **102** (2009) 182003 [arXiv:0903.0005 [hep-ph]]
- J. M. Campbell, R. Frederix, F. Maltoni and F. Tramontano, "NLO predictions for t-channel production of single top and fourth generation quarks at hadron colliders," arXiv:0907.3933 [hep-ph]
- R. Frederix, T. Gehrmann and N. Greiner, "MadDipole: automation of the dipole subtraction method in MadGraph/MadEvent," *JHEP* **09** (2008) 122 [arXiv:0808.2128 [hep-ph]]

and the conference proceedings, Ref. [9].

1.1 Top quarks in the Standard Model

The Standard Model of particle physics describes very successfully almost all available data in elementary particle physics. The Standard Model includes the fundamental constituents of matter, fermions (or spin-1/2 particles) and their fundamental interactions, mediated by gauge bosons (or spin-1 particles). The fermions in the Standard Model can be put in two groups: the leptons and the quarks. Both the quarks and the leptons are subdivided into three generations, which show a strong hierarchy in mass. The top quark, which is the heaviest fundamental particle known so far, belongs to the third generation, together with the bottom quark and the tau and tau-neutrino leptons.

In the SM the interactions between particles are mediated by gauge bosons, eight massless gluons mediate the strong force, while the electroweak force is mediated by photons and the massive W and Z bosons. Quarks, contrary to leptons, are charged under the $SU(3)_{\mathrm{QCD}}$ color charge and are therefore affected by the strong interaction. A remarkable feature of the strong coupling, known as asymptotic freedom, is that it is very strong at relatively large distances, but gets weaker at larger relative momenta (or small distances). This allows for a perturbative treatment of the color interactions at high momenta

transfers, while at larger distances quarks form bound states, a process called hadronization, which cannot be described by perturbative physics.

Besides the strong interaction, quarks are also charged under the electroweak interaction, based upon the gauge group $SU(2)_{\mathrm{L}} \times U(1)_{\mathrm{Y}}$. Only the left-handed fermions are charged under the $SU(2)_{\mathrm{L}}$ weak isospin gauge group which naturally groups the fermions into two classes: the right-handed components of the fermions that are singlets under the $SU(2)_{\mathrm{L}}$ gauge group, and the left-handed fermion components that are grouped into doublets. The left-handed component of the top quark is grouped together with its weak isospin partner, the bottom quark in a doublet as the upper component. In the doublets the up-type quarks (and the neutrinos in the lepton sector) carry weak isospin charge $T_3 = +\frac{1}{2}$ and the lower components $T_3 = -\frac{1}{2}$. The hyper-charge Y which is transformed under the gauge group $U(1)_{\mathrm{Y}}$, is defined via the weak isospin and the electric charge Q_f, as $Y = 2Q_f - T_3$.

The decay of the top quark is governed by the electroweak interactions and is at leading order (LO) equal to $\Gamma_t = \frac{G_F}{8\pi\sqrt{2}}|V_{tb}|^2 m_{\mathrm{top}}^3 \left(1 + \mathcal{O}(m_W^2/m_{\mathrm{top}}^2)\right)$. Because the top quark is very heavy and the decay width scales like m_{top}^3 its decay width is large and therefore its life-time short. In fact, if we put the numerical values for its mass and couplings, we find that the scale at which QCD hadronization occurs ($\Lambda_{\mathrm{QCD}} \approx 200$ MeV) is smaller than the top quark decay width,* $\Lambda_{\mathrm{QCD}} \ll \Gamma_{\mathrm{top}} \approx 1.5$ GeV. This means that, contrary to all other quarks, the top quark does not form bound states: its life-time is shorter than the time it takes to form a hadron ($\tau_{\mathrm{top}} = \Gamma_{\mathrm{top}}^{-1} < \tau_{\mathrm{had}} = \Lambda_{\mathrm{QCD}}^{-1}$). Therefore the top quark offers the unique opportunity to the study properties of (bare) quarks.

Within the $SU(2)_{\mathrm{L}} \times U(1)_{\mathrm{Y}}$ gauge group, masses for the gauge bosons are not allowed. However, the masses of the W and Z bosons, that mediate the electroweak force, are non-zero. The minimal mechanism to accommodate for the masses of these gauge bosons, the so-called Brout-Englert-Higgs mechanism, allows for the "breaking" of this gauge group. By introducing a scalar doublet under $SU(2)_{\mathrm{L}}$ of which one of the components has a non-zero vacuum expectation value the $SU(2)_{\mathrm{L}}$ symmetry is no longer exact: the vacuum fails to obey the symmetry, and therefore all the states built in this space inherit this failure. The $SU(2)_{\mathrm{L}} \times U(1)_{\mathrm{Y}}$ gauge group is broken to the $U(1)_{\mathrm{QED}}$ giving mass to the W and Z gauge bosons, while keeping the photon massless. This removes three degrees of freedom from the scalar doublet, leaving the final one to be the Higgs boson.

*This relies on the Standard Model expectation for the value of $|V_{tb}|^2$. Direct measurements still allow for a significantly smaller value of V_{tb}, as we will show in Chapter 3.

Via the Yukawa coupling of the Higgs doublet to the fermions, the vacuum expectation value gives also masses to these particles, $m_f = \lambda_f v/\sqrt{2}$. In particular, to explain the large top quark mass the coupling of the top quark to the Higgs boson has to be of order unity ($\lambda_{\text{top}} = \sqrt{2}m_{\text{top}}/v \approx \sqrt{2}\,173/246 \approx 0.99$), which might suggest a special role of the top quark in electroweak symmetry breaking.

A final ingredient to the Standard Model that is relevant to top quark physics is the relation of fermion mass eigenstates to electroweak eigenstates. The mass states are not eigenstates under electroweak current, but mix under the charged current which is described by the 3×3 CKM matrix. Out of the nine complex arguments of this matrix only four parameters are independent, three mixing angles and one phase, of which the latter one is the only measured source for CP violation in the Standard Model. By convention, the CKM matrix operates on the lower components of the $SU(2)_{\text{L}}$ doublets mass eigenstates,

$$\begin{pmatrix} d' \\ s' \\ b' \end{pmatrix}_{\text{L}} = V_{\text{CKM}} \begin{pmatrix} d \\ s \\ b \end{pmatrix}_{\text{L}} = \begin{pmatrix} V_{ud} & V_{us} & V_{ub} \\ V_{cd} & V_{cs} & V_{cb} \\ V_{td} & V_{ts} & V_{tb} \end{pmatrix} \begin{pmatrix} d \\ s \\ b \end{pmatrix}_{\text{L}} \tag{1.1}$$

and relates them to the electroweak eigenstates. Because the matrix has off-diagonal terms the charged W boson interactions mix the three generations, *e.g.*, a top quark decays not only to a bottom (and a W boson), but there is also a fraction of top quarks decaying to down and strange quarks.

1.1.1 The need for the top quark

Besides the firm proof of the direct observation of the top quark, there are two main reasons for the need of a top quark in the Standard Model. The first reason is to keep the Standard Model a renormalizable theory. One necessity for the renormalizability of a theory is to have it free from chiral "anomalies". In this context anomalies can be regarded as symmetries that are true at the classical (or "tree") level, but break down at the quantum (or "loop") level. The axial anomaly, related to the break down of the conservation of the axial vector current when going from the classical to the quantum theory, can be expressed by triangle diagrams such as the one depicted in Fig. 1.1. The interaction between the two photons and the axial vector boson[†] should vanish when all contributions are included, *i.e.*, when summed over all possible fermions in the loop.

[†]In the Standard Model the axial vector boson could, *e.g.*, be the axial part of the Z boson.

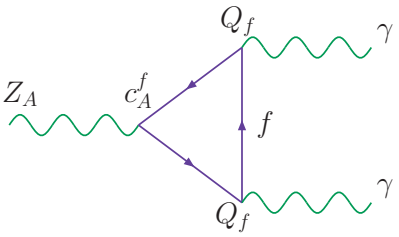

Figure 1.1: A diagram sensitive to the axial anomaly.

The contribution from each diagram is proportional to the coupling $c_A^f Q_f^2$, where c_A^f is the axial current coupling strength to the fermion f in the loop and Q_f is the coupling of the photon to that fermion. The axial current coupling is equal to the weak isospin charge $c_A^f = T_3$, *i.e.*, $+\frac{1}{2}$ and $-\frac{1}{2}$ for up and down type fermions of doublets and $+1$ for singlets under the SU(2) symmetry. The coupling of the photon is equal to the electric charge. After summing over all fermions the diagram in Fig. 1.1 gives a total contribution proportional to

$$\sum_{N_{\text{families}}} \left(-\frac{1}{2}(-1)^2 + \frac{1}{2}N_c\Big(\frac{2}{3}\Big)^2 - \frac{1}{2}N_c\Big(\frac{-1}{3}\Big)^2 \right), \tag{1.2}$$

where the first contribution is coming from the leptons, the second from the up-type quarks and the third from the down-type quarks. $N_c = 3$ is the number of colors. We see that only if the number of families for the leptons and the quarks are equal that the above expression gives zero. Consequently, the discovery of the third lepton generation already called for a third family in the quark sector of the Standard Model to keep a renormalizable theory.

The second reason comes from the measurement that the b quark is not singlet under the weak transformation. It is part of a doublet with weak isospin $T_3 = -\frac{1}{2}$ and electric charge $Q_b = -\frac{1}{3}$. The forward backward asymmetry for the number of fermions produced in the forward and backward regions in the detector via the process $e^+e^- \to b\bar{b} \to \mu^\pm$+hadrons originates from electroweak interference effects and is a measurement of the weak isospin. The measurement, performed at the JADE detector at PETRA in 1984 [10], confirmed that the b quark is not an isospin singlet, and needs an isospin partner.

These two arguments predicted the existence of the top quark well before its discovery in 1995, but gave no indication what its mass was.

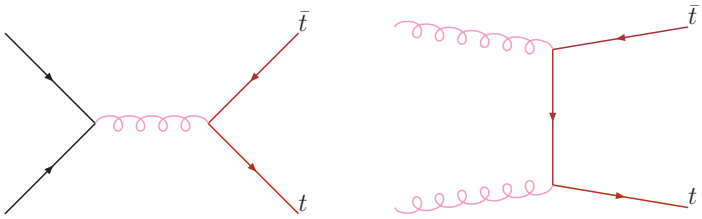

(a) (b)

Figure 1.2: Representative LO top quark pair production diagrams for the (a) quark–anti-quark annihilation and (b) gluon fusion channels.

1.2 Top quark production in the Standard Model

In hadron collisions top quarks can be produced with the strong interaction in pairs, or singly via the electroweak interaction.

1.2.1 Top quark pair production

Due to the large coupling strength of QCD the main production mechanism of top quarks at the Tevatron and LHC is by pair production. In Fig. 1.2 representative leading order diagrams are depicted for quark–anti-quark annihilation (a) and gluon fusion (b).

At the Tevatron the top quark pairs are in about 85% of the cases produced by the quark–anti-quark annihilation channel, with the rest through gluon-gluon fusion.[‡] At the LHC it is the opposite: it is predicted that top quark pairs are in almost 90% of time produced by gluon fusion. The two reasons for this is that the Tevatron is a proton–anti-proton collider, and therefore the quark–anti-quark luminosities are greater compared to a proton–proton collider, like the LHC. Furthermore, compared to the LHC the production of top quark pairs at the Tevatron requires much higher x's, *i.e.*, the fraction of the hadrons' energies carried by the partons in the interaction. For large x's the (anti) quark luminosities are of greater importance compared to the gluon luminosities because they drop much more rapidly with increasing x.

[‡]Beyond leading order there is also a small fraction of events produced by one initial state (anti) quark and one gluon. This is of no relevance here and will not be discussed further.

Theoretical status of top pair production

The first fixed NLO in QCD corrections to the tree level heavy quark pair hadro-production were performed more than 20 years ago by Nason et al. [11] and Beenakker et al. [12,13]. The inclusion of the threshold logarithms [14–16], which can become sizable close to the kinematic threshold ($\hat{s} \approx 4m^2$, *i.e.*, $x \to 1$) is a refinement, which was studied by various groups in the context of top quark pair production up to leading logarithmic (LL) accuracy [17–23]. In 2003 Cacciari et al. [24,25] gave updated predictions including also the next-to-leading logarithms (NLL) based on the work first presented in Ref. [26]. Since the contributions from these large logarithms are positive in the phase space region where they are important the inclusion of these logarithmic terms to all orders increases the cross section.

Even though the top pair production is relatively close to threshold at the Tevatron, the inclusion of the threshold resummation logarithms affects the total cross section only mildly by ($\sim 5\%$). However, the predictions are more stable under scale variations, going down from roughly 10% at NLO to $\pm 5\%$ at NLO plus NLL [24, 26] which suggests that including even higher order terms will have only a small effect in the prediction of the cross section. Very recently also updated predictions for the LHC were given, using the same NLO plus NLL approximation [25]. Because at the LHC top pair production is further away from threshold, including the resummed threshold logarithms increases the total cross section by only 3%. Furthermore, the reduction in the scale dependence is also very mild: it goes down from ($\sim 12\%$) at NLO to 9% at NLO plus NLL.

A different approach in resumming threshold logarithms has been pursued by Kidonakis et al. [27–31] and in joint resummation by Banfi et al. [32]. Recently, Moch and Uwer [33] have performed a complete NNLL soft gluon resummation and used this formalism to provide an approximation of the NNLO cross section. It has been found that the approximate NNLO cross section has a very small scale dependence: of the order of 3% for the Tevatron and similarly for the LHC. However, in this study the renormalization and factorization scales were not varied independently, which might be an underestimate of the total dependence. Furthermore, because this approximate NNLO computation was obtained by including only NNLL threshold logarithms and terms depending on the renormalization and factorization scales, the left-over scale dependence might underestimate the true uncertainty. The inclusion of more NNLO terms could easily lead to a prediction for the total cross section outside their current quoted uncertainty bound.

For a top mass of 171 GeV the predictions for the total cross section of top pair production at the Tevatron runII ($\sqrt{s} = 1.96$ TeV) and the LHC ($\sqrt{s} = 14$ TeV) have been summarized in Table 1.1, using the `MRST2006NNLO` PDF sets [34].

Besides the QCD corrections to on-shell top quark pair production summed over their spins, there are four more classes of corrections that have been computed. First there are the NLO QCD corrections by Bernreuther et al. that take the top and anti-top spin degrees of freedom fully into account [35, 36]. This provides azimuthal correlations between the decay products of the top quark at NLO in QCD. Second, the mixed QCD and EW corrections have been computed by Kühn et al. [37] and Bernreuther et al. [38] in 2006. The effects of the EW corrections are negative, however small for the total cross section, but have some effect on shapes of distributions. Third, the non-factorizable QCD corrections between production and decay, *i.e.*, corrections of order $\alpha_s \Gamma_t / m_t$, are known [39]. Fourth, the NLO QCD predictions have also been interfaced in a consistent way to parton shower programs by Frixione et al. in the `MC@NLO` code [40] and the `POWHEG` framework [41].

These precise predictions for the total cross section allows for a consistency test of the Standard Model and perturbation theory at high accuracy. Also, top quark pair production is a major background to other processes, in particular to the single top channels that are discussed in the next section. A precise determination of the top quark pair production channel is needed to reduce it as a background and allow for a clean measurement of the single top channels.

	Tevatron $\sqrt{s} = 1.96$ TeV (in pb)	LHC $\sqrt{s} = 14$ TeV (in pb)
Cacciari et al. [25]	$7.93^{+0.34}_{-0.56}$	961^{+89}_{-91}
Kidonakis and Vogt [31]	$8.06 \pm 0.32^{+0.03}_{-0.28}$	$994 \pm 5^{+81}_{-52}$
Moch and Uwer [33]	8.11 ± 0.21	949 ± 20

Table 1.1: Predictions for the total top pair production cross section using $m_t = 171$ GeV and the `MRST2006NNLO` PDF set with scale uncertainties and "kinematics" uncertainties for the predictions by Kidonakis et al. For more details we refer the reader to the corresponding Refs.

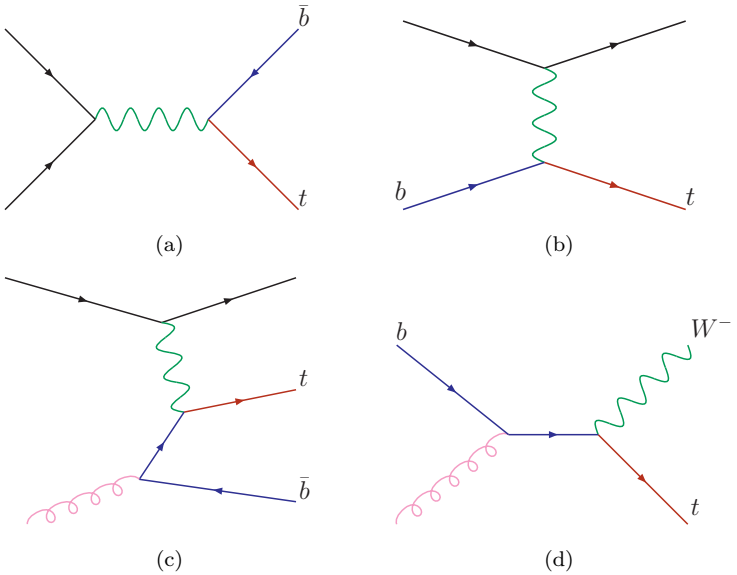

Figure 1.3: Representative LO single top production diagrams for the (a) s channel, (b) and (c) t channel in the five and four flavor schemes and (d) Wt associated production (in the five flavor scheme).

1.2.2 Single top quark production

There are three distinct ways for top quarks not to be produced in pairs. All three are governed by the electroweak interaction that relies on the flavor changing coupling of the W boson that changes a bottom quark into a top quark. In Fig. 1.3 representative diagrams for the three production mechanism are depicted.[§] All three channels are proportional to the CKM matrix element $|V_{tb}|^2$ and therefore a measurement of any of these single top production cross sections is a direct measurement of this CKM matrix element. In Chapter 3 this is discussed in more detail.

t-channel single top production Both at the Tevatron and the LHC the t-channel production is the largest of these three production mechanisms, Fig. 1.3(b), (c). Naively one would expect that a production process through the electroweak interaction is considerably smaller than a process through the strong interaction. However, due to the sizable gain in phase space for single top production and the t-channel enhancement at high

[§]Beyond leading order there exist some interference effects between the three production channels. However, this interference is in general color suppressed and does not spoil the distinction in most phenomenological studies.

energies due to the W boson [42–44], t-channel single top production is only about a factor three smaller than $t\bar{t}$ production, about 2 pb at the Tevatron and 240 pb at the LHC, summing both the top and anti top production cross sections.

The initial state b quark can be treated in two distinct ways. In the usual five flavor scheme, Fig. 1.3(b), it is considered to be a part of the proton, with its luminosity described by a PDF set. In this treatment the initial state b quark is considered massless at leading order. Its mass enters in (some of) the higher order corrections, in particular when the bottom quark is not an initial state particle. On the contrary, in the four flavor scheme the mass of the b quark is taken to be non-zero already at leading order, and the bottom quark is unsuitable for a description by a PDF set. In particular the b quark has to come from a gluon splitting into a $b\bar{b}$ pair. At lowest order this leads to a $2 \to 3$ process, as can be seen in Fig. 1.3(c). We will discuss this issue in more detail in Chapter 4 where we present the NLO corrections to this channel in the four flavor scheme.

s-channel single top production At the Tevatron s-channel single top production, Fig. 1.3(a), is the second largest with a sizable cross section of about 0.8 pb [45, 46]. Because there is no t-channel enhancement, the cross section at the LHC is only about a factor 10 larger. Furthermore, because at LHC energies the process is dominated by partons from the proton sea, there is no enhancement relative to other channels, which makes it challenging to distinguish it from backgrounds. This makes the Tevatron the most natural place to study s-channel single top events in the (near) future.

Out of the three production mechanisms it is believed that the total cross section for the s channel is under best theoretical control. It is very similar to Drell-Yan heavy vector boson production and quantum corrections are believed to be under excellent theoretical control.

Wt associated production The Wt associated production mechanism, see Fig. 1.3(d) [47,48], is of no relevance at the Tevatron due to the low gluon luminosity and the lack of phase space to produce both a top quark and a W boson. At the LHC where the gluon luminosity is much larger this process can play a significant role and has a cross section of the order of 70 pb.

The cross section for Wt production has the same problem as the t-channel production. Also here there is a b quark in the initial state in the five flavor scheme. However, there is a more important issue with the

correct definition of the Wt cross section. At NLO and beyond there is potentionally a large interference with top quark pair production. Therefore the total inclusive cross section for Wt production is not a well-defined quantity. However, with some simple analysis cuts to remove part of the $t\bar{t}$ background, also the interference can be suppressed and a practical definition for the cross section exists for studies involving searches for Wt production [49–51].

For all the three channels there has been an intense activity in the last fifteen years to provide more precise predictions at NLO accuracy. Calculations have progressed from evaluations of total rates [52, 53], to differential distributions [30, 54], including spin correlations in production and decay [49, 55–57] and finally to the implementation of the three production channels in a fully exclusive Monte Carlo program [50, 58]. In Chapter 4 we report on the latest improvement in this series of increasingly-sophisticated predictions, *i.e.*, the NLO corrections to the t-channel production mechanism in the four flavor scheme [59].

1.3 Top quarks relation to BSM physics

As stated before, the top quarks large mass close to the electroweak symmetry breaking scale (EWSB) suggest that it has a special role in the breaking. In particular the hierarchy problem in the stabilization of the Higgs boson mass, is significantly affected due to the large top quark mass. Due to its large mass the contribution from the top quark is the largest[¶] in the one-loop radiative corrections to the Higgs boson mass,

$$m_H^2 = (m_H^0)^2 + \frac{3\Lambda_{\rm UV}^2}{8\pi^2 v^2}\Big(-4m_t^2 + 2m_W^2 + m_Z^2 + m_H^2\Big) \tag{1.3}$$

The bare Higgs boson mass squared, $(m_H^0)^2$, has to be tuned in such a way that, together with the contributions from the top, the EW bosons and the Higgs boson itself, it gives a value for the Higgs boson mass m_H that is consistent with all the indirect electroweak constraints. Which means a Higgs boson m_H lighter than 200 GeV or so. In this relation $\Lambda_{\rm UV}$ is a UV cut-off scale in energy above which the Standard Model is no longer valid. If we believe that the Standard Model is valid up to the order of the Planck scale $\Lambda_{\rm UV} \sim M_{\rm Planck}$, *i.e.*, the scale at which we *know* that the Standard Model is no longer a valid description of nature, the one-loop corrections to the Higgs boson mass are some 30 orders

[¶]For a very heavy Higgs boson, the contributions from the Higgs boson itself are dominant.

of magnitude above the value that is consistent with experiments. This implies that the bare Higgs boson mass, m_H^0, is of the same magnitude to get an almost perfect cancellation between the extremely large quantum corrections and the bare Higgs boson mass.

Due to the fact that numerically the largest contributions to these quantum corrections are from the top quark, the top quark plays a natural role in new physics models that try to relieve this fine tuning. These models can be classified in three groups.

1.3.1 Weakly coupled models at the TeV scale

The idea of models that fall into this category introduce new particles with electroweak couplings that cancel the large contributions to the Higgs boson mass corrections present in the Standard Model.

The most popular example of such a solution is supersymmetry. Introducing a supersymmetry to the SM forces each particle to have a supersymmetric partner of opposite statistics, but with all other quantum numbers and masses unaltered. This leads to a natural solution of the hierarchy problem because the radiative corrections to the Higgs boson mass due to the superpartners have opposite sign and cancel exactly the contributions from the SM particles.

However, as no superpartners have been observed, supersymmetry cannot be exact and must be broken. This breaking entails a difference in running of the masses of the SM particles and their supersymmetry partners from the supersymmetry breaking scale down to lower scales, which leads to different masses at low scales. However, to have only a mild fine tuning, the superpartner of the top quark cannot be extremely heavy and must be "around the corner".

The other class of models that fall into this category are so-called Little Higgs models. The idea behind Little Higgs models is to solve the fine tuning problem of the Higgs boson mass by considering the Higgs boson as a pseudo-Nambu-Goldstone boson of a broken symmetry [60–67]. This is very similar to the pion in QCD, where it is considered to be the Goldstone boson of the spontaneously broken (global) chiral symmetry. Enlarging the symmetry group entails the need for more particle states of which one should cancel the large contribution from the top quark in the radiative corrections to the Higgs boson mass. In general, a heavy vector-like top quark, T, is introduced whose couplings interplay neatly with the SM couplings to cancel the top quark contributions. The mass of this fermionic state should not be too far from the top quark mass to

solve the fine tuning problem and therefore it should be accessible by direct searches at the LHC.

1.3.2 Strongly coupled models at the TeV scale

Models that fall into this category introduce new strong dynamics at the TeV scale. Typical examples are, *e.g.*, "Topcolor" in which the EWSB in the Standard Model is a dynamical mechanism involving a top quark condensate, $\langle t\bar{t}\rangle$, of a new fundamental strong interaction preferentially coupling to the third generation [68]. However, without fine-tuning, this model predicts a too large top quark mass and refinements are needed.

In "Topcolor assisted technicolor" the top quark mass is a combination of a small *fundamental* component generated by an (extended) technicolor mechanism, and a large *dynamical* mass component generated by topcolor dynamics. The technicolor component allows us to relax the necessity that the top quark condensate triggers all the EWSB and therefore predicts a smaller top quark mass compared to pure topcolor models [69–71].

In topcolor see-saw models the QCD gauge group is embedded in a larger gauge group. Due to mixing with another electroweak singlet the top quark mass can be "see-sawed" down to the experimental value [72–74].

The gauge bosons of such new topcolor symmetries couple preferentially to the third generation, which means that they could show up as resonances in $b\bar{b}$ or $t\bar{t}$ production.

1.3.3 New space-time structures

Models with extra dimensions solve the problem of the fine-tuning of the Higgs boson mass in the Standard Model by introducing extra space-time dimensions.

In the ADD, or "large extra dimensions" models [75] the gravitational and gauge interactions become united at the weak scale, hence the cut-off in Eq. (1.3) is of the order $\Lambda_{\mathrm{UV}} \sim 1$ TeV. The observed weakness of gravity is a consequence of the large size, $\mathcal{O}(\mathrm{mm})$, of the extra dimensions. On the other hand, the weak interaction is still strong compared to gravity because only gravity can propagate through the bulk while the SM fields are confined to the usual four dimensional space-time and not affected by the large extra dimensions.

The gravitons propagating through the bulk lead to an effective four dimensional theory with a virtually infinite tower of massive, but almost degenerate,

gravitons. Although each single graviton couples with the small gravitational strength the shear number of them can lead to striking signatures at colliders.

In "RS models" of extra dimensions [76], all the SM fields, as well as the gravitons can propagate in the bulk. In these models it is not the gravitational scale that is of the order of the weak scale as in the ADD models, but the other way around: the electroweak scale is of the order of the Planck scale. Due to an exponentially warped AdS_5 space-time the effective four dimensional weak scale is warped from the Planck scale down to ~ 1 TeV. In these models the masses of the SM particles can be inferred from the overlap of their wave functions in the fifth dimension with the Higgs boson wave function.

In many such models gauge interactions exist whose coupling with the third generation quarks and in particular to the top quark are enhanced. These include Kaluza-Klein (KK) excitations of the graviton [77–79] as well as the weak [80] and the strong gauge bosons [77, 81–88] which couple to top quarks. Such particles could show up as resonances in the $pp \to X \to t\bar{t}$ production channel and not in other channels, like di-jets or di-leptons, due to their small couplings to light particles.

In the next chapter the effects of general resonances on the top pair invariant mass is addressed in a model independent way.

1.3.4 Other models

Of course many other models that do not try to address the hierarchy problem specifically have been proposed. A simple, but not yet excluded idea is to introduce a fourth generation of $SU(2)_{\mathrm{L}}$ doublet fundamental particles. Recently, it received attention and could be of phenomenological relevance [89–92]. The existence of new heavy colored fermion states similar to the top (and bottom) quarks could mix with these SM particles. This looses the indirect constraints from unitarity on the CKM matrix and could have a direct impact on the size of the element V_{tb}, which plays an important role in single top production. This is addressed in more detail in Chapter 3. Furthermore, the t-channel single top channel provides the largest production mechanism in direct searches for the new massive quarks, as discussed in Chapter 4.

CHAPTER

TWO

TOP QUARK PAIR INVARIANT MASS

As stated in the introduction, the top quark plays a special role in many scenarios where alternative mechanisms for electroweak symmetry breaking are proposed. If on the one hand the fact that many rich and theoretically motivated models predict new physics in connection with the top quark provides a strong motivation for detailed experimental investigations, on the other it makes difficult to perform the analyses corresponding to all the suggested scenarios. A way to avoid such an "explosion" of models is a bottom-up approach, where first a physical observable, which carries some potential for BSM studies, is identified and then the effects due to the existence of new physics are systematically explored. The aim of this chapter is to present such a model independent approach to the discovery and identification of new physics in $m_{t\bar{t}}$, the top-antitop invariant mass distribution. We do not focus on specific models, instead we assume the existence of heavy particles, whose masses and quantum numbers are unknown but are such that interactions with the top quark are privileged, a feature common to many scenarios where the top quark plays a role in the EWSB, as discussed in the introduction. To simulate the physics associated with the new states, we have developed a dedicated "model" in the multipurpose Monte Carlo generator `MadGraph/MadEvent` [93–95].

This chapter is organized as follows. In Section 2.1, we perform an analysis of the theoretical uncertainties on the QCD predictions for $m_{t\bar{t}}$, in the low- as well as high-mass regions. We find that the shape of the $m_{t\bar{t}}$ distribution has very little theoretical uncertainties (in contrast to its normalization, *i.e.*, the

total cross section) and we argue it could provide a new handle on the top mass determination.

In Sections 2.3, 2.4 and 2.5 we propose a three-step analysis. In Section 2.3 the effects on $m_{t\bar{t}}$ induced by new heavy resonances in the s-channel, $pp \to X \to t\bar{t}$, from the presence of simple peaks, to non-trivial patterns arising from interference between signal and SM background. In the following section we assume that a resonance is found and study how the spin structure of a resonance affects the angular distributions of the top and anti-top quarks. In Section 2.5 we discuss how spin-correlations are affected by nature of the coupling of the resonances to SM particles, by simulating the full matrix elements including the decay, $pp \to X \to t\bar{t} \to 6f$. In Section 2.6 we discuss how non-resonant BSM effects can affect the $t\bar{t}$ invariant mass distribution and in Section 2.7 some of the reconstruction issues are discussed. We leave to Section 2.8 the discussion of the results and our conclusions.

2.1 Theoretical uncertainties in the top quark pair invariant mass

In this section we study the theoretical uncertainties on the available predictions for the invariant mass spectrum and their dependence on the top mass. We mainly focus on the LHC and refer to the results of Ref. [24] for the Tevatron. We start by considering the invariant mass spectrum of the $t\bar{t}$ pair calculated up to next-to-leading order (NLO), as implemented in `MCFM` [96]. We use the `CTEQ6M` PDF-set [97] and do not apply cuts on the final state particles. Here and in the following we always assume that the invariant mass can be fully reconstructed, see also Sec. 2.7. In Fig. 2.1 results at the LHC are plotted for three different top quark masses with uncertainty bands associated to the PDF errors and renormalization and factorization scale variations.

The PDF uncertainty is estimated by running the 41 members of the `CTEQ6` PDF set, with the scales set equal to $\mu_R = \mu_F = m_t$, and found to be about $\pm 3.2\%$. The scale uncertainty is obtained by varying the renormalization and factorization scales in the region between $\mu_R = \mu_F = m_t/2$ and $\mu_R = \mu_F = 2m_t$ independently. The associated total scale uncertainty at NLO is about $\pm 12\%$. Thus, the theoretical errors at the LHC are completely dominated by the scale uncertainty. This is contrast to the Tevatron where scale and PDF errors are comparable, of the order 5% [24].

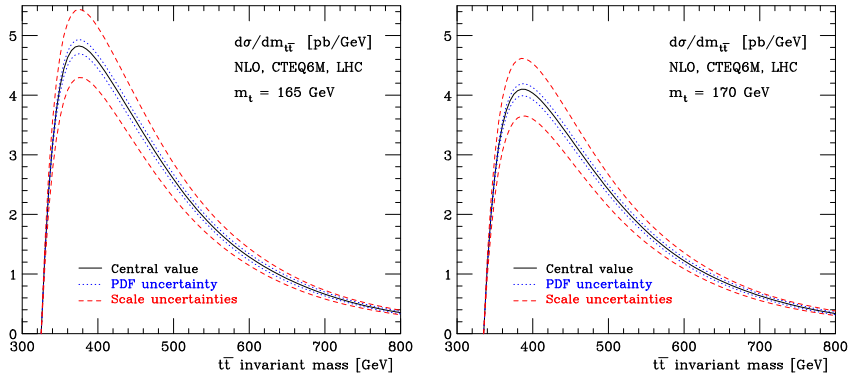

Figure 2.1: Scale (*dashed*) and PDF (*dotted*) uncertainties in the $t\bar{t}$ invariant mass spectrum for top masses (a) $m_t = 165$ GeV, (b) $m_t = 170$ GeV and (c) $m_t = 175$ GeV at NLO for the LHC using the `CTEQ6M` pdf set.

NLL resummed calculations suggest that the dependence on the scales could go down to $\pm 6\%$ [26, 98], however in that analysis the scales were not varied independently. A more recent study shows [25] that changing the scales independently leads to a more conservative estimation of the uncertainty to the order $\pm 9\%$.

Next we compare the NLO shapes for the invariant mass distribution with those obtained at LO and `MC@NLO` [99], Fig. 2.2, both at the Tevatron and the LHC. We find that the differences are minimal at the LHC, and well within the uncertainty bands of the theoretical errors on the NLO cross section. On the other hand, at the Tevatron the differences between LO and NLO, fixed and dynamic renormalization and factorization scales are larger.

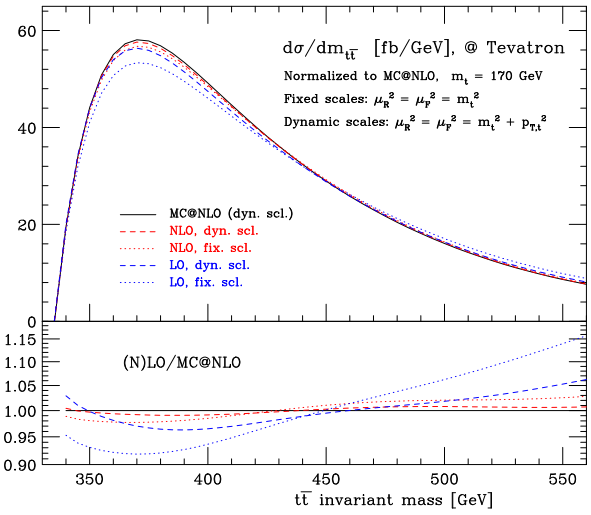

(a)

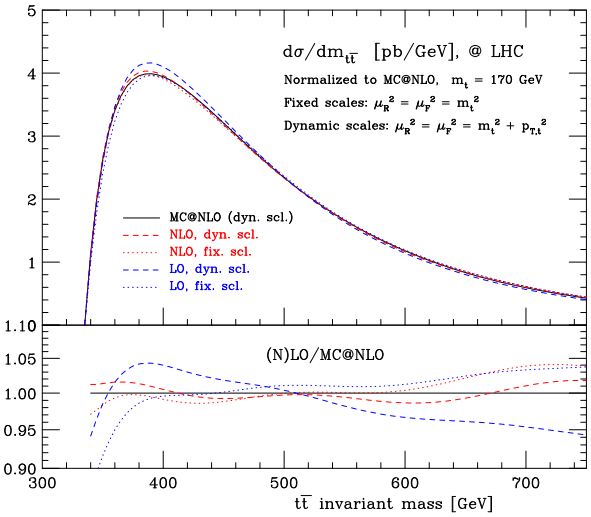

(b)

Figure 2.2: The MC@NLO $m_{t\bar{t}}$ distribution compared with the LO (*blue*) and NLO (*red*) fixed order predictions. The distributions are normalized to the MC@NLO cross section. We set $m_t = 170$ GeV, include no cuts, and use CTEQ6M for the NLO and MC@NLO, and CTEQ6L1 for the LO calculations.

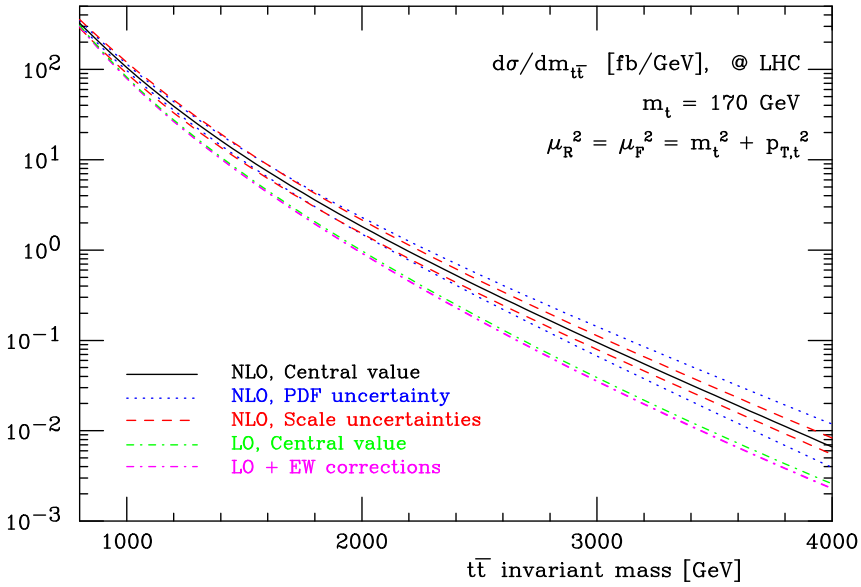

Figure 2.3: Scale (*dashed*) and PDF (*dotted*) uncertainties in the $t\bar{t}$ invariant mass spectrum for $m_t = 170$ GeV at NLO in QCD, with the `CTEQ6M` PDF-sets. Also plotted are the LO distribution (*light dash-dotted*), the LO including NLO Electro-Weak corrections (*dark dash-dotted*) with `CTEQ6L1` PDF-set. The LO distribution is normalized to the NLO total cross section.

In the high invariant mass region for the LHC, Fig. 2.3, the LO approximation starts to deviate from the NLO order and clearly underestimates the NLO distribution (note that curves here are normalized to the total cross section at NLO). Also, as expected, the PDF uncertainties start to increase and dominate the theoretical errors as the most important contributions come from the large x region. Next-to-leading order electroweak corrections to the LO distribution are also included in this figure [37, 38]. Their effect is to decrease the cross section by a few percent for invariant masses below 1000 GeV and up to 15% for invariant masses around 4 TeV (the Higgs boson mass dependence is mild). This means that EW effects on this distribution are negligible compared to the current PDF uncertainties and give only a minor deviation from the LO curve.

We conclude this section by mentioning the other sources of potentially large uncertainties in the determination of the $t\bar{t}$ invariant mass. The first is related to its reconstruction from the decay products. In general the uncertainty on the $m_{t\bar{t}}$ distribution will depend on the final state signature (fully-hadronic, single-lepton and double-lepton final states), which determine the reconstruction technique and, more importantly, on the detector efficiencies and resolu-

tions. For completeness we briefly discuss the current proposals for reconstruction in the various decay channels in Sec. 2.7. The second is due to both QCD backgrounds, *i.e.* multi-jet, W, Z+jets and WW+jets, and top backgrounds, *i.e.* single-top and $t\bar{t}$ itself as coming from a final state different signature than the one considered. While the QCD backgrounds at the Tevatron are severe but very well studied, it has been shown that at the LHC their impact at low $t\bar{t}$ invariant mass is negligible when at least one lepton is present in the final state [100]. In the high invariant mass tail, some QCD backgrounds, and in particular $W+$ one or two jets, become important due to the fact that the tops are highly boosted and can give rise to single jet-like topologies when they decay hadronically. The interested reader can find a detailed study for the single lepton final state signature in Refs. [101, 102].

2.2 Top quark mass dependence

As can be clearly seen from Fig. 2.1, the normalization, as well as the shape of the $t\bar{t}$ invariant mass distribution depends on the mass of the top quark. It is then natural to wonder whether such a rather strong dependence could provide another way to determine the mass of the top quark. The aim of this subsection is to provide a quantitative answer, based only on the theoretical uncertainties.

In Fig. 2.4 we have plotted the $t\bar{t}$ production cross section σ as a function of the top quark mass at the Tevatron (a) and the LHC (b). The scale uncertainties, even at the NLO, are rather large. Neglecting non-linear terms, a fit to the central curve gives

$$\Delta m_t/m_t \sim 0.2\Delta\sigma/\sigma + 0.03 \qquad \text{(LHC)}. \tag{2.1}$$

This equation relates the relative uncertainty on the measurement of the $t\bar{t}$ cross section to the relative uncertainty on the top quark mass: the $\Delta\sigma/\sigma$ term represents the slope and the constant term the horizontal spread, *i.e.*, the scale uncertainty, of the curves in Fig. 2.4. This means that a measurement of the cross section with an uncertainty of 5% would lead to a $0.2 \times 5\% + 0.03 = 4\%$ uncertainty of the top quark mass, the error being mainly associated with scale variations. At the Tevatron the situation is slightly different. The scale dependence is milder,

$$\Delta m_t/m_t \sim 0.2\Delta\sigma/\sigma + 0.015 \qquad \text{(Tevatron)}\,, \tag{2.2}$$

and known to be reduced at NLL [24], but the PDF errors, which are not included in the plot, are not negligible and are found to be of a similar size [24].

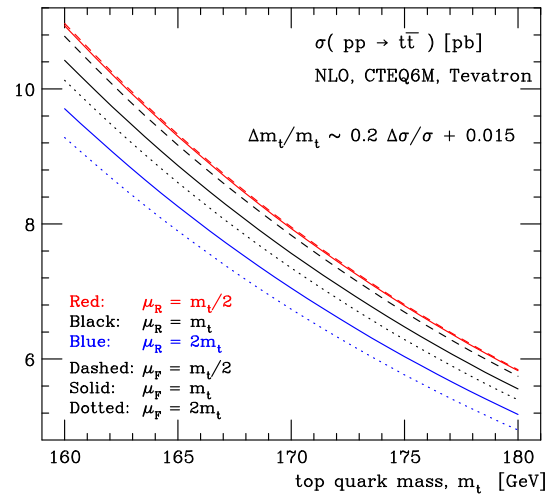

(a)

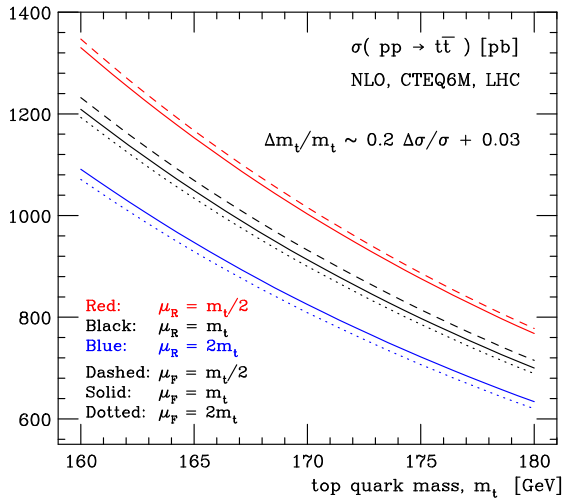

(b)

Figure 2.4: The $t\bar{t}$ production cross section as a function of the top quark mass m_t including scale dependence at the Tevatron (a) and the LHC (b).

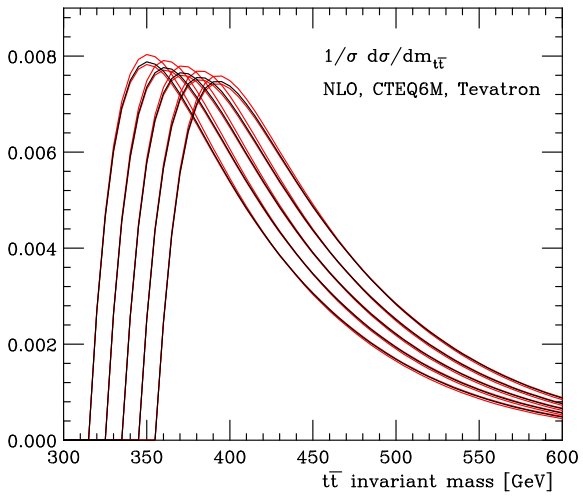

(a)

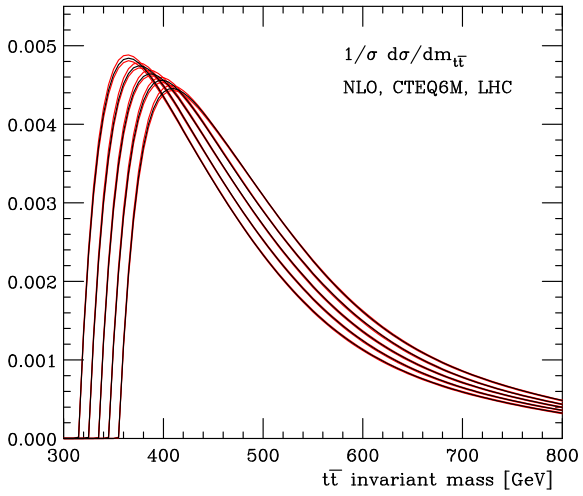

(b)

Figure 2.5: The normalized $t\bar{t}$ production cross section as a function of the $t\bar{t}$ invariant mass, $m_{t\bar{t}}$, for the Tevatron (a) and the LHC (b). Solid lines from left to right are for a top quark mass of $m_t = 160, \ldots, 180$ GeV in steps of 5 GeV, respectively. The bands spanned by the red lines show the scale uncertainties.

We can therefore conclude that the accuracy of an independent extraction of the top mass from a measurement of the cross section is limited by the NLO theoretical uncertainties. Recent work suggests that inclusion of NNLO corrections could reduce the scale uncertainties sizably [33].

It is therefore worth investigating whether information on the top mass can be extracted from some other quantity besides the total cross section. In Fig. 2.5 the $t\bar{t}$ invariant mass distributions normalized to unity, $\frac{d\sigma}{dm_{t\bar{t}}}\Big|_{\text{norm.}}$, are plotted for five different top quark masses, $m_t = 160 \ldots 180$ GeV in steps of 5 GeV. The bands spanned by the red lines show the left-over scale uncertainties which are sizably reduced compared to Fig. 2.1. We find that the shape of the $m_{t\bar{t}}$ distribution is quite insensitive to theoretical uncertainties, while retaining a strong dependence on the top quark mass. It is therefore interesting to consider whether the invariant mass distribution could provide an independent measurement of the top quark mass.

One way to quantify to which extent the shape is sensitive to the top mass vs. the theoretical uncertainties is to perform an analysis based on the first few moments of the normalized $t\bar{t}$ invariant mass distributions $\frac{d\sigma}{dm_{t\bar{t}}}\Big|_{\text{norm.}}$. This approach has the virtue of being simple and systematic. Needless to say, alternative quantities, such as the peak position, or more sophisticated techniques could also be employed. In fact, the idea of testing the *shape* of the $t\bar{t}$ invariant mass distribution against SM predictions has been picked up by the CDF top quark group [103].

In Fig. 2.6 we present the mean value $\langle m_{t\bar{t}} \rangle$, standard deviation s, skewness γ_1 and kurtosis γ_2 of the $t\bar{t}$ invariant mass distributions as a function of the top quark mass m_t for various scales at the LHC. We remind that the skewness (kurtosis) is a dimensionless quantity that gives a measure of asymmetry (peakedness) of a distribution. These quantities are defined as

$$\begin{aligned} \langle m_{t\bar{t}} \rangle = \int^{m_{\text{cutoff}}} \mathrm{d}m_{t\bar{t}}\, m_{t\bar{t}} \frac{d\sigma}{dm_{t\bar{t}}}\Big|_{\text{norm.}}, \qquad s = \sqrt{\mu_2}, \\ \gamma_1 = \frac{\mu_3}{\mu_2^{3/2}} \quad \text{and} \qquad \gamma_2 = \frac{\mu_4}{\mu_2^2} - 3, \end{aligned} \tag{2.3}$$

respectively. The central moments μ_n are defined as

$$\mu_n = \int \mathrm{d}m_{t\bar{t}} \left(m_{t\bar{t}} - \langle m_{t\bar{t}} \rangle\right)^n \frac{d\sigma}{dm_{t\bar{t}}}\Big|_{\text{norm.}}. \tag{2.4}$$

In our analysis we focus on the low invariant mass region and therefore we have limited the $m_{t\bar{t}}$ integrals to $m_{t\bar{t}} < m_{\text{cutoff}} = 1$ TeV. The aim of this cut is just to mimic an experimental analysis where the precision on the higher moments

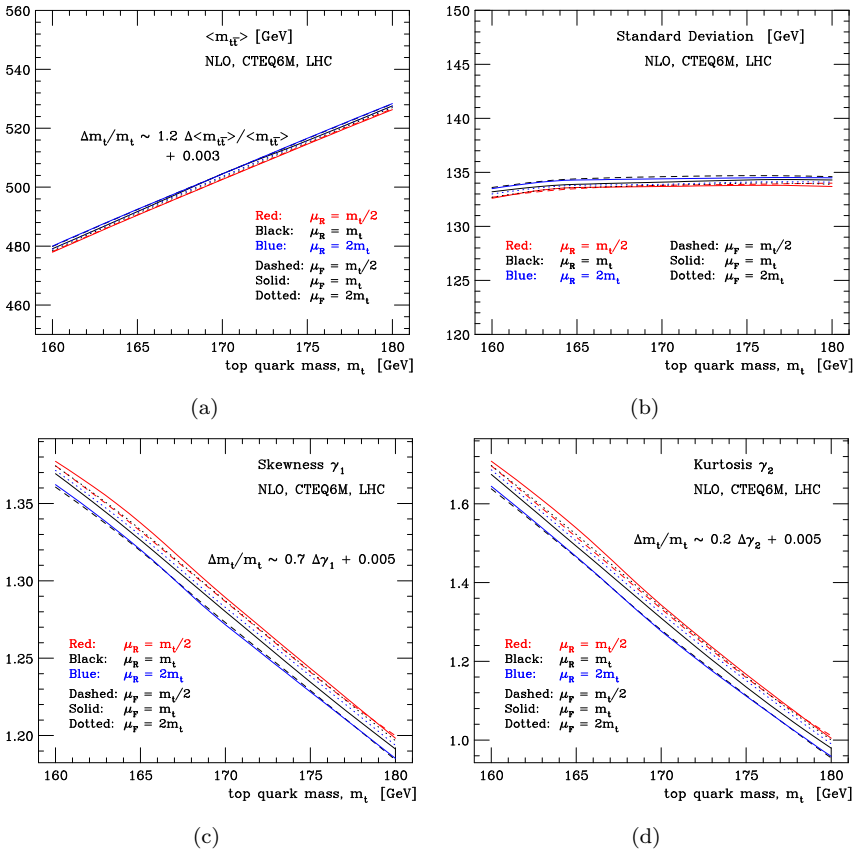

Figure 2.6: The average value (a), standard deviation (b), skewness (c) and kurtosis (d) of the $t\bar{t}$ invariant mass distribution as a function of the top quark mass m_t including the scale dependence at the LHC.

would be limited by the statistics. Since our purpose is only for illustration we do not consider these effects further. However, we stress that our numerical results do retain a significant dependence on this cutoff.

Due to the small scale uncertainty and the strong linear correlation, the mean of the $t\bar{t}$ invariant mass distribution, $\langle m_{t\bar{t}} \rangle$, Fig. 2.6(a), appears to be an excellent estimator of the top quark mass. From the experimental point of view, one can also hope for smaller uncertainties than those associated to the measurement of total cross section. In fact, to measure the mean, many systematics, such as those coming from luminosity or tagging efficiencies, are much less important. A fit to the mean value shows that $\Delta m_t/m_t \sim 1.2\Delta\langle m_{t\bar{t}}\rangle/\langle m_{t\bar{t}}\rangle + 0.003$. So, for instance, if the mean value is measured with a 1% uncertainty, the uncertainty of the top quark mass is only 1.5%, including the scale uncertainties.

The standard deviation, Fig. 2.6(b), is almost constant and therefore is not suitable for a top quark mass measurement. In Figs. 2.6(c) and 2.6(d) the skewness and the kurtosis for the $t\bar{t}$ invariant mass are plotted, respectively. Also here, the scale uncertainty is reduced, while still slightly larger than for the mean value, Fig. 2.6(a). The slopes of the lines are promising, in particular for the kurtosis, which means that a relatively large experimental error on the measurement of the kurtosis leads to a small error on the top mass measurement.

At this point, we have to stress that the above simple analysis does not include neither statistical nor systematics effects in the data, which should also be carefully considered. In particular, the higher moments such as the skewness and the kurtosis are more sensitive to the tail of the $m_{t\bar{t}}$ distribution then the lower moments and therefore more sensitive to statistical and systematic effects that affect more strongly this tail. Eventually, the final uncertainty on the top quark mass will depend on how well the above quantities can be measured. It is plausible to expect that a combined analysis based on the above quantities might lead to an even smaller uncertainty for the top quark mass.

For completeness we show the same analysis performed at the Tevatron energies, see Fig. 2.7. Also in this case, we have used a fixed order NLO calculation to estimate the scale uncertainties. However, as we have already mentioned, at the Tevatron the $t\bar{t}$ pairs are produced almost at threshold, hence a resummed calculation which predicts a smaller scale uncertainty, is preferred [24].

The Tevatron results (Fig. 2.7) are similar to those obtained in the LHC study, but the reduction in the scale uncertainties by analyzing the (higher) moments is smaller compared to the LHC. The first moment, *i.e.*, the mean value, is probably the best estimator for the top quark mass among all the moments,

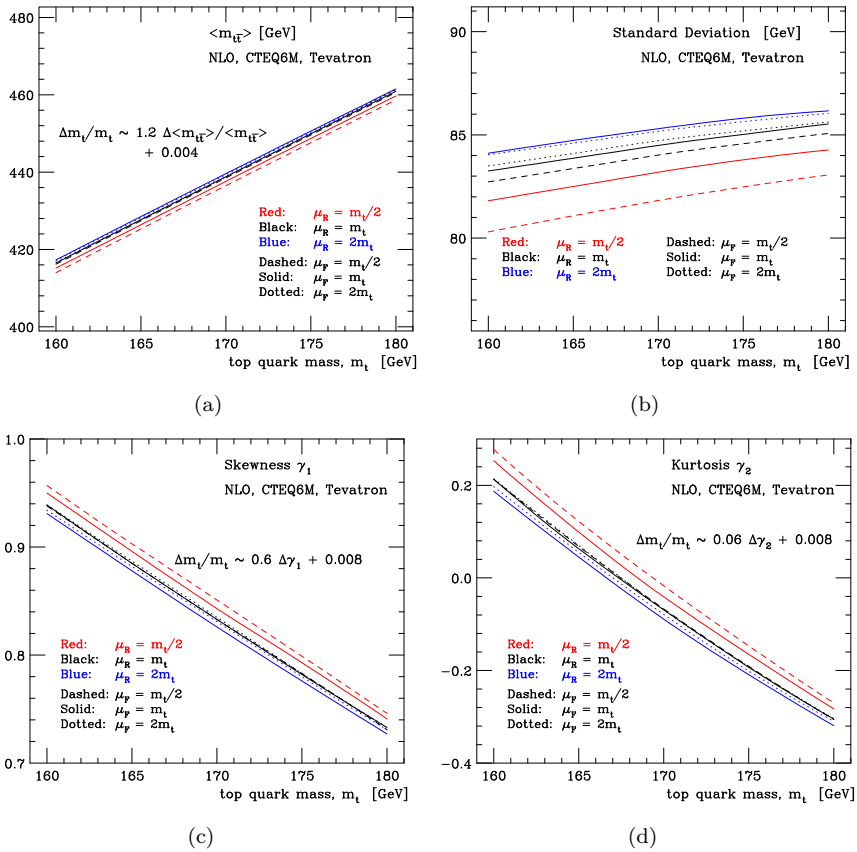

Figure 2.7: The average value (a), standard deviation (b), skewness (c) and kurtosis (d) of the $t\bar{t}$ invariant mass distribution as a function of the top quark mass m_t including the scale dependence at the Tevatron. For the skewness and kurtosis we restricted the integration region in Eq. 2.4 to $m_{t\bar{t}} < 600$ GeV.

due to its small constant value of 0.004, and the reasonably good proportionality factor of 1.2. The higher moments are more sensitive to statistical fluctuations and might be less suitable with a limited sample. The lack of events in the higher invariant mass regions might give rise to larger errors for the skewness and worse the kurtosis. In these plots we restrict the $t\bar{t}$ invariant mass to below $m_{\text{cutoff}} = 600$ GeV. We mention that even though using the fixed order NLO calculation we have overestimated the scale uncertainties, we have neglected the PDF errors which at the Tevatron can reach the 6-7% [24] and errors coming from the reconstruction of the $t\bar{t}$ invariant mass from the (anti-)top quark decay products, see Sec. 2.7.

Finally, we comment about the definition of the top quark mass. In the more standard top mass measurements where the top mass is reconstructed from its decay products, the top quark invariant mass is sensitive to extra radiation and to non-perturbative effects due to confinement, typical of a pole mass [104]. In this respect the same issues and problems in associating a theoretically well-defined mass to the measurement remain in the case of extracting the top quark mass from the $t\bar{t}$ invariant mass. This is at variance with an extraction of the top mass from a cross section measurement which can be directly related to a short distance mass and does not suffer from the same non-perturbative or extra radiation effects. We stress, however, that $m_{t\bar{t}}$ is at least twice the top quark mass, which would decrease the relative impact of the ambiguities due to extra radiation. In addition, typical combinatorial systematics associated to the assignment of the jets to the "right" tops, are absent for $m_{t\bar{t}}$. In this respect, more experimental work on the systematics affecting such a measurement would be certainly welcome.

2.2.1 Threshold effects

Of course the $t\bar{t}$ threshold is extremely sensitive to the top quark mass. However, both experimentally as well as theoretically the region very close to threshold is more difficult to control. Therefore, a measurement of only the threshold is not a good discriminant for the top quark mass, but a good resolution in the invariant close through threshold could show some interesting effects: recently [105, 106] several studies to threshold effects in $t\bar{t}$ production at the LHC were performed. In the framework of non-relativistic QCD (NRQCD), including effects from soft gluons, the $t\bar{t}$ invariant mass distribution shows contributions from a would-be bound state governed by a non-relativistic Green's function as a small peak just below threshold, see, *e.g.*, Fig. 4 of Ref. [106].

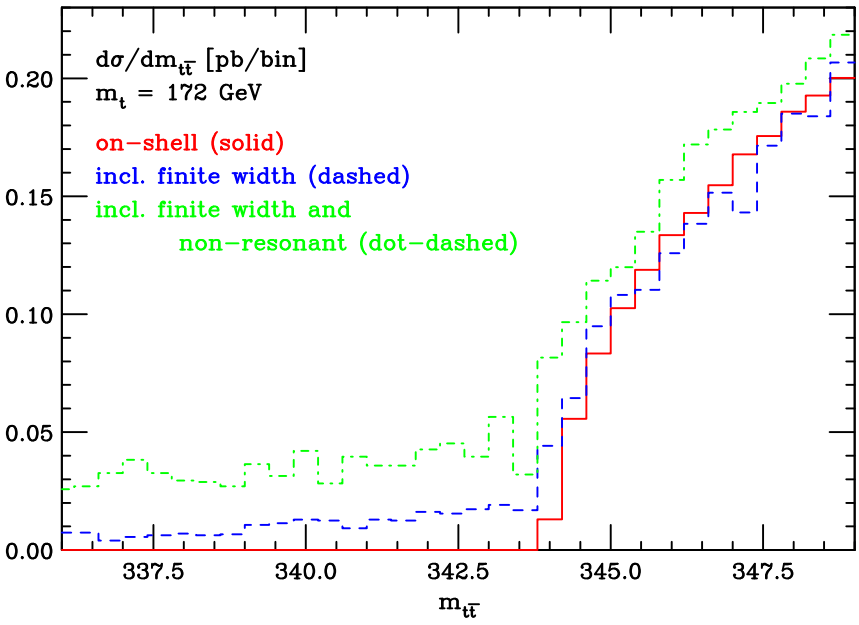

Figure 2.8: Leading order prediction for the $t\bar{t}$ invariant mass distribution close to the $t\bar{t}$ threshold for the LHC. The red curve is for on-shell top quarks, the blue curve includes off-shell effects and the green curve includes all resonant contributions.

However, in this context effects from non-resonant contributions are usually not taken into account. The question arises if this is justified. To correctly take these effects into account the decay of the top quarks $t \to Wb$ needs to be taken into account in the simulation. At the moment there are no NLO computations that include the decay of the top quarks and have the full NLO prediction for the $WbWb$ final state. The best available approximation is the leading order.

To study the effects from non-resonant contributions we start by considering the effects from the possible off-shellness of the top quarks. We simulate $t\bar{t}$ production with `MadGraph` including the subsequent decay of the top quarks to Wb. In Fig. 2.8 the $t\bar{t}$ invariant mass distribution is plotted in the region close to the threshold. The red curve is the LO prediction for on-shell top quark pairs, while the blue curve includes the possible off-shellness.

From this plot it is clear that the effects from off-shell top quarks are small. Above threshold there is no difference, as expected. Below threshold the cross section is no longer exactly zero, but the tail is very small and will be impossible to see at the LHC, even if backgrounds would be neglected, due to detector (in)efficiencies.

Besides the off-shell effects, potentially larger contributions might come from non-(double-)resonant non-reducible backgrounds, such as electroweak tW production with an additional b-quark. These effects are slightly larger, see the green curve in Fig. 2.8, but also here these contributions can safely be neglected when studying the $t\bar{t}$ invariant mass. The threshold effects calculated in Ref. [106] are dominant in this region of phase space.

However, also these contributions are small and, in particular when the detector effects are taken into account, it will be extremely challenging to unambiguously disentangle these events from other backgrounds (such as W+jets) or the $t\bar{t}$ signal.

2.3 Effects from BSM resonances

In this section we investigate the effects of (model-independent) new resonances on the $t\bar{t}$ invariant mass spectrum. All the numerical results presented here have been obtained with `MadGraph/MadEvent`, through the implementation of a dedicated "model", `topBSM`, which is publicly accessible on the `MadGraph` servers for on-line event generation and for download.*

`topBSM` offers the possibility of studying a wide range of new physics resonances and efficiently exploits the flexibility and the possibilities of `MadGraph`:

- SM effects are consistently included, *i.e.*, possible non-trivial interference effects between new resonances and the $t\bar{t}$ background are taken into account. As it will be shown in the following, in some cases such effects can be important and might lead to very distinctive signatures (cf. the case of the peak-dip structure arising in $m_{t\bar{t}}$ due to the presence of a (pseudo) scalar state). In general, they should always be included.
- The full matrix elements $2 \to 6$ including the decays of the top quarks can be generated, which is crucial for spin correlation studies.

*Technical documentation on how to use the model can be found at `http://cp3wks05.fynu.ucl.ac.be/twiki/bin/view/Software/TopBSM`.

- The generated events can be automatically interfaced to parton showers programs, such as `Pythia` [107] or `Herwig` [108], to shower and hadronize the events after which these events can be processed by a detector simulation for full experimental analyses.

We have considered s-channel spin-0, spin-1 and spin-2 resonances, of different color and CP parity, as listed in Table 2.1. The parameters related to each resonance are simply the mass, the width and the relevant values of the couplings to Standard Model particles which enter in the production process (to the partons and to the top quark).

2.3.1 Spin-0 resonances

The first resonances we discuss are spin-0 particles. We distinguish between color singlet (ϕ) and color octet (S^0), as well as parity even (scalar) and odd (pseudo-scalar) spin-0 particles.

Color singlet

Let us start by considering a color singlet (pseudo) scalar boson ϕ contributing to the $t\bar{t}$ process $gg \to (\phi \to) t\bar{t}$. The Feynman diagram for this loop induced

Spin	color	parity $(1, \gamma_5)$	some examples/Ref.
0	0	(1,0)	SM/MSSM/2HDM, Ref. [109–111]
0	0	(0,1)	MSSM/2HDM, Ref. [110, 111]
0	8	(1,0)	Ref. [112, 113]
0	8	(0,1)	Ref. [112, 113]
1	0	(SM,SM)	Z'
1	0	(1,0)	vector
1	0	(0,1)	axial vector
1	0	(1,1)	vector-left
1	0	(1,-1)	vector-right
1	8	(1,0)	coloron/KK gluon, Ref. [114–116]
1	8	(0,1)	axigluon, Ref. [115]
2	0	–	graviton "continuum", Ref. [75]
2	0	–	graviton resonances, Ref. [76]

Table 2.1: The BSM particles included in the `topBSM` "model".

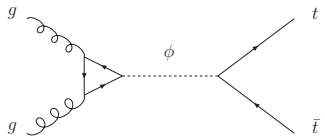

Figure 2.9: Feynman diagram for the (pseudo) scalar contribution to $t\bar{t}$ production.

process is depicted in Fig. 2.9. The spin-0 coupling strength to quarks,

$$g_{\phi qq} = a_1 i\frac{m_q}{v} + a_2\frac{m_q}{v}\gamma_5, \tag{2.5}$$

is proportional to the quark mass m_q. In analogy with the SM, v is the spin-0 field vacuum expectation value and a_1 and a_2 are real proportionality factors for the parity even and odd spin-0 particles, respectively. For the SM Higgs boson $a_1 = 1$ and $a_2 = 0$, while for a pure pseudo-scalar $a_1 = 0$ and a_2 is non-zero.

We do not include scalar production by (anti-)quark annihilation, $q\bar{q} \to \phi$, because for this cross section to be sizable compared to the loop induced gluon fusion process, the branching ratio for the scalar to $t\bar{t}$ has to be small and can be neglected.

Since we are interested in scalars with strong couplings to the top quark, we neglect all particles in the loop of Fig. 2.9 except for the most heavy quark, *i.e.*, the top quark. If the mass of the spin-0 boson is larger than twice the mass of the top quark, the loop-induced gluon-gluon-(pseudo) scalar coupling develops an imaginary part, which leads to a peak-dip structure for the interference terms between the QCD background and the signal [109–111].

The possibility to detect a signal in the $t\bar{t}$ invariant mass depends on the width of the spin-0 resonance. In general, a scalar particle couples also to the electroweak bosons. In the SM the decay rate to W, Z is much larger than the decay rate to $t\bar{t}$, and therefore the $t\bar{t}$ channel is suppressed. Moreover, the presence of a destructive interference between the signal and the QCD background and the relatively large width of the scalar makes detection very difficult. An enhanced coupling to top would not help much because the improvement in the branching ratio would be compensated by an increase of the total width. In conclusion, there is little hope to see a SM-like scalar by looking at the $t\bar{t}$ invariant mass spectrum, even if the coupling to top quark were (much) larger than in the SM.

On the other hand, the case of a pseudo-scalar or a 'boson-phobic' scalar resonance that does not couple to the heavy vector bosons is more promising. For such a state, the branching ratio to $t\bar{t}$ can be taken unity, $\mathrm{BR}(\phi \to t\bar{t}) = 1$, *i.e.*, the total width of the scalar spin-0 resonance is equal to the SM partial width to $t\bar{t}$. SUSY models with this feature can be constructed [117]. The smaller widths of the pseudo-scalar and the boson-phobic scalar give a narrow resonance peak in the $t\bar{t}$ invariant mass spectrum. The interference between the signal and the QCD $t\bar{t}$ production leads to a dip in $t\bar{t}$ production at an invariant mass just above the mass of the spin-0 particle. In this case the signal together with the interference terms sum to the characteristic peak-dip structure, Figs. 2.10 and 2.11.

The *dot-dashed* line in Figs. 2.10 and 2.11 shows the effect of a 400 GeV color singlet spin-0 particle on the $t\bar{t}$ invariant mass spectrum with couplings $a_1 = 1$, $a_2 = 0$ and $a_1 = 0$, $a_2 = 1$, respectively. Comparing with the QCD $t\bar{t}$ production, the *dark solid* line, a peak-dip structure is visible when the spin-0 particle is a pseudo-scalar, $a_1 = 0$ and $a_2 = 1$. In the case where it is a scalar, $a_1 = 1$ and $a_2 = 0$, there is only a peak and a very small dip.

If the coupling to the top quark is enhanced, the peak as well as the dip becomes broader due to the larger decay width. The peak increases in the case the spin-0 is a scalar, but remains the same for the pseudo-scalar. The *dashed* line shows the effect of enhancing the ttH coupling by a factor of two. If the coupling to the top quarks is taken even larger, the increasing width of the (pseudo) scalar starts to dominate the effects on the invariant mass. This results in the disappearance of the dip, as shown by the *light solid* line in Figs. 2.10 and 2.11.

In the case where the coupling to the top is smaller than in the SM, the peak of the scalar gets smaller and the dip completely disappears. The effect of varying the coupling for the pseudo-scalar are much smaller. Even if the coupling to top quarks is reduced by a factor of two, $a_1 = 0$ and $a_2 = 0.5$, a very clear peak-dip structure is still visible, as shown by the *dotted* line in Figs. 2.10 and 2.11.

Color octet

The case of a color octet resonance is very similar. Here we shall study scalar S_R^0 and a pseudo-scalar S_I^0 color octets, similar to those introduced in Refs. [112, 113]. In these models the (pseudo) scalar color octet couples only to quarks, with the same SM coupling but for the color

$$g_{S_R^0 qq} = \eta_U i \frac{m_q}{v} T^a_{ij}, \qquad \text{and} \qquad g_{S_I^0 qq} = \eta_U \gamma_5 \frac{m_q}{v} T^a_{ij}, \tag{2.6}$$

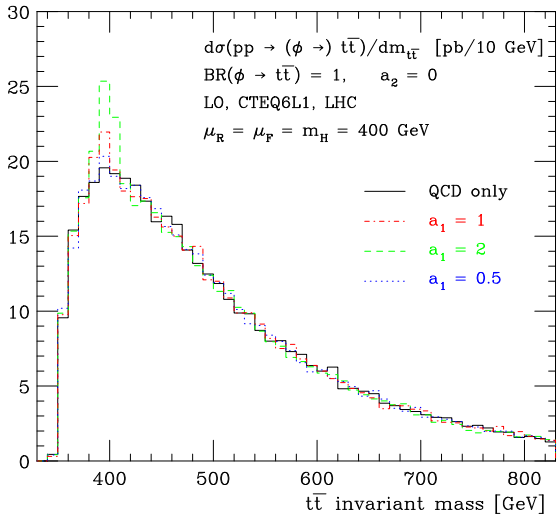

(a)

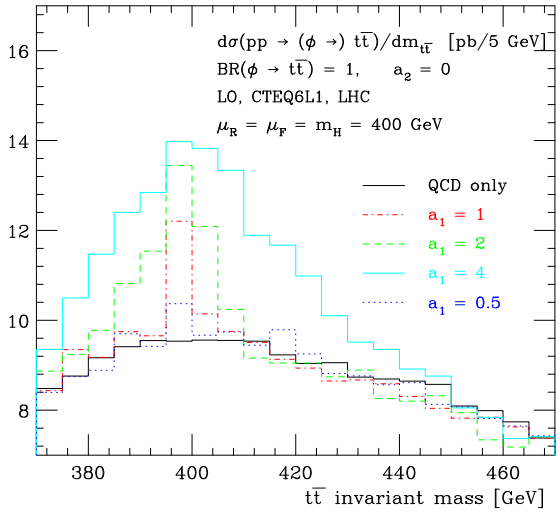

(b)

Figure 2.10: Invariant $t\bar{t}$ mass spectrum for the boson-phobic scalar. *Bottom*: The interesting region with finer binning. Different colors represent different coupling strength of the Higgs to top quarks: *dot-dashed* for the Standard Model coupling and *dotted*, *dashed* and *light solid* for 0.5, 2 and 4 times the Standard Model coupling strength, respectively. *Dark solid* is QCD $t\bar{t}$ production, *i.e.*, without the Higgs signal. All plots were produced using the `CTEQ6L1` PDF set with $\mu_R = \mu_F = 400$ GeV. No acceptance cuts are applied.

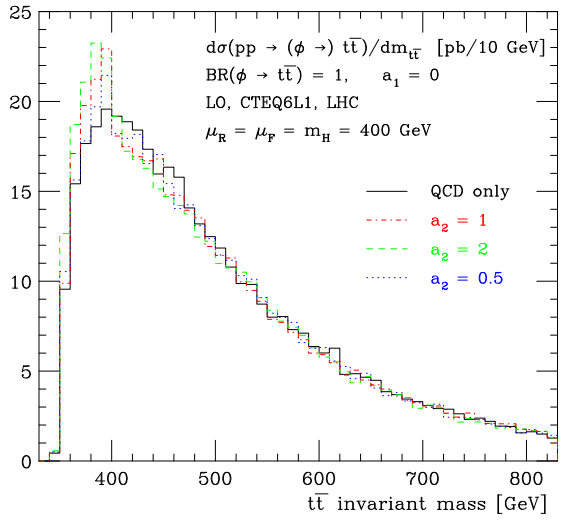

(a)

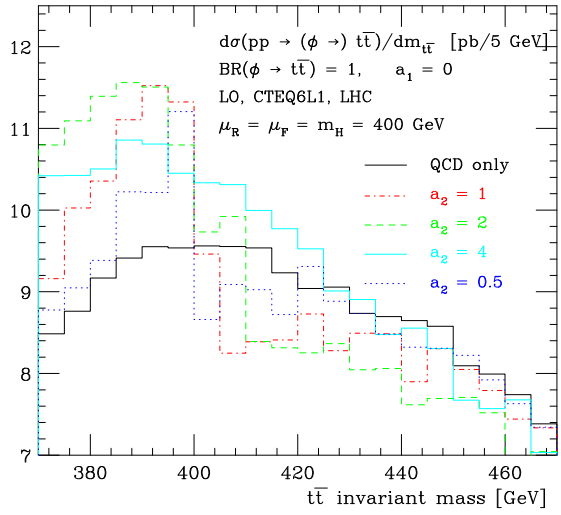

(b)

Figure 2.11: Invariant $t\bar{t}$ mass spectrum for the boson-phobic pseudo-scalar. *Bottom*: The interesting region with finer binning. Different colors represent different coupling strength of the Higgs to top quarks: *dot-dashed* for the Standard Model coupling and *dotted*, *dashed* and *light solid* for 0.5, 2 and 4 times the Standard Model coupling strength, respectively. *Dark solid* is QCD $t\bar{t}$ production, *i.e.*, without the Higgs signal. All plots were produced using the `CTEQ6L1` PDF set with $\mu_R = \mu_F = 400$ GeV. No acceptance cuts are applied.

where η_U is a coupling proportionality factor and of order 1. The production and decay mechanism for the (pseudo) scalar color octet are similar to the 'peak-dip' color singlets, *i.e.*, the resonance is produced through a top quark loop by gluon-gluon fusion, and the decay is mainly to top quarks. We find that compared to the 'peak-dip' color singlet the 'signal' cross section is 5/72 times smaller, *i.e.*, $\sigma(gg \to S^0_{R,I} \to t\bar{t}) = \frac{5}{72}\sigma(gg \to H \to t\bar{t})$, the interference between signal and background is 5/12 times smaller and the width of the (pseudo) scalar color octet is 6 times smaller than the width of the 'peak-dip' (pseudo) scalar color singlet. In Fig. 2.12(a) the $t\bar{t}$ invariant mass is plotted in a model with a color octet scalar of a mass of 400 GeV, and in Fig. 2.12(b) for the pseudo-scalar. As expected, the results are very similar to the color singlet, see the lower plots of Figs. 2.10 and 2.11. The same 'peak-dip' structure is also present for the color octet but it is more pronounced. This is mainly due to the smaller width of the (pseudo) scalar color octet.

We conclude this section by mentioning that pseudo-scalar singlet and octet resonances could also arise from bound states of meta-stable gluinos in split SUSY scenarios [118]. Also in this case $gg \to \phi$ would be the dominant production channel and it could be described within the same framework.

2.3.2 Spin-1 resonances

In this section we discuss a spin-1 resonance produced by $q\bar{q}$ annihilation[†]. This resonance can either be a color singlet or a color octet. For the color octet case we distinguish between a vector and an axial-vector. Although both the vector and the axial-vector interfere with the QCD $t\bar{t}$ production, only the vector shows interference effects in the $t\bar{t}$ invariant mass spectrum.

Including an s-channel color singlet vector boson (a "model-independent" Z') in the $t\bar{t}$ production process gives a simple peak in the invariant mass spectrum as can be seen from the *dot-dashed* line in Fig. 2.13. The precise width and height of the peak depends on the model parameters in the model for the Z'. As a benchmark we show a Z' vector boson with mass $m_{Z'} = 2$ TeV that couples with the same strength to fermions as a Standard Model Z boson. The interference effects with the SM Z boson can be neglected in the $t\bar{t}$ channel, so the peak is independent of the parity of the coupling.

In general, for the color octet spin-1 particles the interference with the SM $t\bar{t}$ production cannot be neglected. Two cases are to be considered: a color octet

[†]According to Yang's theorem [119] the production of an on-shell color singlet resonance by two vector particles is forbidden at leading order.

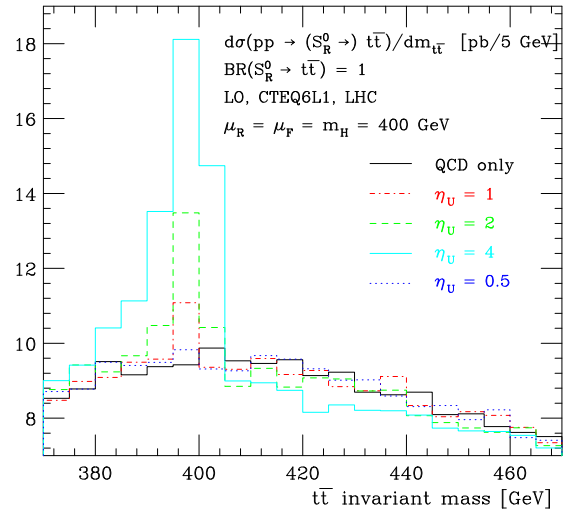

(a)

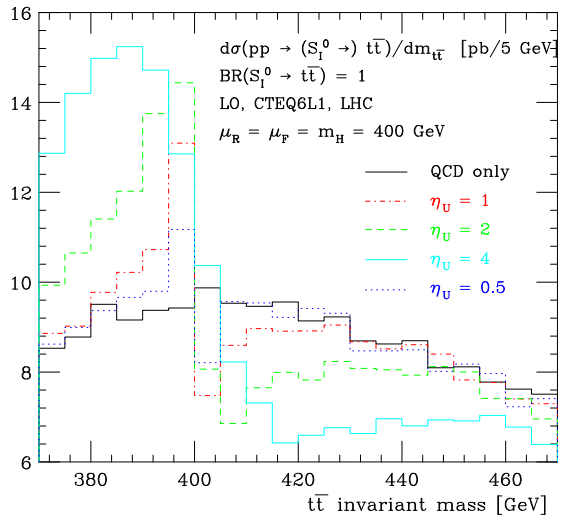

(b)

Figure 2.12: Invariant $t\bar{t}$ spectrum for $pp \to t\bar{t}$ including a s-channel S_R^0 scalar color octet (a) and a pseudo-scalar scalar S_I^0 color octet (b) with masses $m_{S_R^0} = m_{S_I^0} = 400$ GeV. *Dark solid* line is QCD $t\bar{t}$ production, *dash-dotted* line is with standard coupling between the scalar and $t\bar{t}$, *dashed*, *light solid* and *dotted* the coupling is 2, 4 and 0.5 times as large, respectively. All plots were produced using the `CTEQ6L1` PDF set with $\mu_R = \mu_F = 400$ GeV. No acceptance cuts are applied.

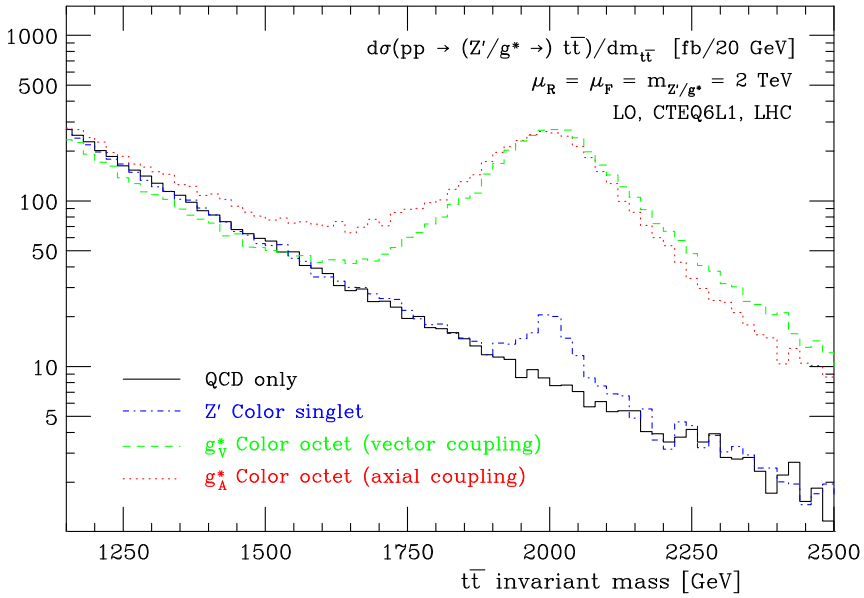

Figure 2.13: Invariant $t\bar{t}$ spectrum for $pp \to t\bar{t}$ including a s-channel Z' color singlet vector boson and color octet (axial) vector bosons with masses $m_X = 2000$ GeV that couples with standard model strength to quarks. *Solid* QCD $t\bar{t}$ production, *dot-dashed* with a color singlet (Z'), *dotted* with a color octet axial vector (axigluon g_A^*), *dashed* with a color octet vector boson (KK gluon/coloron g_V^*). All plots were produced using the `CTEQ6L1` PDF set with $\mu_R = \mu_F = 2000$ GeV. No cuts were applied in making any of the plots.

vector particle (*e.g.*, a KK gluon [116] or coloron [115]), and an axial-vector particle (*e.g.*, an axigluon [115, 120, 121]). It is natural to assume a coupling strength equal to the strong (QCD) coupling g_s for their coupling to quarks.

In Fig. 2.13 the effects of a color octet spin-1 particle on the $t\bar{t}$ invariant mass spectrum are presented. The interference effects of the axial vector (*dotted* line) with the QCD $t\bar{t}$ production do not change the shape of the $t\bar{t}$ invariant mass spectrum. Hence the effects of the color octet axial vector and the color singlet are very similar, apart from the size due to the different coupling constant.

The interference of the color octet vector particle with the QCD $t\bar{t}$ production does effect the $t\bar{t}$ invariant mass distribution. There is negative interference in the invariant mass region below the resonance mass and positive interference for heavier invariant masses. This slightly changes the shape of the peak as can be seen from Fig. 2.13. Other quantities, such as the charge asymmetry between

the top and the anti-top quarks could be more sensitive to axial vectors [122] and could help their discovery at higher invariant masses.

2.3.3 Spin-2 resonances

The interactions between spin-2 particles, or *gravitons*, and ordinary matter is in general Planck suppressed, which makes it impossible to see effects of the gravitons at TeV energies. There are, however, models with extra dimensions where the contributions from the gravitons might be large enough to make a discovery at the LHC. In this case a model-independent approach is not really appropriate. Instead we consider two scenarios that have distinct signals in the $t\bar{t}$ invariant mass. First the ADD model [75, 123], where the effect of a the large number of graviton KK states contributing to a cross section could be important and, secondly, the RS model [76, 124] where only a limited number of KK modes contribute, but the coupling constant itself is enhanced by a large "warp" factor.

In the so-called ADD models [75, 123] all the SM fields are confined to a four-dimensional brane, letting only gravitons propagate through the bulk. The extra n bulk dimensions are compactified on a n-torus with a radius R. If the radius R is large enough, (of the order of 0.1 mm for 2 extra dimensions) the $(4+n)$ dimensional Planck scale can be as small as the TeV scale.

Due to the fact that the radius of the extra dimensions is large, the graviton KK states can be almost degenerate in mass. So, although all graviton couplings are Planck suppressed, the sum of all the KK states can contribute significantly to the $t\bar{t}$ invariant mass spectrum. All states are summed up to the cutoff scale M_S, defined by $\lambda^2 R^n = 8\pi(4\pi)^{n/2}\Gamma(n/2)M_S^{-n+2}$, where λ is related to the four dimensional Newton's constant $\lambda = \sqrt{16\pi G_N}$.

The effect of this tower of graviton states on the $t\bar{t}$ invariant mass distribution is plotted in Fig. 2.14 in the case of 3 extra dimensions and for 4 different cutoff scales. Due to the sum over all nearly degenerate resonances, there is no single resonance peak in the invariant mass distribution. It is also clear that the distribution is only valid well below the cutoff scale M_S, otherwise unitarity violating effects become sizable.

In the so-called RS model [76,124] there is one extra dimension postulated that is compactified to a $\mathbf{S}^1/\mathbf{Z}_2$ orbifold. There are two branes on specific points of the orbifold: a "Planck" brane at $\phi = 0$ and a "TeV" brane at $\phi = \pi$ where the physical SM fields are confined. The bulk space is warped in such a way that the (reduced) Planck mass is warped down on the "TeV" brane to

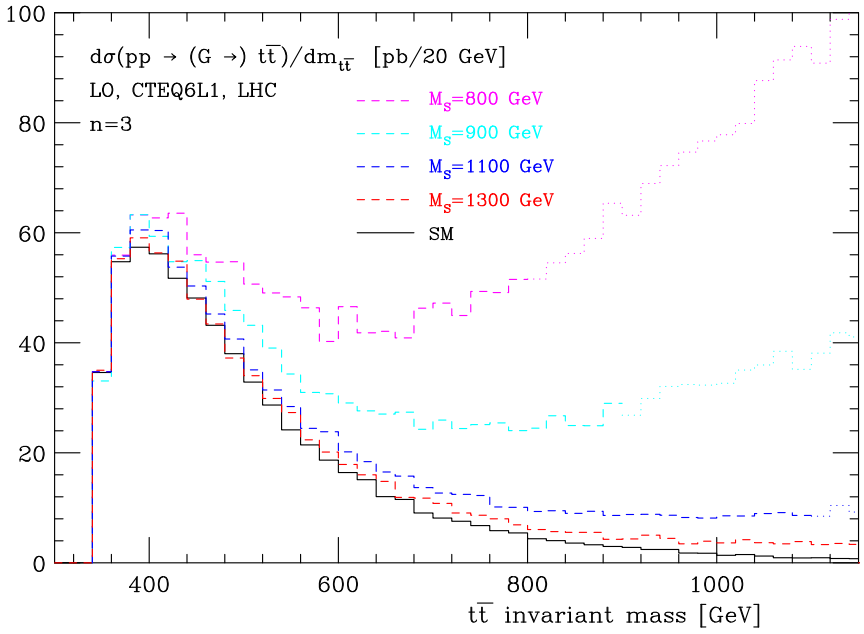

Figure 2.14: Invariant $t\bar{t}$ spectrum for $pp \to t\bar{t}$ including s-channel gravitons. The distributions show the effect of the almost degenerate tower of KK gravitons in the ADD model with $n = 3$ extra dimensions and, from top to bottom, with a cutoff scale $M_S = 800$, 900, 1100 and 1300 GeV. The bottom line shows contributions from SM only. We used `CTEQ6L1` and set the scales to $\mu_R = \mu_F = m_t$.

$\Lambda = \overline{M}_{\rm pl} e^{-\pi\kappa R}$. The gauge hierarchy problem ($\Lambda = \mathcal{O}(1\ \text{TeV})$) is now solved with only a minor fine-tuning of $\kappa R \simeq 12$. After KK compactification of the massless graviton field, the coupling constant of KK gravitons with matter is given by the inverse of Λ.

A prediction in the RS model is that the masses of the KK modes m_n are given by $m_n^2 = x_n \kappa e^{-\pi\kappa R}$, where x_n are the positive zero's of the Bessel function $J_1(x)$. If one of the masses is given, all the others are fixed, which could give rise to a series of resonances in the $t\bar{t}$ invariant mass spectrum.

In Fig. 2.15 the effect of a series of KK graviton modes on the $t\bar{t}$ invariant mass spectrum is shown with $m_1 = 600$ GeV and for various ratios $\kappa/\overline{M}_{\rm pl}$. The resonances are clearly visible over the QCD background. Higher KK states are characterized by larger widths.

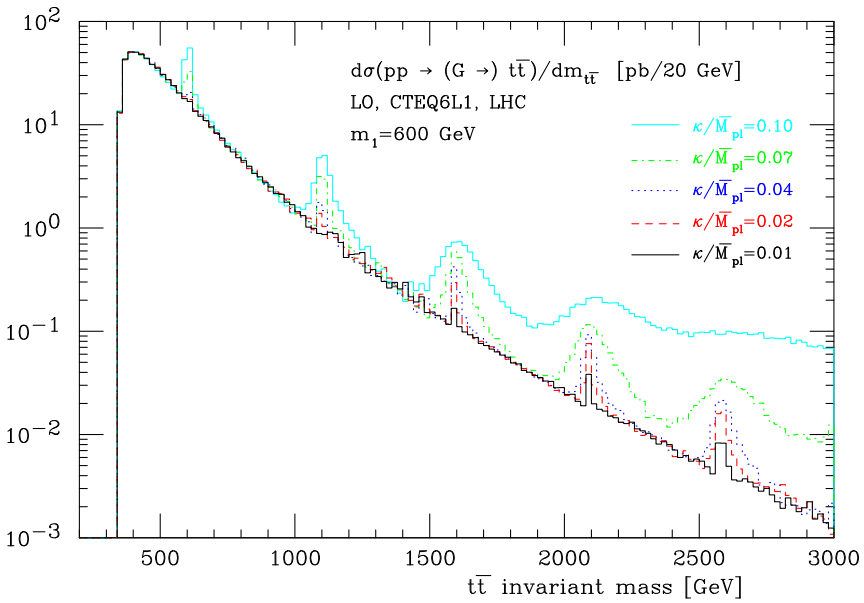

Figure 2.15: Invariant $t\bar{t}$ spectrum for $pp \to t\bar{t}$ including s-channel gravitons. The distribution shows the effect of a couple of KK resonances in the RS extra dimensions model. The mass of the first KK mode is $m_1 = 600$ GeV and the colored lines represent various choices for the ratio $\kappa/\overline{M}_{\rm pl}$. We used `CTEQ6L1` and set the scales to $\mu_R = \mu_F = m_t$.

2.4 Spin information from (anti-)top quark directions

A useful, yet simple, quantity sensitive to the spin of the intermediate heavy state into a $t\bar{t}$ pair, is the Collins-Soper angle θ [125]. This angle is similar to the angle between the top quark and the beam direction, but minimizes the dependence on initial state radiation. θ is defined as follows. Let p_A and p_B be the momenta of the incoming hadrons in the rest frame of the top-antitop pair. If the transverse momentum of the top-antitop pair is non-zero, then p_A and p_B are not collinear. The angle θ is defined to be the angle between the axis that bisects the angle between p_A and p_B and the top quark momentum in the $t\bar{t}$ rest frame.

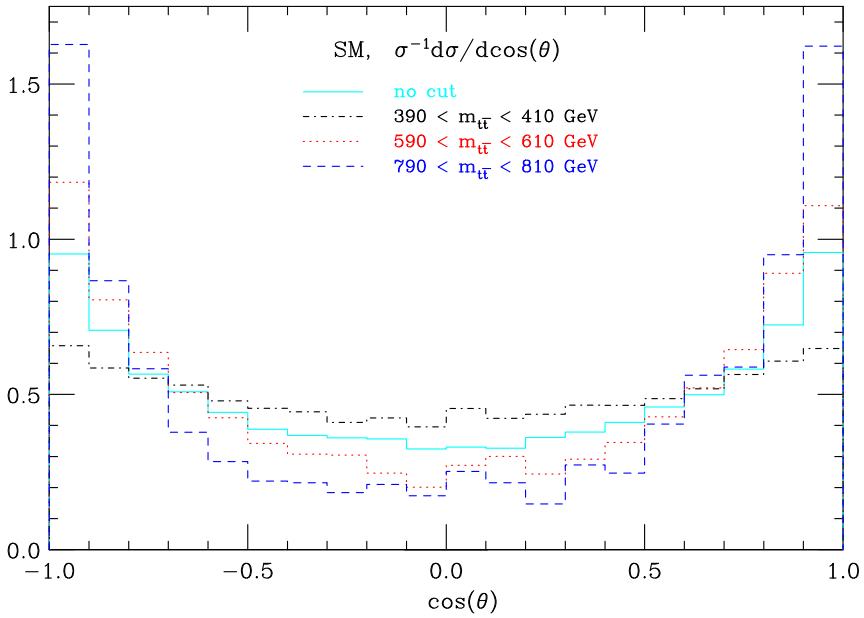

Figure 2.16: Normalized distribution for $\cos\theta$, where θ is the Collins-Soper angle, for SM production at the LHC. Different lines represent different cuts on $t\bar{t}$ invariant mass.

2.4.1 Standard Model

The distribution of θ in the SM is plotted in Fig. 2.16. Also plotted in the same figure are the distributions with cuts on the $t\bar{t}$ invariant mass spectrum as backgrounds to narrow resonances.

A simple analytic calculation confirms this behavior. The matrix element squared for the initial state $q\bar{q}$ to the SM $t\bar{t}$ contribution in terms of the Collins-Soper angle $\cos\theta$ is proportional to

$$|\mathcal{M}(q\bar{q} \to t\bar{t})|^2 \sim s(1+\cos^2\theta) + 4m_t^2(1-\cos^2\theta), \tag{2.7}$$

where s is the center of mass energy squared, $s = (p_q + p_{\bar{q}})^2$. For the gg initial state we have

$$|\mathcal{M}(gg \to t\bar{t})|^2 \sim \frac{s(7 + 9\cos^2\theta) - 36m_t^2\cos^2\theta}{\left(sc_- + 4m_t^2\cos^2\theta\right)^2}\Big[s^2c_+c_- + 2sm_t^2\Big(3c_-^2 + c_+^2\Big) - 4m_t^4\Big(3c_-^2 + c_+^2 + c_-\Big)\Big], \quad (2.8)$$

where $c_+ = 1 + \cos^2\theta$ and $c_- = 1 - \cos^2\theta$.

2.4.2 Spin-0 resonances

In Fig. 2.17(a) the normalized cross section as a function of $\cos\theta$ is plotted for a spin-0 resonance. The distribution is independent of the mass and parity of the resonance. The matrix element squared for the spin-0 resonance H is at leading order proportional to

$$|\mathcal{M}(gg/q\bar{q} \to H \to t\bar{t})|^2 \sim (|a_1|^2 + |a_2|^2)p_t \cdot p_{\bar{t}} - (|a_1|^2 - |a_2|^2)m_t^2, \quad (2.9)$$

where p_t and $p_{\bar{t}}$ are the momenta of the top and anti-top quarks, respectively, and a_1 and a_2 are the coupling constants, see Eq. 2.5, for the scalar and pseudo-scalar, respectively. The matrix element squared is clearly independent of the angle $\cos\theta$, which explains the flat distribution.

2.4.3 Spin-1 resonances

For a generic spin-1 resonance Z' the matrix element squared is proportional to

$$|\mathcal{M}(q\bar{q} \to Z' \to t\bar{t})|^2 \sim 2(|a_L|^4 + |a_R|^4)p_q \cdot p_{\bar{t}}\; p_{\bar{q}} \cdot p_t + 4|a_L|^2|a_R|^2 p_q \cdot p_t\; p_{\bar{q}} \cdot p_{\bar{t}} + m_t^2(|a_L|^2 + |a_R|^2)(a_L a_R^* + a_R a_L^*)p_q \cdot p_{\bar{q}}, \quad (2.10)$$

where a_L and a_R are the left and right handed part of the couplings of the Z' resonance to quarks, *i.e.*, $g_{Z'q\bar{q}} \sim a_L\frac{1-\gamma_5}{2} + a_R\frac{1+\gamma_5}{2}$ and where p_q and $p_{\bar{q}}$ are the momenta of the incoming quark and anti-quark, respectively. In terms of $\cos\theta$ the matrix element squared is proportional to

$$|\mathcal{M}(q\bar{q} \to Z' \to t\bar{t})|^2 \sim (|a_L|^2 + |a_R|^2)(s - 4m_t^2)(1 + \cos^2\theta) + 4m_t^2|a_L + a_R|^2. \quad (2.11)$$

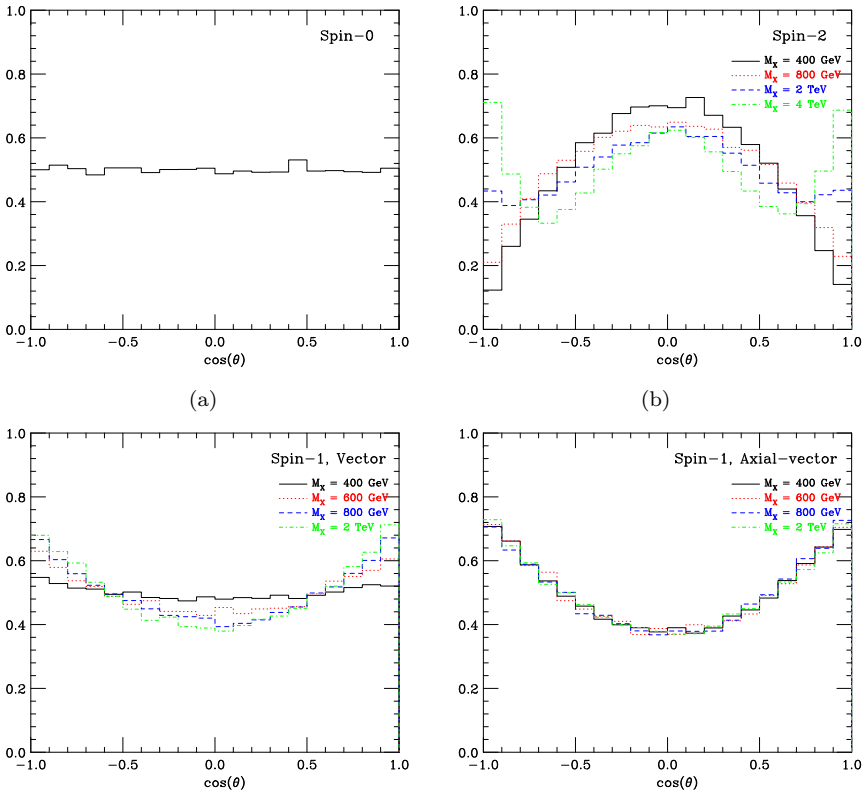

Figure 2.17: Normalized distributions for $\cos\theta$, where θ is the Collins-Soper angle, for spin-0 (a), spin-2 (b), vector (c) and axial-vector (d) resonances of mass M_X. All plots were produced using the `CTEQ6L1` PDF set with $\mu_R = \mu_F = M_X$.

The normalized $\cos\theta$ distribution is independent of the mass of the resonance for an axial vector, $a_R = -a_L$ (see Fig. 2.17(d)), while for a pure vector resonance the dependence is maximal Fig. 2.17(c). However, for heavy resonances, $M_X \gtrsim 800$ GeV the difference between the curves for the vector and the axial-vector is less then 8% which makes it challenging to get any information about parity of the coupling from this distribution. In Ref. [126] a similar polar angle has been studied. That polar angle is also sensitive to the chirality of the coupling. However, the Collins-Soper angle used here has the advantage that it minimizes the effects from initial state radiation.

2.4.4 Spin-2 resonances

In the case of the spin-2 resonance $G_{\mu\nu}$, both the $q\bar{q}$ and gg initial states contribute. The matrix element squared for the $q\bar{q}$ initial state is proportional to

$$|\mathcal{M}(q\bar{q} \to G_{\mu\nu} \to t\bar{t})|^2 \sim s(1 - 3\cos^2\theta + 4\cos^4\theta) + 16m_t^2\cos^2\theta(1 - \cos^2\theta), \quad (2.12)$$

and for the gg initial state

$$|\mathcal{M}(gg \to G_{\mu\nu} \to t\bar{t})|^2 \sim \Big[s(1+\cos^2\theta) + 4m_t^2(1-\cos^2\theta)\Big](1-\cos^2\theta). \quad (2.13)$$

The large differences in the distributions for the spin-2 resonances between light compared to heavy spin-2 particles, see Fig. 2.17(b), is due to the fact that the relatively light spin-2 particles are mainly produced by gluon fusion, while the very heavy spin-2 particles by quark-antiquark annihilation.

2.5 Spin correlations in (anti-)top-quark decays

In the Standard Model, the top-quark decay width is rather large $\Gamma \approx 1.5$ GeV $> \Lambda_{QCD}$ and top quarks do not form bound hadronic states. At present, we do not have any direct measurement of the top width and the formation of top hadrons is not excluded. This could happen for example, if V_{tb} were much smaller than what is predicted in the Standard Model, as discussed in Ref. [89]. Note, however, that even if this were to happen, the information on the spin of the top quark would be anyway fully inherited by its decay products [127], as spin-flip would occur at time scales of the order m_t/Λ_{QCD}^2, *i.e.*, much later than the lifetime of the top quark. In this respect, spin correlation effects are a very robust probe of new physics entering in the production cross section.

For Standard Model leptonic top decays, the directions of the leptons are 100% correlated with the polarization of the top quarks and therefore their spin analyzing power[‡] is equal to one. The spin analyzing power of the direction of the b quark (W^+ boson) is not as good, around -0.4 (0.4). In hadronic top decays the anti-down (or anti-strange) quarks coming from the W^+ boson decay have the same full spin analyzing power as the lepton. On the other hand, the up (or charm) quarks have a spin analyzing power of only -0.3, *i.e.*,

[‡]The spin analyzing power is a measure for the how well the direction of the decay product is related to the spin of the top quark.

the same as the neutrino in leptonic decays. For the decay of anti-top quarks or spin-down top quarks, all spin analyzing powers change sign. The angular distributions of the two down-type fermions (leptons in leptonic top decays or jets coming from down-type quarks in hadronic W decays) give maximal information about the spin of the (anti-)top quarks in $t\bar{t}$ events [128, 129].

In studies on the spin correlations in $t\bar{t}$ production, two distributions are usually considered [36, 98]. First the distribution

$$\frac{1}{\sigma}\frac{d^2\sigma}{d\cos\theta_+ d\cos\theta_-} = \frac{1}{4}\Big(1 - A\cos\theta_+\cos\theta_- + b_+\cos\theta_+ + b_-\cos\theta_-\Big), \quad (2.14)$$

where θ_+ (θ_-) is the angle between the t ($\bar{t}$) direction in the $t\bar{t}$ center of momentum frame and the f_d^+ (f_d^-) direction in the t ($\bar{t}$) rest frame, where f_d^+ (f_d^-) is the down-type fermion coming from the W^+ (W^-) decay. For a parity conserving $t\bar{t}$ production mechanism, such as QCD, the parameters b_+ and b_- vanish. In practice, the way to construct these angles is first to construct the t and $\bar{t}$ four-momenta in the laboratory frame. Then perform a rotation-free boost from the laboratory frame to the $t\bar{t}$ center of momentum frame to define the t ($\bar{t}$) direction in the $t\bar{t}$ center of momentum frame. Thirdly, boost the down-type fermion momenta, *i.e.*, the lepton in leptonic top decays and the down-type quark in hadronic W decays, from the $t\bar{t}$ center of momentum rotation-free to the t and $\bar{t}$ rest frames. If the t and $\bar{t}$ rest frames are constructed directly by boosting from the laboratory frame a Wigner rotation has to be taken into account [36].

Defining the angles θ_+ and θ_- as described above, corresponds to studying spin correlations of the $t\bar{t}$ pair in the helicity basis.

It is important to stress that in spin correlation studies it is mandatory to reconstruct the top and the anti-top quark momenta. In the case of a double leptonic decay, two neutrino's are emitted and the full reconstruction of the event becomes non trivial. Imposing kinematic constraints, such as the known top and W masses, a constrained system of equations for the neutrino momenta can be set up. In general multiple solutions arise and the best solution can be only obtained on a statistical basis [79, 98, 130–133]. In Sec. 2.7 some of the issues for the reconstruction are discussed in more detail. Alternatively, the single leptonic $t\bar{t}$ decay could be used by letting one of the jets of the hadronically decayed (anti-)top quark play the role of the lepton. Ideally, one would like to use the jet coming from the down-type quark, because it has the same (maximum) spin analyzing power as the lepton. In experiments one cannot easily distinguish between up- and down-type quarks jets on event-by-event basis, and the analyzing power gets averaged $(1-0.3)/2 \approx 0.35$. However,

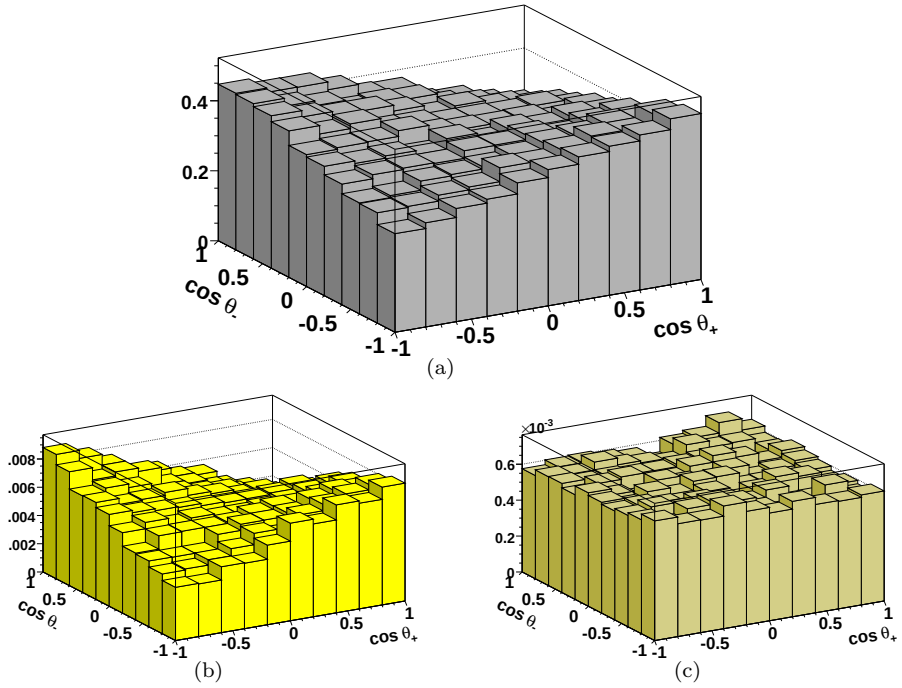

Figure 2.18: The distribution $\frac{1}{\sigma}\frac{d^2\sigma}{d\cos\theta_+ d\cos\theta_-}$ for SM $t\bar{t}$ production at the LHC, using PDF set `CTEQ6L1`, without applying cuts (a), and for the regions $390 < m_{t\bar{t}} < 410$ GeV (b) and $790 < m_{t\bar{t}} < 810$ GeV (c).

improvements can be achieved by exploiting the fact that down-type quark jets have in general a smaller transverse momentum than the up-type quark jets. Using the least energetic (non-b) jet from the hadronic top decay increases the spin-analyzing power from 0.35 to approximately 0.5 [36, 134]. For illustration purposes in the following we assume that the top quark momenta are correctly reconstructed and the spin analyzing power is maximal.

In Fig. 2.18 this distribution is plotted for QCD $t\bar{t}$ production.

The differences among the various $t\bar{t}$ production mechanisms are manifest. In Fig. 2.19 the distributions are plotted for resonance masses of 800 GeV for the following states:

- Scalar boson (a),
- Pseudo-scalar boson (b),
- Vector boson (c),

- Axial-vector boson (d),
- Vector-left boson (e),
- Vector-right boson (f),
- Spin-2 boson (g).

With the vector-left and vector-right we understand a spin-1 vector boson that couples *only* to left- or right-handed fermions, respectively. We choose very narrow resonances by taking the width of resonances to be 1% of the mass, *i.e.*, 8 GeV for a mass of 800 GeV. We do not include the SM QCD $t\bar{t}$ production background in these plots.

In Table 2.2 the distributions are fitted to Eq. (2.14) and compared with analytic computations. For the sake of simplicity, in the analytic computations the off-diagonal elements of the spin correlations matrix in the helicity basis are neglected. This means that the interference between different top quark spins are not included. In fact, the interference effects are negligible and the fitted values agree very well with the analytic computations. For completeness we also included the numbers for a smaller resonance mass, $M_X = 400$ GeV, where the effects from the mass of the top play a larger role.

The second angle, which is commonly considered when studying spin correlations in $t\bar{t}$ production is ϕ, *i.e.*, the angle between the directions of the f_d^+ and f_d^- in the t and $\bar{t}$ rest frames, respectively. The distribution

$$\frac{1}{\sigma}\frac{d\sigma}{d\cos\phi} = \tfrac{1}{2}(1 - D\cos\phi), \tag{2.15}$$

for this angle is plotted in Fig. 2.20 for a resonance mass of 800 GeV.

The distributions for the angle ϕ are the same for production through a scalar and a vector boson. The distribution for the pseudo-scalar, on the other hand, is completely different from the one for the scalar and the vector boson [111]. Also, the angular distribution for SM $t\bar{t}$ production is different from the other production mechanisms. In the case of a spin-1 state, the ϕ distribution is independent of the type of coupling to the top: it makes no difference whether it is pure vector, an axial-vector, a left-handed or right-handed couplings.

2.6 Non-resonant BSM effects

There are also non-resonant BSM processes that could effect the $t\bar{t}$ invariant mass spectrum. In this section we consider $t\bar{t}\phi$ production, where ϕ is an

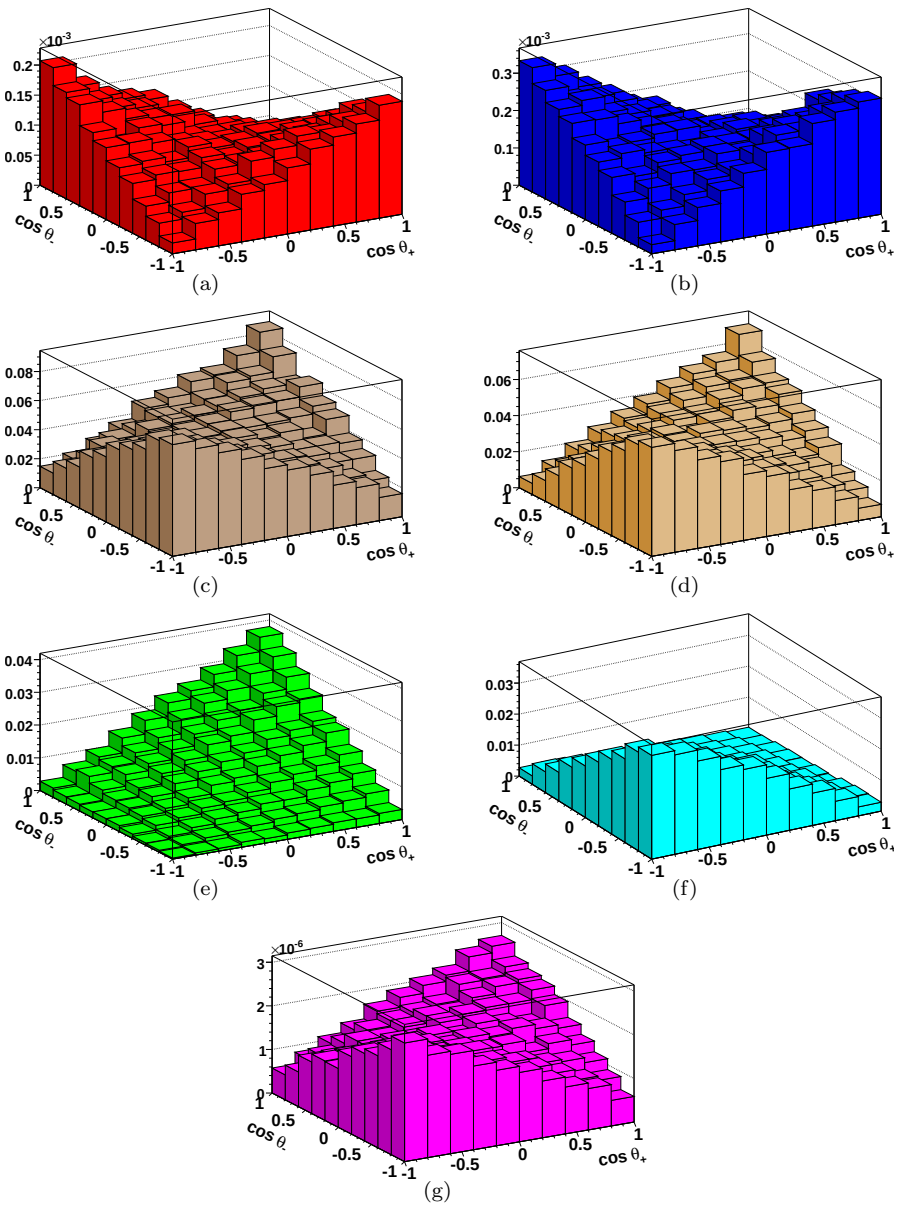

Figure 2.19: The distribution $\frac{1}{\sigma}\frac{d^2\sigma}{d\cos\theta_+ d\cos\theta_-}$ for (a) scalar, (b) pseudo-scalar, (c) vector, (d) axial-vector, (e) vector-left, (f) vector-right, (g) spin-2. $M_X = 800$ GeV at the LHC, using the PDF set `CTEQ6L1`. No cuts were applied.

invisible scalar, and the SUSY process stop–anti-stop pair production where the (anti-)stops decay in (anti-)tops and neutralinos which are not detected. Again, we apply no cuts to the final state particles and assume that the $t\bar{t}$ invariant mass can be fully reconstructed, in all models. Because of this last requirement these two examples can be considered as academic, as it will be extremely challenging, if not impossible, to reconstruct the $t\bar{t}$ invariant mass unambiguously if there are BSM missing particles in the events.

2.6.1 Invisible (pseudo-)scalar

Normally, looking for missing E_T is the simplest way to get information about invisible particles. But there are also other indirect ways of detecting these particles and extract their properties. Here we consider the process $pp \rightarrow t\bar{t}\phi$, see Fig. 2.21, where the ϕ is a (pseudo) scalar which is not detected and considered to couple only to top quarks. If it is lighter than twice the top quark mass it cannot decay, and it will pass through a detector unobserved. The $t\bar{t}$ invariant mass spectrum will be different for this three body final state. First of all, the total cross section will change dramatically as a function of the mass of this invisible (pseudo) scalar particle, see Table 2.3. For this table we

resonance	mass (GeV)	A calc.	A fit.	b_+ calc.	b_+ fit.	b_- calc.	b_- fit.
sm	–	0.319	0.304	0	0.008	0	-0.003
sm	$390 < m_{t\bar{t}} < 410$	0.501	0.532	0	0.004	0	0.005
sm	$790 < m_{t\bar{t}} < 810$	-0.061	-0.051	0	-0.014	0	-0.011
scalar	400	1	0.972	0	0.005	0	0.007
pseudo-scalar	400	1	0.966	0	0.007	0	0.002
vector	400	-0.449	-0.432	0	0.008	0	-0.004
axial-vector	400	-1	-0.990	0	-0.004	0	0.002
vector-left	400	-0.531	-0.536	0.605	0.607	0.605	0.600
vector-right	400	-0.531	-0.558	-0.605	-0.604	-0.605	-0.610
spin-2	400	–	-0.348	0	0.001	0	0.006
scalar	800	1	0.985	0	-0.015	0	0.004
pseudo-scalar	800	1	0.978	0	-0.004	0	-0.004
vector	800	-0.826	-0.819	0	0.008	0	0.005
axial-vector	800	-1	-1.001	0	0.008	0	0.008
vector-left	800	-0.900	-0.912	0.945	0.955	0.945	0.946
vector-right	800	-0.900	-0.884	-0.945	-0.938	-0.945	-0.943
spin-2	800	–	-0.743	0	0.022	0	0.013

Table 2.2: $\frac{1}{\sigma}\frac{d^2\sigma}{d\cos\theta_+ d\cos\theta_-} = \frac{1}{4}(1 - A\cos\theta_+\cos\theta_- + b_+\cos\theta_+ + b_-\cos\theta_-)$. For a top mass of 175 GeV. In the analytic calculation of the parameters, the interference between the various top spins is neglected.

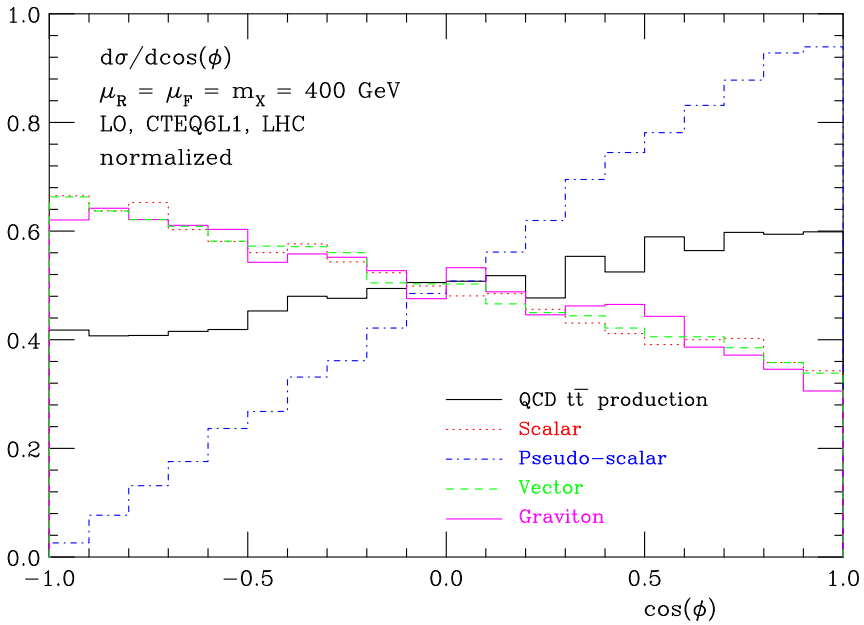

Figure 2.20: Distribution for the angle ϕ, defined in the text, for different $t\bar{t}$ production mechanisms at the LHC. *Dark Solid* line is the SM $t\bar{t}$ production, *dotted line* is $t\bar{t}$ production through a scalar, *dot-dashed* line is $t\bar{t}$ production through a pseudo-scalar, *dashed* line is $t\bar{t}$ production through a vector (this is independent of the coupling). The *light solid* line is $t\bar{t}$ production through a graviton. The plots are normalized. The PDF set `CTEQ6l1` is used with M_X = 800 GeV and $\mu_R = \mu_F$ = 800 GeV.

assumed that the ϕ couples to the top quarks with a strength equal to the SM coupling strength of the Higgs boson, *i.e.* $a_1 = 1$, $a_2 = 0$ for the scalar and $a_1 = 0$, $a_2 = 1$ for the pseudo-scalar in (2.5). To introduce a realistic model with a massless (or very light) (pseudo) scalar that couples only to top quarks and not, *e.g.*, to bottom quarks, is challenging. We will ignore this issue in the discussion below.

The overall normalization depends not only on the mass of the invisible (pseudo) scalar, but, of course, also on the coupling strength of this (pseudo) scalar to the top quarks. If we do not know this coupling strength we cannot use the total cross section to deduce information about the mass of the invisible scalar. However, the shape of the $t\bar{t}$ invariant mass distribution depends on the mass of ϕ. We can still distillate information about the mass of the invisible (pseudo) scalar from this distribution. In Fig. 2.22 the normalized $t\bar{t}$ invariant mass distributions for different ϕ masses are plotted.

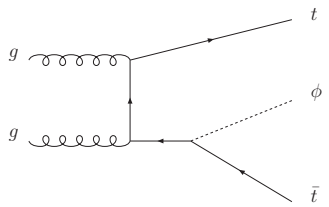

Figure 2.21: One of the diagrams contributing to $t\bar{t}\phi$ production.

For scalar masses smaller than about 70 GeV the $t\bar{t}$ invariant mass spectrum is slightly more peaked than the SM QCD $t\bar{t}$ production. For masses larger than 70 GeV the invariant mass spectrum is more flattened, but the differences remain small for masses up to about 120 GeV. However, if we keep increasing the scalar mass, up to 200 GeV or even 400 GeV, we get big differences in shape, which could be used to extract the scalar mass, if the coupling of the ϕ to top quarks would be very large to have a sizable cross section and $t\bar{t}$ invariant mass can be reconstructed.

For the pseudo-scalar on the contrary, the discriminative power is much smaller. Over the whole range of pseudo-scalar mass between 0 and 400 GeV the shapes of the $t\bar{t}$ invariant mass spectrum are more or less the same.

m_ϕ (GeV)	σ(scalar) (pb)	σ(pseudo-scalar) (pb)
limit $m_\phi \to 0$	68.1	0.436
20	10.1	0.393
50	3.03	0.306
100	0.735	0.198
200	0.107	0.091
400	0.018	0.026
w/o (pseudo-)scalar (LO)	450	

Table 2.3: Leading order cross section for $pp \to t\bar{t}\phi$ for different Higgs masses. Higgs couples with SM strength to the top quarks. LO, `CTEQ6L1`, $\mu_R = \mu_F = 2m_t$, no cuts.

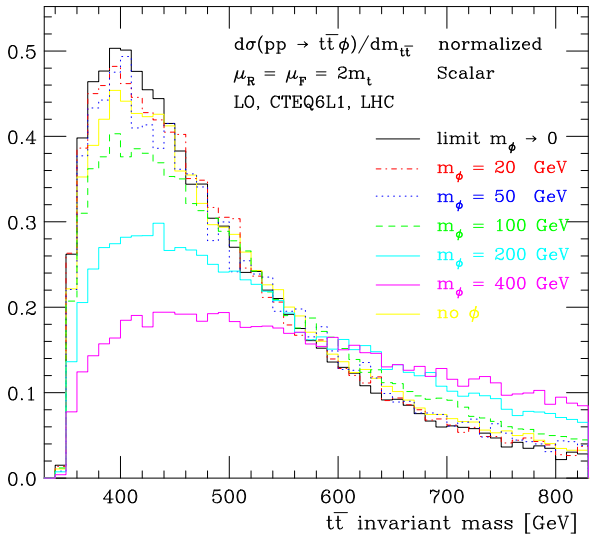

(a)

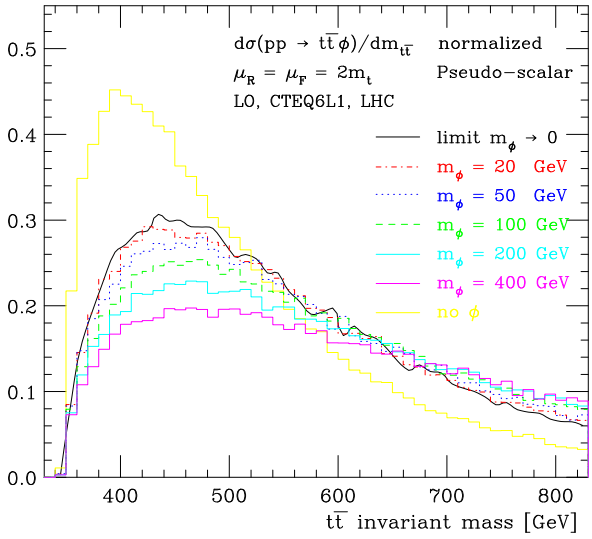

(b)

Figure 2.22: Invariant $t\bar{t}$ spectrum for $pp \to t\bar{t}\phi$ where ϕ is an invisible scalar (a) or an invisible pseudo-scalar (b). Plots are normalized. `CTEQ6L1`, $\mu_R = \mu_F = 2m_t$, no cuts.

2.6.2 $pp \to \tilde{t_1}\bar{\tilde{t}_1} \to t\bar{t}\tilde{\chi}_1^0\tilde{\chi}_1^0$

Here we study the SUSY process $pp \to \tilde{t_1}\bar{\tilde{t}_1} \to t\bar{t}\tilde{\chi}_1^0\tilde{\chi}_1^0$, see Fig. 2.23. We again look at the invariant $t\bar{t}$ spectrum and do nothing with the undetectable neutralinos. The invariant mass is plotted in Fig. 2.24. Here again we look at the shapes of the distributions, c.f. section 2.6.1 $pp \to t\bar{t}\phi$, where the ϕ decays invisibly.

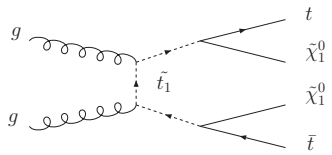

Figure 2.23: One of the diagrams contributing to $t\bar{t}\chi_0\chi_0$ production.

In figure 2.24 the *left-* (*right-*)hand side show the invariant $t\bar{t}$ mass distribution, based on the benchmark point sps1a (sps1b) defined in [135]. The colored lines represent the same process for different neutralino masses. This is the *only* difference between the lines. All other parameters are kept the same. Even the width of the stops are not adjusted to the different masses.

- sps1a: Stop mass $m_{\tilde{t_1}} = 400$ GeV, neutralino mass $m_{\tilde{\chi}_1^0} = 96.7$ GeV.
- sps1b: Stop mass $m_{\tilde{t_1}} = 660$ GeV, neutralino mass $m_{\tilde{\chi}_1^0} = 162$ GeV.

The total cross section for this process depends on the benchmark point as well as the neutralino mass. In Table 2.4 the overall sizes of cross sections are listed.

The shape and the total cross section do not change very much for relatively small neutralino masses. Only if the neutralino mass is larger than about 30-40% of the stop mass the shape of the invariant $t\bar{t}$ mass distribution changes. Also, for larger neutralino masses the distribution becomes more and more peaked, which is the opposite of what is happening in section 2.6.1 for larger masses of the invisible scalar.

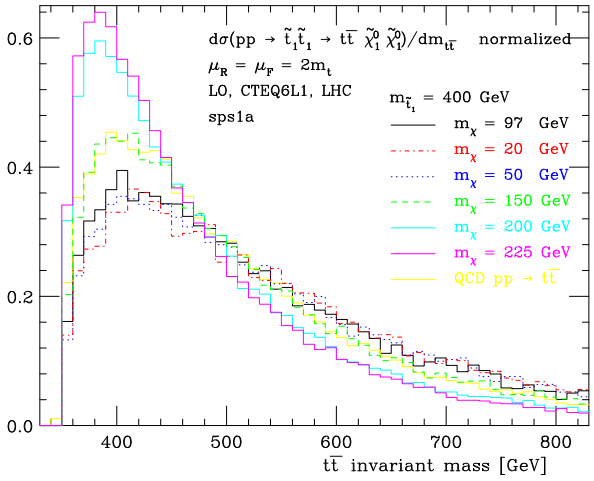

(a)

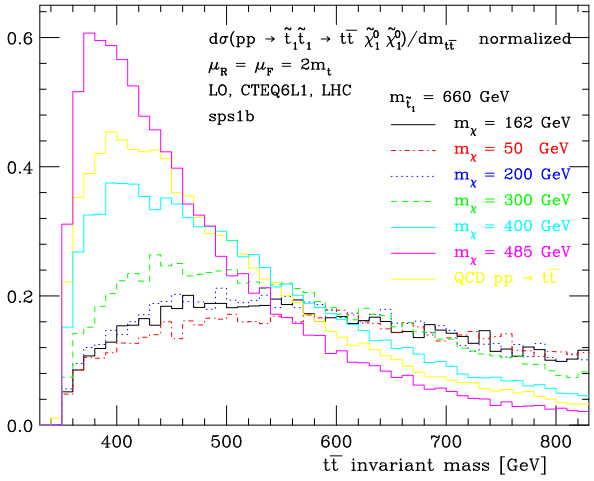

(b)

Figure 2.24: Invariant $t\bar{t}$ mass spectrum for the process $pp \to \tilde{t}_1\bar{\tilde{t}}_1 \to t\bar{t}\tilde{\chi}_1^0\tilde{\chi}_1^0$. In Fig. a (b) the *black* line corresponds to the sps1a (sps1b) benchmark point. Plots are normalized. `CTEQ6L1`, $\mu_R = \mu_F = 2m_t$, no cuts.

2.7 Reconstruction issues in $t\bar{t}$ events

In this section we address some of the issues arising in the reconstruction of the $t\bar{t}$ events and in particular their different impact in the three-step analyses proposed above.

For a generic $2 \to 6$ process, where the final state particles masses are known, 16 independent variables are needed to determine the kinematics of the event: the six final state particle three-momenta, $\{\mathbf{p}_i\}$, the two energy fractions carried by the initial state partons, $x_{a,b}$, minus the overall momentum conservation which reduces the number of independent variables by 4, leads to $6 \times 3 + 2 - 4 = 16$.

From the measured angles and energies of the final state particles, together with constraints from W boson and top quark masses, a system of equations can be set up to solve for the 16 unknown variables on an event-by-event basis.

The three decay modes of the $t\bar{t}$ pairs face each their own challenges for detection and reconstruction. Around 44% of the $t\bar{t}$ pairs decay hadronically, 30% of the $t\bar{t}$ pairs decay single-leptonically and 5% double leptonic (not including

	Neutralino mass (GeV)	Cross section (fb)
sps1a	97	54.8
	20	80.8
	50	73.8
	150	27.8
	200	6.71
	225	0.095
sps1b	162	5.35
	50	6.84
	200	4.56
	300	2.73
	400	0.68
	485	0.0035
SM $t\bar{t}$ production (LO)		4.50×10^5

Table 2.4: Leading order cross section for $pp \to \tilde{t_1}\bar{\tilde{t_1}} \to t\bar{t}\tilde{\chi}_1^0\tilde{\chi}_1^0$ for different neutralino masses. Benchmark points sps1a and sps1b, with *only* the neutralino masses changing. LO, `CTEQ6L1`, $\mu_R = \mu_F = 2m_t$, no cuts.

tau's) [98][§]. These three channels offer very different challenges related to the detection of final state particles and the reconstruction the (anti-)top quark momenta, which we will now address channel-by-channel.

The *fully-hadronic* decays have the advantage that in principle the momenta of all the final state particles can be determined, leading to $6 \times 3 = 18$ measurements. Together with the four mass constraints the system of equations for the 16 independent variables is over-constrained. Such constraints can be used in two ways. First they can be used to extract information, typically the jet energies, that have bad detector resolution. For example, measuring only the angles (θ, ϕ) of the six jets and including all the constraints from the top quark and W boson masses would already provide the required 16 independent quantities (although with combinatorics). Alternatively, the constraints from the masses can also be used to solve the combinatorics in reconstructing the W boson and (anti-)top quark momenta. Combinatorics, affect each of the three steps in the analysis proposed in this chapter in a different way. In the first step, *i.e.*, the measurement of the $t\bar{t}$ invariant mass, Sec. 2.3, combinatorics play no role: the invariant mass can be calculated by summing all the final state momenta irrespective of assigning jets to top or anti-top quarks, W^+ or W^- bosons. In the second step, *i.e.* the measurement of the spin of an intermediate resonance, Sec. 2.4, there is in principle a 12-fold ambiguity (assuming b-tagging) in assigning the correct (b-)jets to the top or anti-top quark. These ambiguities could be solved (in case of a very good jet energy resolution) or anyway alleviated by using the constraints from the top quark and W masses. In the third step, *i.e.*, the measurement of the spin correlations of the top anti-top pair, Sec. 2.5, not all ambiguities can be solved: in any case is not possible to uniquely identify on an event-by-event basis which of the two jets come from the down-type quarks in the W boson decays. Experimentally, the fully-hadronic decay is difficult to trigger and extract from multi-jet backgrounds, which makes this channel challenging for BSM physics studies. [136]

The *single-lepton* decay channel is much more promising. The single lepton in the final state greatly improves the possibility for triggering on these events and extracting it from backgrounds compared to the fully-hadronic decay mode. The presence of a missing neutrino in the final state entails that only $5 \times 3 = 15$ independent measurements can be obtained, one short of 16 necessary. The missing information can be recovered by including a constraint coming from, *e.g.*, the W boson mass (up to a two-fold quadratic ambiguity, which can be solved in various ways, *e.g.*, see Ref. [126]). Using also the constraint from the top mass removes the ambiguity for assigning the correct b-jet to the top quark

[§]The remaining 21% are events including decays to tau's, which are not be considered here.

needed for second and third step in our analysis. For the third step, however, it is still non-trivial to solve the ambiguity coming from assigning the correct jet to the down-type quark in the non-leptonic W decay. Several methods have been proposed, including, for example choosing the least energetic non-b-jet [36, 134]. Given its rate and the various reconstruction studies and possibilities, the single-lepton channel is the most straightforward search channel for BSM physics in $t\bar{t}$ events.

In the *double-lepton* decay mode there are two missing neutrino's in the final state. This makes the reconstruction of the full event kinematics challenging but certainly not impossible [79,98,130–133]. There are four visible particles in the final state, two b-jets and two opposite sign leptons, leading to $4 \times 3 = 12$ independent measurements. The additional four constraints from the W boson and top quark masses are just enough to set up a system of non-linear equations to solve for the necessary 16 variables. It can be shown that this system has up to eight solutions [131], of which, in general, only a few are physical and can be discarded or included based on their likelihood. It has to be noted that each solution has no further ambiguities and the event is completely reconstructed. For this reason, despite the small branching ratio, this channel competes in reach with the single-lepton in the studies of the spin correlation studies in $t\bar{t}$ [98, 137].

2.8 Conclusions

Given the large number of the models proposed and their complexity, a "top-down" approach, *e.g.*, model parameter scanning, will not be practical, in particular if a comparison of many different channels and observables at once will be necessary. As an alternative, a simpler and more pragmatic "bottom-up" approach could be employed, whereby one identifies specific observables which can be developed as tools for discriminating generic features of new physics resonances, thus keeping the analysis as model independent as possible.

In this chapter we have presented an example on how such a study could be performed for the invariant mass distribution of the $t\bar{t}$ pair.

As a first step we have assessed the accuracy of the best theoretical predictions available for $t\bar{t}$ production at hadron colliders. We have found that the shape of the distribution is under good theoretical control, especially at low invariant mass values, suggesting also the possibility of a precise top mass extraction.

We have then identified the features of new physics scenarios, namely the existence of heavy bosonic resonances of various spin, color and parity, that could

show up in the $m_{t\bar{t}}$ distribution, and implemented them in the `MadGraph/MadEvent` package. The full matrix elements, $pp \to X \to t\bar{t} \to 6f$, X being a spin-0, spin-1 or spin-2 particle, particles with arbitrary masses, width, color and couplings, have been automatically generated by `MadGraph`. The effects due to the interference with the $pp \to t\bar{t}$ SM process are included when relevant.

The strategy to gain information on new physics is then straightforward and consists of three successive steps:

I. The discovery of the resonance (and the determination of its mass and width) which could appear as a sharp or broad peak or as a more distinctive peak-dip structure in very specific cases. In this measurement the key aspect will be the experimental resolution in the $m_{t\bar{t}}$ reconstruction.

II. The identification of the spin of the resonance, which can be inferred from the angular distribution of the top and the anti-top.

III. Information on the couplings of the resonance to the top anti-top pair, which can be obtained by measuring the spin correlations of the top anti-top pair (for this last step the full matrix matrix element $2 \to 6$ is required).

In conclusion, we have outlined a simple strategy and provided the necessary Monte Carlo tools to search for new resonances in $t\bar{t}$ events.

CHAPTER

THREE

CONSTRAINING THE THIRD ROW OF THE CKM MATRIX WITH DIRECT MEASUREMENTS

3.1 Introduction

From the unitarity of the CKM matrix in the SM the third row of this matrix is very well constrained from precision measurement. The third element in the third row, $|V_{tb}|$ is constrained to be very close to unity, $0.9990 < |V_{tb}| < 0.9992$ at 95% C.L., while the other two elements are close to zero [138]. These rather precise values rely crucially on the unitarity of the 3×3 CKM matrix, which may not hold anymore in the presence of New Physics, *e.g.*, an extended quark flavor sector generally leads to an extended CKM matrix, of which the SM 3×3 sub-matrix could be non-unitary [89, 139].

There are indirect measurements, *e.g.*, the ratio of the oscillation frequencies ΔM_{B_d} and ΔM_{B_s}, that constrain the third row of the CKM matrix, see *e.g.* Refs. [89–91], and do, in principle, not rely on unitarity. However, these loop–induced processes can be polluted by New Physics which means that the bounds derived from these processes depend on the physics model. To constrain the allowed parameter space for $|V_{td}|$, $|V_{ts}|$ and $|V_{tb}|$ in a model independent way, only direct measurements can be used.

In Sec. 3.2 the most minimal extensions of the SM that relaxes the unitary constraints on the CKM matrix are introduced. A deviation of V_{tb} from its SM value is seriously restricted by flavor and EW precision measurements, but

the precise details of the model are needed to set these bounds. In Sec. 3.3 the details of the model are ignored and only direct measurements are used to set bounds on the third row of the CKM matrix in Sec. 3.4. We conclude in Sec. 3.5.

3.2 Minimal New Physics models with extended CKM matrices

3.2.1 Vector-like t'

The most minimal extension of the Standard Model having an extended CKM matrix contains a new heavy vector-like quark state, generally called t' with electric charges $Q = +2/3$ [89]. This singlet under the $SU(2)_{\rm L}$ gauge group* naturally mixes with the SM top quark if the mass of this new quark is close to the electroweak scale. This results in a 4×3 extended CKM matrix:

$$\mathbf{V}_{4\times3} = \begin{pmatrix} \mathbf{1}_{2\times2} & \mathbf{0}_{2\times2} \\ \mathbf{0}_{2\times2} & \mathbf{U}_{2\times2} \end{pmatrix} \begin{pmatrix} \mathbf{V}^{\rm SM}_{3\times3} \\ \mathbf{0}_{1\times3} \end{pmatrix}, \tag{3.1}$$

where $\mathbf{V}^{\rm SM}_{3\times3}$ is the unitary SM CKM matrix. For a general unitary $\mathbf{U}_{2\times2}$ matrix, the new extended 4×3 CKM matrix is not unitary, $\mathbf{V}_{4\times3}(\mathbf{V}_{4\times3})^\dagger \neq \mathbf{1}_{4\times4}$.

Here, $\mathbf{V}_{4\times3}$ enters in the flavor changing charged current

$$\mathcal{L}_{W^\pm} = -\frac{g}{\sqrt{2}}[\bar{u}_L \mathbf{V}_{4\times3} \gamma^\mu d_L W^+_\mu + h.c.]. \tag{3.2}$$

Note that such an enlargement does not spoil the unitarity of the first two rows of the CKM matrix. If we neglect possible CP-violating phases beyond CKM, the left-handed unitary transformation leading to the physical t and t' quarks is a simple rotation in the $3-4$ flavor plane

$$\mathbf{U} = R_{34}(\theta) = \begin{pmatrix} \cos\theta & -\sin\theta \\ \sin\theta & \cos\theta \end{pmatrix} \tag{3.3}$$

such that

$$V_{ti} = V^{\rm SM}_{ti} \cos\theta, \tag{3.4}$$

$$V_{t'i} = V^{\rm SM}_{ti} \sin\theta, \tag{3.5}$$

*Because a vector-like quark has no weak isospin charge it does not contribute to the axial anomaly, see Sec. 1.1.1, and therefore it does not hamper the renormalizability of this model.

with $V_{tb}^{\rm SM} \simeq 1$. We are therefore left with only two new parameters beyond the SM, namely the $t - t'$ mixing angle θ and the t' mass $m_{t'}$.

This model allows V_{tb} to be smaller than one but also implies tree-level flavor changing neutral currents (FCNC)

$$\mathcal{L}_{Z^0}(\theta) = -\frac{g}{2\cos\theta_{\rm W}} \bar{u}_L \mathbf{V}_{4\times3}(\mathbf{V}_{4\times3})^\dagger \gamma^\mu u_L Z^0_\mu \tag{3.6}$$

$$\mathcal{L}_{H^0}(\theta, m_{t'}) = \frac{g}{2M_W}[\bar{u}_L \mathbf{V}_{4\times3}(\mathbf{V}_{4\times3})^\dagger \mathbf{M}^u u_R + h.c.]H^0 \tag{3.7}$$

with

$$\mathbf{V}_{4\times3}(\mathbf{V}_{4\times3})^\dagger = \begin{pmatrix} \mathbf{1}_{2\times2} & \mathbf{0}_{2\times1} & \mathbf{0}_{2\times1} \\ \mathbf{0}_{1\times2} & \cos^2\theta & \sin\theta\cos\theta \\ \mathbf{0}_{1\times2} & \sin\theta\cos\theta & \sin^2\theta \end{pmatrix} \quad \text{and} \tag{3.8}$$

$$\mathbf{M}^u = \mathrm{diag}(m_u, m_c, m_t, m_{t'}). \tag{3.9}$$

Notice that the Z coupling to $t\bar{t}$ is reduced by a factor of $\cos^2\theta$. The non-observation of the FCNC processes potentially restricts the off-diagonal elements of $\mathbf{V}_{4\times3}(\mathbf{V}_{4\times3})^\dagger$ and consequently constrains the $t - t'$ mixing angle θ. In fact, current limits on FCNC involving the top quark only constrain the Ztu and Ztc couplings [140].

(Indirect) constraints from precision measurements

Both flavor physics and electroweak precision measurements constrain the mixing angle θ and therefore the third (and fourth) rows of the CKM matrix. The strongest constraint from flavor physics is coming from the branching ratio $\mathrm{Br}(B \to X_s\gamma) = (3.55 \pm 0.45) \times 10^{-4}$. This constrains the mixing angle to be larger than $|\cos\theta| > 0.5$ at 95% C.L. for $m_{t'} = 2m_t$, with stronger constraints for increasing t' masses [89].

Electroweak precision observables, like the oblique S, T and U parameters also constrain the mixing between the vector-like t' quark and top quark. The most stringent constraint is coming from the ratio $R_b = \Gamma(Z \to b\bar{b})/\Gamma(Z \to \text{hadrons})$ [141], leading to a lower bound on $|V_{tb}|$ of

$$|V_{tb}| = |\cos\theta\, V_{tb}^{\rm SM}| \gtrsim 0.91 \quad \text{at 95 \% C.L.} \tag{3.10}$$

for $m_{t'} = 1.5m_t$ and increasing with increasing t' mass [89].

Note that the t' mass has been constraint by direct searches at the Tevatron collider. Recently, CDF announced a new bound, $m_{t'} > 311$GeV at 95%

C.L. [142]. In this analysis it is assumed that the t' quark decays exclusively to Wq. However, this is a rather strong assumption in a model with a general CKM matrix, because we have seen that there could be FCNCs with t' quarks decaying to other quarks in association with Z or H bosons, Eq. (3.6) and (3.7). For a plot of the branching ratios, see *e.g.*, Fig. 1 of Ref. [89].

3.2.2 Fourth generation

The next-to minimal extension of the Standard Model with an extended CKM matrix is the addition of a fourth generation. In this case, both a t' and a b' that form a $SU(2)_{\mathrm{L}}$ doublet and their singlet right-handed partners are introduced. The presence of the b' implies a unitary $\mathbf{V}_{4\times4}$ mixing matrix such that tree-level FCNCs are forbidden.

Neglecting again the CP-violating phases beyond CKM, the 4×4 unitary matrix contains three extra mixings which we parametrize, following Ref. [143], as

$$\mathbf{V}_{4\times4} = R_{34}(\theta_u)R_{24}(\theta_v)R_{14}(\theta_w)\begin{pmatrix} \mathbf{V}^{\mathrm{SM}}_{3\times3} & \mathbf{0}_{3\times1} \\ \mathbf{0}_{1\times3} & 1 \end{pmatrix}, \tag{3.11}$$

where $R_{ij}(\theta)$ is the rotation in the $i-j$ flavor plane. We then obtain (for $i = d, s, b$)

$$V_{ui} = \cos\theta_w V^{\mathrm{SM}}_{ui} \tag{3.12}$$
$$V_{ci} = \cos\theta_v V^{\mathrm{SM}}_{ci} - \sin\theta_v \sin\theta_w V^{\mathrm{SM}}_{ui} \tag{3.13}$$
$$V_{ti} = \cos\theta_u V^{\mathrm{SM}}_{ti} - \sin\theta_u \sin\theta_v V^{\mathrm{SM}}_{ci} - \sin\theta_u \cos\theta_v \sin\theta_w V^{\mathrm{SM}}_{ui} \tag{3.14}$$
$$V_{t'i} = \sin\theta_u V^{\mathrm{SM}}_{ti} + \cos\theta_u \sin\theta_v V^{\mathrm{SM}}_{ci} + \cos\theta_u \cos\theta_v \sin\theta_w V^{\mathrm{SM}}_{ui}. \tag{3.15}$$

For a detailed discussion of this model and the indirect bounds and constraints on the CKM matrix we refer the reader to Refs. [89–91].

3.3 Direct constraints on $|V_{tb}|$

In the previous sections with the examples off minimal extensions to the Standard Model, electroweak precision measurements constrain the CKM matrix element $|V_{tb}|$ strongly. However, these indirect bounds depend on loop processes and are therefore sensitive to the precise definition of the New Physics model. One could imagine more elaborate models with more BSM particles running in the loops and cancelling some of the contributions described above.

A more solid constraint, valid in general extensions of the SM, can only be obtained from direct measurements. So far, direct constraints on the $|V_{tb}|$ matrix element can be derived from the measurements of top quark decays and single top cross section.

3.3.1 Top quark decay

The ratio R is defined to be the number of b-quark jets over the number of light quark jets in top quark decay,

$$R \equiv \frac{\mathrm{BR}(t \to Wb)}{\mathrm{BR}(t \to Wq)} = \frac{|V_{tb}|^2}{\sum_q |V_{tq}|^2}, \tag{3.16}$$

where the summation is over $q = d, s, b$. This ratio can be derived by considering the relative number of zero, one and two b-tagged jets in $t\bar{t}$ events at the Tevatron collider. The most stringent current bound for this ratio is coming from DØ [144]

$$R > 0.79 \text{ at } 95\% \text{ C.L.} \tag{3.17}$$

Note that the direct determination of $|V_{tb}|$ from R, $|V_{tb}| = \sqrt{R} > 0.89$ at 95% C.L. given in Ref. [144], assumes unitarity. As described already above, unitarity constrains $|V_{tb}|$ to be one and extraction of $|V_{tb}|$ from R is therefore not particularly interesting. However, the measurement of R does imply a hierarchy between the elements of the third row of the CKM matrix, $|V_{tb}|^2 > |V_{td}|^2 + |V_{ts}|^2$.

3.3.2 Single top production

The second direct constraint on $|V_{tb}|$ is coming from the measurement of the single top production cross section, which is in the SM directly proportional to $|V_{tb}|^2$. The measured cross sections by CDF [7, 145] and DØ [8] can be found in Table 3.1. The CDF separation of the single top measurement into s and t channel might not be entirely correct as explained later in Sec. 4.7.3. We therefore will not consider these separate measurements in the following. Both measurements for the total cross section are consistent with the SM prediction for the cross section at NLO [54, 146], *i.e.*, with $|V_{tb}| = 1$, although there is a slight tension between the measured values and the predictions, see Table 3.1.

Both DØ and CDF have used these measurements to determine the value of $|V_{tb}|$. However, to extract the signal events from the overwhelming backgrounds, the SM is assumed in their analyses. Note that not only for the signal

it is assumed that $R = 1$, but also for the large $t\bar{t}$ background. The extraction is therefore only correct if $|V_{tb}| \gg |V_{td}| + |V_{ts}|$, *i.e.*, $R \simeq 1$. Although current measurements prefer a large R, there is still a sizable uncertainty, see Eq. (3.17). This leaves plenty of room for non-zero $|V_{td}|$ and/or $|V_{ts}|$, which complicates the extraction of $|V_{tb}|$.

If $|V_{td}|$ (or to a lesser extent $|V_{ts}|$) is non-zero, the t-channel cross section could be significantly enhanced due to the possibility of single top production from valence down (or strange) quarks in the initial state. This would increase the measured t-channel single top production.

In the case of the s-channel production the average number of b-quarks in the final state is reduced if $|V_{td}| \neq 0$ and/or $|V_{ts}| \neq 0$. This would reduce the measured s-channel cross section, because the analyses require two b-jets. However, if there is still one b-quark in the final state, the events become very similar to the t-channel single top signature, for which there is only 1 b-jet required in the analyses. So, non-zero $|V_{td}|$ and/or $|V_{ts}|$ could reduce the measured s-channel and increase the t-channel single top productions.

The decay of the top quark is also altered for both t- and s-channel production processes if $|V_{tb}| \ll 1$ and $|V_{td}| \neq 0$ and/or $|V_{ts}| \neq 0$. A significant deviation from the SM value $R = 1$ is still allowed by the current bound on R from $t\bar{t}$ events, see Eq. (3.17). A low value for R would reduce the measured cross sections, because in the CDF and DØ analyses it is assumed that BR($t \to Wb$) = 1.

Taking into account the above considerations, a model independent discrimination between t- and s-channel from the number of b-quark jets in the final state cannot be made. The quoted measurements by the CDF and DØ collaborations (see Table 3.1) of the s- and t-channel cross sections cannot be directly related to the SM s- and t-channel production mechanisms, but only to $\sigma_{1b\text{-tag}}$

	CDF	DØ	Theory at NLO ($\|V_{tb}\| = 1$)
$\sigma^{t\text{-ch}} + \sigma^{s\text{-ch}}$ (pb)	$2.3^{+0.6}_{-0.5}$	3.94 ± 0.88	2.9 ± 0.4
$\sigma^{t\text{-ch}}$ (pb)	0.7 ± 0.5	N/A	2.0 ± 0.3
$\sigma^{s\text{-ch}}$ (pb)	$2.0^{+0.7}_{-0.6}$	N/A	0.9 ± 0.1

Table 3.1: Measured single top cross sections by CDF [7, 145] and DØ [8] and theory predictions at NLO [54, 146].

and $\sigma_{2b\text{-tag}}$ defined according to [9, 89]

$$\sigma_{1b\text{-tag}} = R\left\{\sum_{q=d,s,b}|V_{tq}|^2\alpha_q\sigma_q^{t\text{-ch}} + 2\beta(|V_{td}|^2+|V_{ts}|^2)\sigma^{s\text{-ch}}\right\} \tag{3.18}$$

$$\sigma_{2b\text{-tag}} = R|V_{tb}|^2\sigma^{s\text{-ch}}. \tag{3.19}$$

Here $\sigma^{s\text{-ch}}$ is the s-channel single top production and $\sigma_q^{t\text{-ch}}$ is the t-channel single top production where q is the incoming quark that couples through the CKM matrix to the top quark. R is the ratio defined in Eq. (3.16). The factors α_q and β correspond to the loss in selection efficiency due to the slightly different kinematics of the final state particles in s- and t-channel events. Monte Carlo simulations for single top events fix the values for the cross sections $\sigma_q^{t\text{-ch}}$ and $\sigma^{s\text{-ch}}$ and the efficiency factors α_q and β. Therefore the two measurements for $\sigma_{1b\text{-tag}}$ and $\sigma_{2b\text{-tag}}$ allow for a direct extraction of $|V_{tb}|$ and $|V_{ts}|^2+|V_{td}|^2$ from experiment. Unfortunately, as we will discuss in the next chapter, the Monte Carlo predictions used by CDF to make the distinction between $\sigma^{t\text{-ch}}$ and $\sigma^{s\text{-ch}}$, see Table 3.1, are not at NLO accuracy and we will not use these separate measurements to set bounds in the third row of the CKM matrix.

3.4 Bounds on $|V_{tb}|$ from direct measurements

Bounds on the third row of the CKM matrix coming from the above measurements of R and single top production are given in Figs. 3.1 and 3.2 using CDF and DØ data, respectively. In these plots it is assumed that the factors $\alpha_q = 1$ and $\beta = 1/2$ [†] and that the measured sum of the t- and s-channel cross sections (Table 3.1) is exactly equal to $\sigma_{1b\text{-tag}} + \sigma_{2b\text{-tag}}$. The trivial bound for the conservation of probability, given by $|V_{td}|^2+|V_{ts}|^2+|V_{tb}|^2 \leq 1$, is also included in the plots. As can be seen from the figure, the combination of the various constraints excludes a significantly larger region than each of the bounds separately. Note that a proper treatment requires taking into account the correlations between R and single top uncertainties. These are expected to be large, but without access to data we have no means to estimate them.

[†] β is probably close to 1/2, because if the invariant mass of the b-jet and the W boson is not close to the top quark the event is probably not selected.

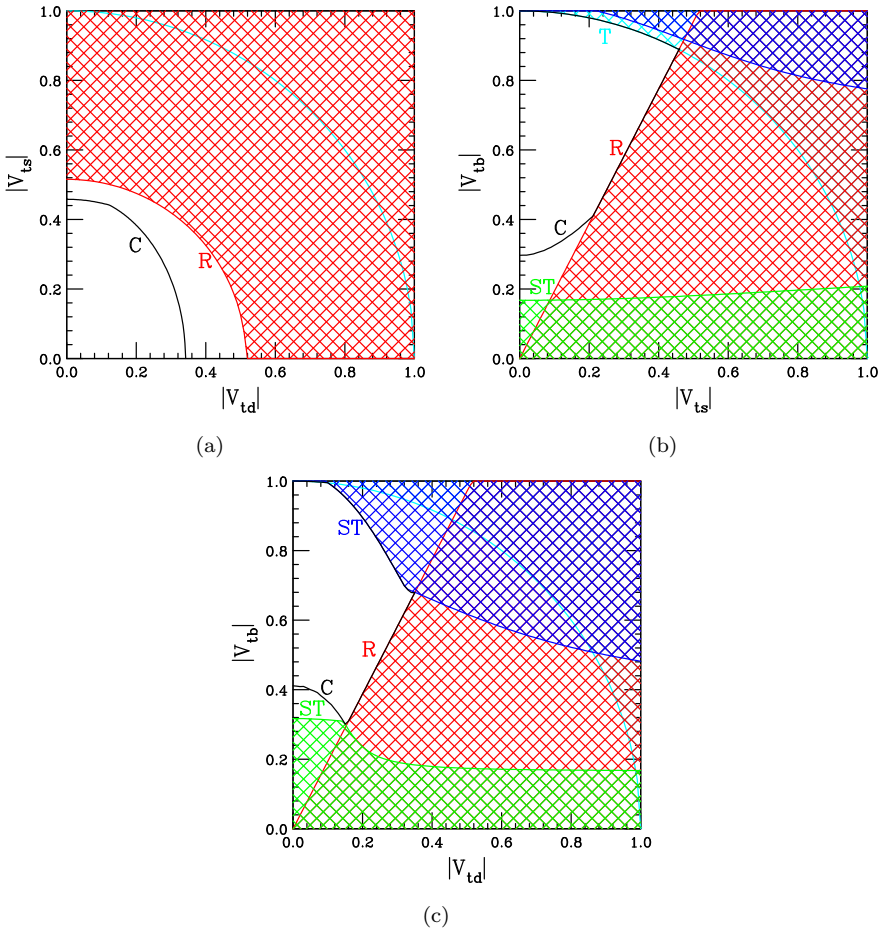

Figure 3.1: Projections of the excluded regions on the $|V_{td}|$ vs. $|V_{ts}|$ (a), $|V_{ts}|$ vs. $|V_{tb}|$ (b) and $|V_{td}|$ vs. $|V_{tb}|$ (c) planes. Constraints are only from CDF data (at 95% C.L.). The labels denote the reason for exclusion: "T" for the trivial constraint, "R" for the ratio R, Eq. (3.16) and "ST" for the single top production, eqs. (3.18, 3.19). "C" denotes the combined excluded region. Labels are written in the region that is still allowed by that constraint.

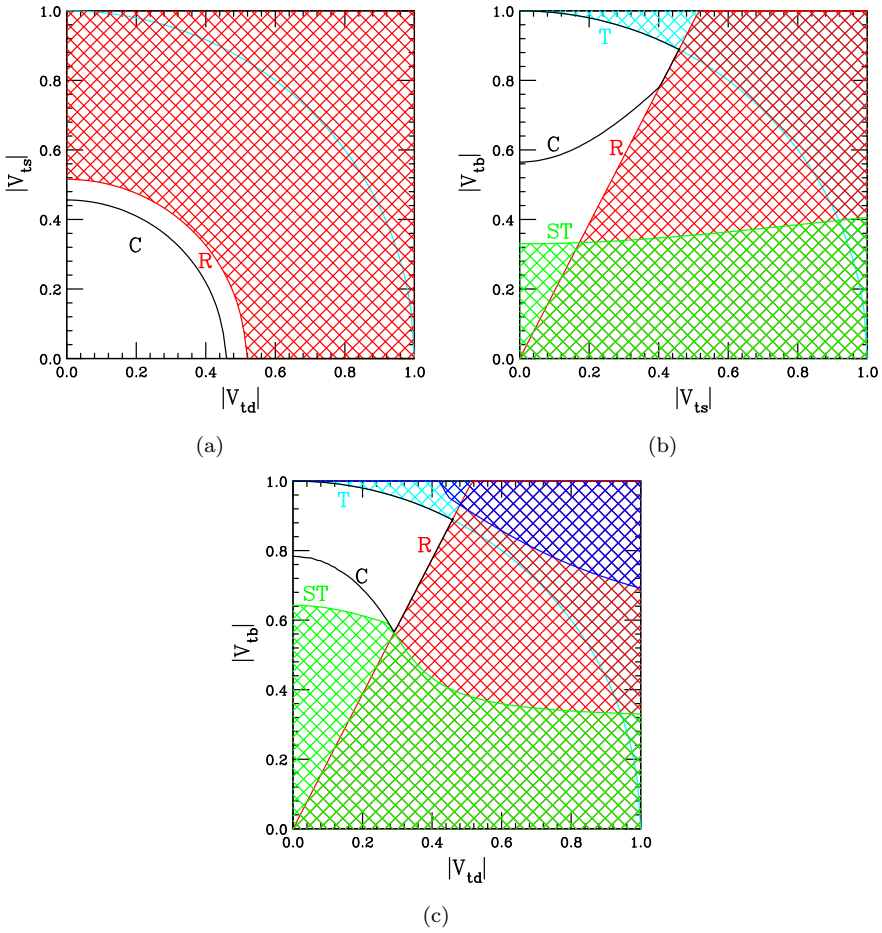

Figure 3.2: Projections of the excluded regions on the $|V_{td}|$ vs. $|V_{ts}|$ (a), $|V_{ts}|$ vs. $|V_{tb}|$ (b) and $|V_{td}|$ vs. $|V_{tb}|$ (c) planes. Constraints are only from DØdata (at 95% C.L.). The labels denote the reason for exclusion: "T" for the trivial constraint, "R" for the ratio R, Eq. (3.16) and "ST" for the single top production, eqs. (3.18, 3.19). "C" denotes the combined excluded region. Labels are written in the region that is still allowed by that constraint.

3.5 Discussion

For general studies, the strong indirect bounds on $|V_{tb}|$, as described in Sec. 3.2.1, can be misleading because New Physics can easily pollute constraints from loop–induced processes.

Using only direct measurements of the third row of the CKM elements it is clear from Figs. 3.1 and 3.2 that all the current direct bounds are consistent with the CKM matrix of the SM. There is, however, room for a non-unitary 3×3 CKM matrix and more elaborate studies are needed to precisely determine the bounds on the CKM matrix elements. There are multiple possible improvements for this study, both from the theoretical as well as the experimental sides. For example, one important issue is that we assumed that in the SM all t-channel events have one b-tagged jet, and all two b-tagged events are s channel. Towards the end of Chapter 4 we will see that this assumption is not entirely valid. Furthermore, important correlations between (systematic) experimental uncertainties are not taken into account. Only with the access to the experimental data and reliable Monte Carlos for their simulation, these can be accessed correctly.

CHAPTER

FOUR

T-CHANNEL SINGLE TOP AT NLO

As already outlined in the introduction, Sec. 1.2.2, there are three distinct electroweak production mechanisms to produce single top events at hadron colliders. Out of these three mechanisms the t channel has the largest rate, both at the Tevatron and the LHC [42–44]. Although the rate for single top production is relatively large compared to top quark pair production, it took almost 15 years since the discovery of of the top quark [4,5] to find a 5 standard deviation significance for electroweak single top production over the Standard Model background [7,8]. In fact, at the Tevatron the prospects for the detection and then measurement of the EW production cross sections have significantly worsened since the first theoretical proposals [147]. The main reason for this was an underestimate of the impact of large backgrounds such as those coming from $W+$ jet production (both with and without heavy flavors) and from the strong production of $t\bar{t}$ [148]. The situation at the LHC, though bound to improve thanks to the larger rates expected, will not be qualitatively very different.

The measurement of the single top production cross section plays a significant role in the physics program at the Tevatron, and will also be very important at the LHC. For example, the single top production channel is the only effective way of directly measuring V_{tb} [89].

The most accurate analyses for single top are based on two essential ingredients. The first is an in situ determination of the background rates. Predictions from theory are in this case not able to match the needed accuracy. The second is the

systematic exploitation of theoretical predictions for the kinematic properties of signal (and backgrounds). This information is encoded via sophisticated analysis techniques (such as those based on matrix elements, neural networks and others [7,8]). Such methods are crucial in building efficient discriminating variables to select the Standard Model signal or possibly find indications of new physics effects [149].

It is therefore clear that the most accurate predictions for the signal, both for rates and kinematic distributions, are needed as inputs in these analyses. An intense activity in the last fifteen years has led to increasingly-sophisticated predictions at NLO accuracy. Calculations have progressed from evaluations of total rates [52, 53], to differential distributions [30, 54], including spin correlations in production and decay [49, 55–57] and finally to the implementation of the three production channels in a fully exclusive Monte Carlo program [50,58].

t-channel single top production can be calculated in two different schemes. All NLO calculations available start from the $2 \to 2$ at the Born level, where a b quark appears in the initial state [150, 151]. This approach, *i.e.*, the five flavor scheme, has two main advantages. The first advantage is of a technical nature: starting from the $2 \to 2$ Born greatly simplifies the calculations, it leads to compact results, and a short running time when evaluating the Monte Carlo integration. The second advantage is that logarithms of the form $\log Q^2/m_b^2$ related to the initial state splitting $g \to b\bar{b}$ are resummed in the the b-quark parton distribution functions. For the $2 \to 2$ the typical scale Q is of the order of the top mass, m_t, which means that these logarithms can be large. The resummation of these logarithms into the b-quark parton density function improves the stability of the perturbative expansion.

However, within this approach the description of the extra b, or "spectator b", enters as the radiative contributions at the NLO level and are therefore effectively only described at leading order. For high-precision measurements at the Tevatron and the LHC this is not good enough and distributions related to the spectator b should also be described at NLO. As a result, most of the current calculations and corresponding Monte Carlo implementations [49, 50, 54–58] do not accurately model such effects. To improve this, it is needed to calculate the NLO corrections starting from the $2 \to 3$ at the Born level. In this approach, called the four flavor (decoupling) scheme, the b quarks are considered to be massive quarks and do not enter the evolution of the parton density functions and the running of the strong coupling. Unfortunately, the calculation of the NLO corrections is much more involved due to the presence of an additional (massive) particle in the final state. For the loop corrections this leads to three extra scales compared to the loop corrections to the $2 \to 2$ process, which gives

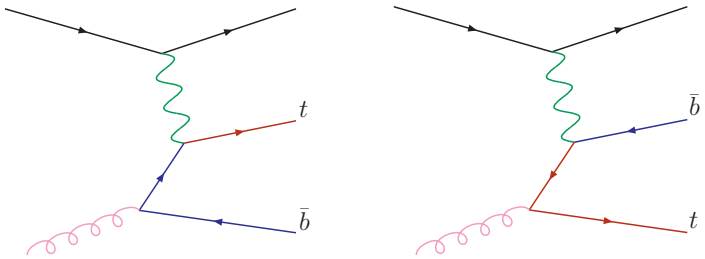

(a) (b)

Figure 4.1: Representative LO t-channel single top diagrams. The other two diagrams for the other subprocess can be obtained by reversing the light quark line.

lengthly expressions and a longer running time for the Monte Carlo integration. However, in this approach the description of the spectator b quark is genuinely at NLO accuracy, which is what is required for high precision phenomenological applications.

By definition the two approaches are equivalent if all orders in the perturbative expansion would be included. However, at low order the two predictions could differ substantially and the question of the ranges of applicability of the two approaches arises.

In the rest of this chapter we describe the calculation of the NLO corrections to the t-channel single top production in the four flavor scheme. Furthermore we will show the results and try to shed some light on the ranges of applicability of the two approaches.

4.1 Born contributions

At the Born level there are two subprocess with each two diagrams contributing, see Fig. 4.1. The other subprocess has the light fermion line in the other direction. Without loss of generality we will ignore these other contributions in the discussion for the moment. The diagrams for t-channel single anti-top production can be obtained by changing the top and the bottom masses in the calculation.

The leading order cross section can be calculated from these diagrams by squaring and convoluting them with the parton density functions for the initial state gluon and quark, performing the phase space integral and including the overall flux factor.

It is important to stress that the LO t-channel single top diagrams do not interfere with (the real emissions of the NLO corrections to) s-channel single top production. Although both contributions possibly have the same initial and final state particles, $gq \to q't\bar{b}$ the interference contributions always contain a closed quark loop with a single gluon (and two W bosons) attached. Because the eight color matrices T^a are traceless, $\mathrm{Tr}[T^a] = 0$, the color structure of a closed quark loop with a single gluon attached vanishes. Hence, there is no interference between s- and t-channel diagrams and they are fully separated at this order in perturbation theory.

4.2 NLO corrections

The NLO QCD corrections to a given process with a n-parton final state receive two types of contributions: the one-loop virtual correction to the $(2 \to n)$-parton scattering process, and the real emission correction from all possible $(2 \to n+1)$-parton scattering processes. For the numerical evaluation, one has to be able to compute both types of contributions separately.

Any NLO calculation for a prediction at a hadron collider consist of the following three ingredients.

- Real corrections. These are tree-level corrections that have one extra QCD parton in the final state.
- Virtual corrections. These are the loop corrections to the Born diagrams and should have the same initial and final state particles as the corresponding Born diagrams.
- Subtraction terms. These cancel infrared divergences in the real and virtual corrections separately.

Each of these contributions need their own treatment which we will discuss in the following sections.

4.3 Real corrections

The real contributions are characterized by the one extra real QCD parton in the final state compared to the Born contributions. Even in the case of a diagonal CKM matrix, this leads to a total of 41 subprocesses. Fortunately,

most of these subprocesses differ only by the flavor of a quark line and can therefore be combined, leading to a total of 16 distinct subprocesses which should be computed, see Table 4.1. A similar set can be constructed for anti-top quark production.

As can be seen from the table, the number of diagrams that needs to be computed is very modest *i.e.*, there is no need to use recursive relations to calculate these contributions: the conventional Feynman diagram approach suffices. The analytical calculations have been performed with FORM [152]. The possible (bookkeeping) difficulties arise only from the large number of subprocesses that each have a slightly different set of diagrams contributing with different interference terms, etc. Care has to be taken to include the correct interference terms for each of the contributions, which is even more prominent when off-diagonal CKM matrix elements are included.

Our implementation takes all contributions and interferences between the t-channel diagrams into account as well as effects from off-diagonal CKM matrix elements.

4.3.1 Interference between t- and s-channel diagrams

At the Born level there is a clear separation between t- and s-channel diagrams. This is even true for the slightly more elaborate set of diagrams contributing to the real NLO corrections to the $2 \to 2$ process. Both t- and s-channel contribu-

Subprocess	# of t-channel diagrams	Subprocess	# of t-channel diagrams
$u\bar{u} \to t\bar{b}\bar{u}d$	2	$ud \to t\bar{b}dd$	4
$\bar{u}\bar{d} \to t\bar{b}\bar{u}\bar{u}$	4	$us \to t\bar{b}ds$	2
$\bar{u}\bar{s} \to t\bar{b}\bar{u}\bar{c}$	2	$\bar{c}\bar{d} \to t\bar{b}\bar{u}\bar{c}$	2
$uu \to t\bar{b}ud$	4	$c\bar{d} \to t\bar{b}\bar{u}c$	2
$uc \to t\bar{b}us$	2	$d\bar{d} \to t\bar{b}\bar{u}\bar{d}$	4
$uc \to t\bar{b}cd$	2	$gu \to t\bar{b}dg$	12
$u\bar{d} \to t\bar{b}\bar{u}u$	2	$g\bar{d} \to t\bar{b}\bar{u}g$	12
$u\bar{d} \to t\bar{b}\bar{d}d$	2	$gg \to t\bar{b}\bar{u}d$	8

Table 4.1: Set of (distinctive) subprocesses contributing to the real NLO contributions of t-channel single top production in the four flavor decoupling scheme. Each of these subprocesses have a slightly different set of diagrams and/or interference terms contributing.

tions form a gauge invariant subset of diagrams and the interference between the two processes is exactly zero. Quite remarkably the interference between t- and s-channel diagrams is still almost factorized for the real corrections for the $2 \to 3$ Born process. Although all the subprocesses listed in Table 4.1 also have s-channel contributions in them, the interference between the t- and s-channel diagrams are color suppressed by at least $1/N_c$. We have checked that the interference is indeed very small by generating the corresponding subprocesses with `MadGraph`. We find that (with some hard cuts on the final state particles) the interference is smaller than the integration error obtained by `MadGraph`, *i.e.*, $< 0.4\%$. We have neglected the interferences between these real NLO t-channel and real NNLO s-channel corrections.

4.3.2 Interference with W associated single top production

In the $q\bar{q} \to t\bar{b}q'\bar{q}$ subprocesses there is interference between with W boson associated single top production, $q\bar{q} \to t\bar{b}(W^- \to q'\bar{q})$. This includes interferences with $t\bar{t}$ production. Although the cross section of $t\bar{b}W^-$ production is very large and the interference with t-channel single top are only $1/N_c$ suppressed, the interference is small due to completely different kinematics of the two processes: while for t-channel single top production the W boson in space-like, for $t\bar{b}W$ production the W boson will be on-shell. Therefore the interference terms will be suppressed by Γ_W/M_W. Moreover, in the narrow width approximation for the W-boson, $\Gamma_W \to 0$, the interference terms are exactly zero. We have not included these interference terms in our calculation.

4.3.3 Interference between heavy and light quark lines

There is one more class of interference terms that need to be addressed: the interference between the heavy and light quark lines. For the $2 \to 2$ process there are no interference effects between the light and heavy quark lines. Also the NLO corrections factorize between the two lines, due to the color algebra. This allows one to choose different renormalization and factorization scales for the light and heavy quark lines. Unfortunately, this separation of the NLO corrections is no longer exact for the real contributions to the $2 \to 3$ Born.

Contributions coming from interference terms between the light and heavy quark lines are included, but need a non-physical splitting to assign them to the light or heavy quark line to be able to assign a different renormalization and factorization to each of the lines. We have decided to simply split the

interference by two and add equal weigths to the light and the heavy quark line. This should be a very good approximation, because the interference terms are $1/N_c^2$ suppressed, and the scale dependence is mild for these terms. Moreover for most phenomenological applications the difference between the two scales should be reasonably mild.

4.4 Virtual corrections

The virtual corrections consist of all the diagrams of one higher order in the strong coupling (compared to the Born contribution) that have the same initial and final state particles as the Born contribution. This leads to a set of diagrams with exactly one closed loop. The momenta flowing through the loop is undetermined and should be integrated over. These diagrams contribute when interfered with the Born level diagrams, such that the corrections to the amplitude squared are of order α_s^2, *i.e.*, one order higher then the LO contributions.

Although this is a $2 \to 3$ process, we do not have to calculated any pentagons, *i.e.*, loops consisting of five particle lines. The color algebra restricts the loop corrections to this process to the heavy or the light quark lines only. This can easily be seen by considering the following argument. Because of color algebra there are no loop diagrams in which the W boson is part of the loop: a gluon connection between the light and the heavy quark line will always lead to a T^a_{ii} color structure for the light quark line (where a is the color index for the gluon) which gives zero, because the T^a_{ij} are anti-symmetric in i and j. Therefore we can treat the corrections to the light quark line separate from the heavy quark line and vice versa.

The corrections to the light quark line are exactly the same as for the $2 \to 2$ process and will not be described here.

There are 11 loop diagrams contributing to the corrections to the heavy quark line: 3 boxes, 6 triangles and 2 bubbles. They are depicted in Fig. 4.2. The calculations for the contributions from these diagrams have been performed with FORM [152].

The diagrams can be divided into two groups according to their color structure and those sets can be treated completely independent. The division can be made according to leading versus sub-leading color structures given in the table:

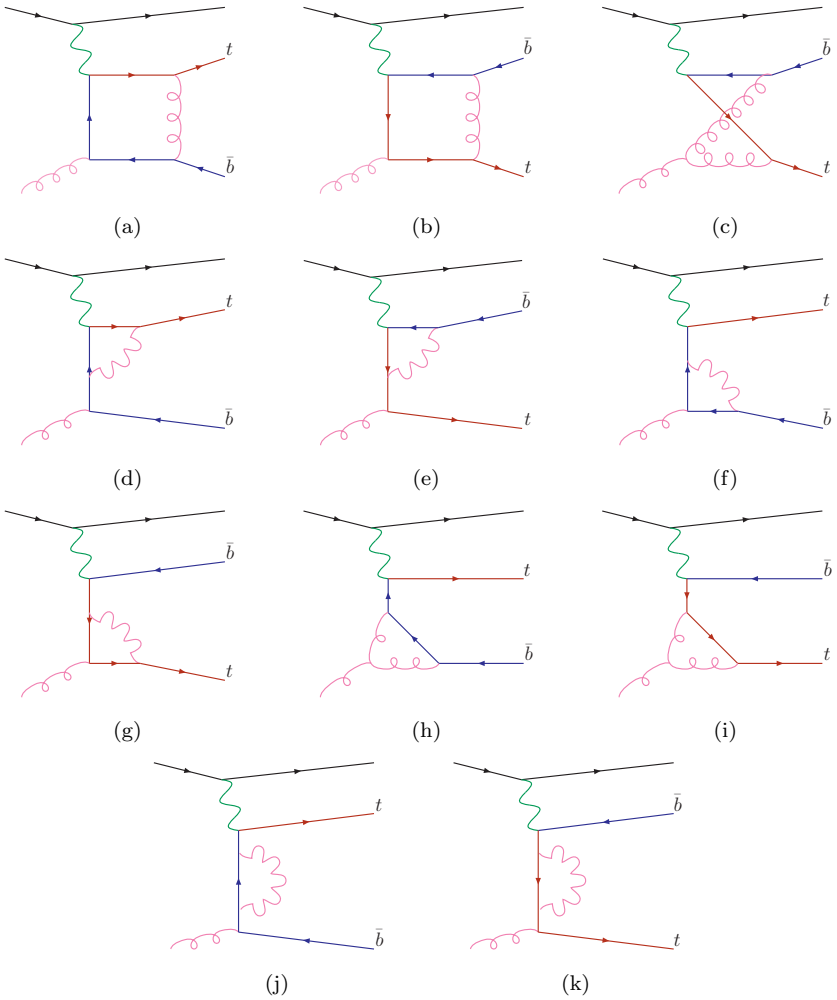

Figure 4.2: Loop diagrams contributing to corrections to the heavy quark line.

Diagram	$\frac{N_c}{2} t^a_{ij}$	$\frac{-1}{2N_c} t^a_{ij}$
(a)		1
(b)		1
(c)	1	
(d)	1	1
(e)	1	1
(f)		1
(g)		1
(h)	1	
(i)	1	
(j)	1	1
(k)	1	1

The index a is the color factor for the gluon, i for the top quark and j for the anti-top quark. Once these diagrams are interfered with the Born contributions, which have a color factor T^a_{ij}, the color factor for the left and right columns are given by $\frac{N_c}{4}(N_c^2-1)$ and $\frac{-1}{4N_c}(N_c^2-1)$, respectively.

4.4.1 Dimensional reduction

To perform the regularization of the divergences we use dimensional reduction. In the dimensional reduction scheme all the Feynman rules and the Dirac Algebra is performed in the original 4 dimensions. Only the loop momentum is considered to be $\hat{d}=4-2\epsilon$ dimensional and the gluon polarization are quasi 4 dimensional, both for internal and external gluons.

So, in this scheme we have to distinguish three different spaces [153]:

- The original $\bar{d}=4$ dimensional space (4S) with metric tensor $\bar{g}_{\mu\nu}$ and $\bar{g}_{\mu\nu}\bar{g}^{\mu\nu}=4$. All momenta, except for the loop momenta, are objects in this space. Also the Dirac Algebra has to be performed in this space.
- A formally $\hat{d}=4-2\epsilon$ dimensional space (DS) with metric tensor $\hat{g}_{\mu\nu}$ and $\hat{g}_{\mu\nu}\hat{g}^{\mu\nu}=4-2\epsilon$. This space is formally a super-space of the $\bar{d}=4$ dimensional space 4S, $\hat{g}^{\mu\nu}\bar{g}_\nu{}^\rho=\bar{g}^{\mu\rho}$. The loop momenta belong to this space.
- A formally (quasi) $d=4$ dimensional space (Q4S) with metric tensor $g_{\mu\nu}$ and $g_{\mu\nu}g^{\mu\nu}=4$. This space is a super-space of the $\hat{d}=4-2\epsilon$ dimensional space DS and the $\bar{d}=4$ dimensional space 4S, $g^{\mu\nu}\hat{g}_\nu{}^\rho=\hat{g}^{\mu\rho}$ and $g^{\mu\nu}\bar{g}_\nu{}^\rho=\bar{g}^{\mu\rho}$. The gluon polarizations belong to this space.

Because the original DS space is a subspace of the Q4S space it can be stated that *"$\hat{d}$ is effectively smaller than 4"* for the dimensional reduction scheme [54].

These three spaces effectively lead to the relation between two adjacent Dirac matrices, when both of them are contracted with a $\hat{d}=4-2\epsilon$ dimensional loop momentum,

$$\not{l}\not{l}=l^\mu l^\nu\gamma_\mu\gamma_\nu=\tfrac{1}{2}l^\mu l^\nu\{\gamma_\mu,\gamma_\nu\}=l^\mu l^\nu\hat{g}_{\mu\nu}=l^2. \tag{4.1}$$

4.4.2 Renormalization of UV divergences

To cancel the UV divergences we need wave function, coupling constant and mass renormalizations. The wave function and coupling constant renormaliza-

tion factor from the tree-level corrections, and are given be an overall factor times the Born contribution.

The wave function renormalization in the dimensional reduction scheme gives for external heavy quark q a factor

$$-\frac{\alpha_s}{2\pi}C_F\Big(\frac{3}{2\epsilon}+\frac{5}{2}+3\log\frac{\mu_R}{m_q}\Big)\mathcal{M}_{\text{Born}}, \tag{4.2}$$

and for each gluon

$$-\frac{\alpha_s}{2\pi}T_F\Big(\frac{2}{3\epsilon}+\frac{4}{3}\log\frac{\mu_R}{m_q}\Big)\mathcal{M}_{\text{Born}}. \tag{4.3}$$

To normalize the charge we need to include for each α_s (this is for the $\overline{\text{MS}}$ scheme)

$$+\frac{\alpha_s}{2\pi}\left[\Big(\frac{2}{3\epsilon}T_F n_{\text{lf}}-\frac{11}{6\epsilon}C_A\Big)+\frac{2}{3\epsilon}T_F+\frac{4}{3}T_F\log\frac{\mu_R}{m_q}\right]\mathcal{M}_{\text{Born}}, \tag{4.4}$$

where $n_{\text{lf}}=4$, that is the number of light quark flavors. In addition, to have the result in the dimensional reduction scheme a finite renormalization of the strong coupling is needed

$$\alpha_s^{\text{D.red.}}=\alpha_s^{\overline{\text{MS}}}\Big(1+\frac{C_A}{6}\frac{\alpha_s^{\overline{\text{MS}}}}{2\pi}\Big), \tag{4.5}$$

which, in our case, results in adding the term

$$\frac{C_A}{6}\frac{\alpha_s}{2\pi}\mathcal{M}_{\text{Born}} \tag{4.6}$$

to the amplitude.

In total this gives for our case with one top quark, one bottom quark and one gluon as external particles as well as one α_s needing renormalization

$$\begin{aligned}+\frac{\alpha_s}{2\pi}\left[\Big(\frac{2}{3\epsilon}T_F n_{\text{lf}}-\frac{11}{6\epsilon}C_A\Big)-C_F\Big(\frac{3}{2\epsilon}+\frac{5}{2}+3\log\frac{\mu_R}{m_b}\Big)\right.\\ \left.-C_F\Big(\frac{3}{2\epsilon}+\frac{5}{2}+3\log\frac{\mu_R}{m_t}\Big)+\frac{C_A}{6}\right]\mathcal{M}_{\text{Born}}.\end{aligned} \tag{4.7}$$

Furthermore there are two mass renormalization diagrams, pictured in Fig. 4.3. These corrections do not factor over the Born and need to be computed as separate diagrams with a mass insertion at the black dot. The mass insertion μ_q is given by

$$\mu_q=g_s^2C_F\Big(\frac{3}{\epsilon}+5+3\log[\mu^2/m_q^2]\Big)m_q, \tag{4.8}$$

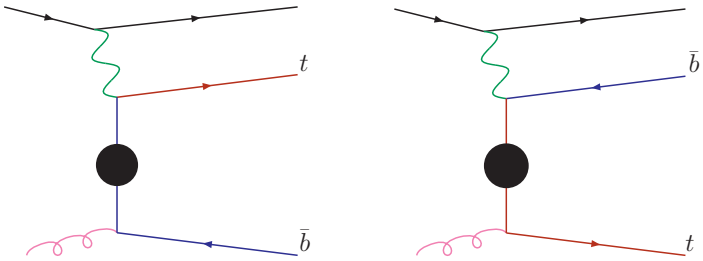

(a) (b)

Figure 4.3: Diagrams for the UV renormalization of the heavy quark masses. The black dot represents the mass insertion.

with μ the renormalization scale.

Inclusion of the wave function and charge renormalizations, Eq. (4.7), and mass renormalization, Eq. (4.8), removes the UV divergences from the loop diagrams.

4.4.3 Finite renormalization from γ_5 in the coupling

In general, the γ_5 is not well-defined in any number of dimensions not equal to 4. Therefore, if there is a string of Dirac matrices with both γ_5's and $\hat{d} = 4-2\epsilon$ dimensional indices (due to contractions with loop momenta) care has to be taken. In particular when there are UV divergences present, the dimensional reduction scheme is ill–defined and ambiguous. Therefore we have chosen to compute the triangles in the four–dimensional helicity scheme and converting this result to dimensional reduction. The difference between the two schemes is subtle, but in practice it can be said that, *"$\hat{d}$ is effectively larger than 4"* for the four–dimensional helicity scheme [54]. This has the following consequence for two adjacent Dirac matrices contracted with loop momenta,

$$\not{l}\not{l} = l^\mu l^\nu \gamma_\mu \gamma_\nu = \tfrac{1}{2} l^\mu l^\nu \{\gamma_\mu, \gamma_\nu\} = l^\mu l^\nu \bar{g}_{\mu\nu} = l^\mu l^\nu \hat{g}_{\mu\nu} - l^\mu l^\nu \dot{g}_{\mu\nu} = l^2 - l^\mu l^\nu \dot{g}_{\mu\nu}, \tag{4.9}$$

where $\dot{g}_{\mu\nu}$ is the -2ϵ dimensional metric. This relation should be compared with Eq. (4.1).

Furthermore, to convert our result to the dimensional reduction scheme and fix the Ward identities a finite renormalization for UV divergent diagrams with a γ_5 in the loop is needed. In our calculation this is only the case for the six triangles:

- for the triangles (d) and (e) (*i.e.*, vertex corrections to the W boson vertex) there is an (explicit) γ_5 in the loop.
- the other triangles ((f), (g), (h) and (i)) (*i.e.*, gluon vertex corrections) only if the polarizations for the external gluon are inserted before the Passarino–Veltman reduction is done, there is an (implicit) γ_5 in the loop.

Triangles (d) and (e)

The first source is a well-known problem and various (similar) calculations already exist in the literature to which our calculation has been checked. In particular, the corrections when a W-boson couples to two massless quarks (which also appears in the corrections to the light quark line) and to one massive and one massless quark [54] agree with the above procedure. There is no reason to believe that our procedure breaks down when the W couples to two massive quarks. If we use the naively anti-commuting γ_5 in the four–dimensional helicity scheme, the following finite renormalizations are needed to convert it to the dimensional reduction scheme

$$\text{(d)}: \quad -C_F\frac{\alpha_s}{2\pi}\times\mathcal{M}^{(\text{a})}_{\text{Born}} \tag{4.10}$$

$$\text{(e)}: \quad -C_F\frac{\alpha_s}{2\pi}\times\mathcal{M}^{(\text{b})}_{\text{Born}} \tag{4.11}$$

where $\mathcal{M}^{(\text{a})}_{\text{Born}}$ and $\mathcal{M}^{(\text{b})}_{\text{Born}}$ are the amplitudes corresponding to the Born diagrams represented in Fig. 4.1 (a) and 4.1 (b), respectively.

Triangles (f), (g), (h) and (i), method 1

For the second source we have a very powerful check to make sure that our calculation is consistent. We can easily perform the calculation of these four triangle graphs in two different ways. The first method is by using the four–dimensional helicity scheme and including the polarization vector for the gluon from the start of the calculation, as we did for diagrams (d) and (e), and the second method is by using the original dimensional reduction and first simplifying our result and performing the Passarino–Veltman reduction before introducing the gluon polarization vectors.

For the first method, we include the gluon polarizations from the start and therefore we have a γ_5 in the traces. This situation is very similar to the triangles (d) and (e) described above, hence we need a finite renormalization to

convert to the dimensional reduction scheme and fix the Ward identities. We can distinguish between corrections to the top quark line and corrections to the bottom quark line. Furthermore we have diagrams with a three gluon vertex and without a three gluon vertex, which belong to different color structures. It turns out that the following finite renormalizations are needed*

$$\text{(f)}: \quad \frac{1}{2N_c}\frac{\alpha_s}{2\pi} \times \mathcal{M}^{(\text{a})}_{\text{Born}} \tag{4.12}$$

$$\text{(g)}: \quad \frac{1}{2N_c}\frac{\alpha_s}{2\pi} \times \mathcal{M}^{(\text{b})}_{\text{Born}} \tag{4.13}$$

$$\text{(h)}: \quad -\frac{N_c}{2}\frac{\alpha_s}{2\pi} \times \mathcal{M}^{(\text{a})}_{\text{Born}} \tag{4.14}$$

$$\text{(i)}: \quad -\frac{N_c}{2}\frac{\alpha_s}{2\pi} \times \mathcal{M}^{(\text{b})}_{\text{Born}}, \tag{4.15}$$

The sum of these four finite renormalization is equal to

$$-C_F\frac{\alpha_s}{2\pi} \times \mathcal{M}_{\text{Born}}. \tag{4.16}$$

Triangles (f), (g), (h) and (i), method 2

The second method we have used to calculate these four triangles is to first simplify a string of Dirac matrices, before including the gluon polarizations and quark helicities. This has the advantage that for the simplification of the gamma matrices there are no γ_5's. Therefore we can safely use the original dimensional reduction and keep the dimensions of the loop momenta in $\hat{d} = 4 - 2\epsilon$ dimensions.

Once the string of γ matrices has been simplified by using the anti-commutation relations of the Dirac matrices and the relation in Eq. (4.1), there is maximally one $\not{l}$ left per string. We can now use Passarino–Veltman reduction to reduce the loop integrals with one l_μ in the numerator, which will leave us with strings of Dirac matrices with *only* 4 dimensional objects and indices. Hence, there are no more problems when including the gluon polarizations and quark helicities (*i.e.* γ_5) in these strings and converting them to traces. Therefore, there is also no need for any finite renormalization and we have checked that the results are the same as the results obtained by using the four–dimensional helicity scheme described above.

*This is using 'normal' Feynman rules. When using Background Gauge Field Feynman rules the finite renormalizations to the diagrams with the three-gluon vertex ((h) and (i)) should be twice as large.

Bubbles and boxes

Let us remind the reader that there are no problems with the bubble diagrams ((j) and (k)), because there are no γ_5's present in the loop. The boxes ((a), (b) and (c)) are UV-finite, which means that also they do not suffer from the spurious anomalies related to the γ_5. We have checked this by removing the axial part of the coupling of the W boson and using the two methods described above for dealing with the gluon polarization. Both methods gave the same result in the dimensional reduction and the four–dimensional helicity schemes, without the need of a finite renormalization.

4.4.4 Scalar integrals

The tensor integrals in the virtual corrections have been decomposed with the help of the reduction routine based on the Passarino-Veltman approach [154]. The full reduction leads to double inverse Gram determinants, which could lead spurious poles and therefore to numerically unstable results. By extending the set of master integrals to include, for instance, also the C_{001} and C_{002} functions, the double inverse Gram determinants can be avoided by absorbing them into these well-behaved functions.

The master integrals have been explicitly computed with standard methods and compared numerically with those available in the `QCDloop` package, Ref. [155].

4.4.5 Top quark decay

Top quarks decay before they can hadronize. In a detector top quarks will never be detected directly but can only be reconstructed from their decay products. For correct phenomenological studies it is therefore necessary to include the decay the top quarks, keeping track of their spin correlations.

As we have been using helicity amplitudes for the calculation of the virtual corrections, it is straight forward to include the decay of the top quark following, *e.g.*, the work presented in Ref. [156]. However, we have not included the top quark decay in the following as we are mostly interested in total cross section and/or comparison with the calculation in the 5 flavor scheme. We leave the study of the decay products of the top quarks for future work.

4.5 Subtraction terms

The real emission corrections contain soft and collinear singularities, which become explicit only after integration over the appropriate real radiation phase space yielding a hard n-parton final state. They are canceled by the IR singularities from the virtual one-loop contributions, thus yielding a finite NLO correction. To systematically extract the real radiation singularities from arbitrary processes, a variety of methods, based either on phase-space slicing [157] or on the introduction of process-independent subtraction terms [158] have been proposed. Several different algorithms to derive subtraction terms are available: residue subtraction [159], dipole subtraction [160, 161] and antenna subtraction [162–165].

We have chosen to use the the dipole subtraction formalism, which provides local subtraction terms for all possible initial and final state configurations [160] and allows to account for radiation off massive partons [161].

4.5.1 Dipole subtraction

The fundamental building blocks of the subtraction terms in the dipole formalism [160, 161] are dipole splitting functions $\mathbf{V}_{ij,k}$, which involve only three partons: emitter i, unresolved parton j, spectator k. A dipole splitting function accounts for the collinear limit of j with i, and for part of the soft limit of j in between i and k. The dipole factors, which constitute the subtraction terms, are obtained by multiplication with reduced matrix elements, where partons i, j and k are replaced by recombined pseudo-partons $\widetilde{ij}$, $\widetilde{k}$. The full soft behavior is recovered after summing all dipole factors.

Because the sum over all dipole factors leads to the same soft and collinear behaviors as the real $n+1$ matrix elements, subtracting the sum over dipoles from the real matrix elements regulates the integral over the phase space for the real contributions to a finite number. However, the integral has a left-over integrable singularity, *i.e.*, the integral is not bounded, which means that the generated events cannot by unweighted.

Although the singularities are cancelled locally, slightly away from the pole the cancellation is not exactly point by point. Due to the mapping of the momentum from the $n+1$ to the n body phase space there might be "misbinnings" between a dipole and the real matrix element, *i.e.*, in a kinematic distribution the contribution from the dipole and the matrix element do not end up in the same bin. Because the (absolute) contributions close to the

singularity are large, but opposite in sign, for the matrix elements and the dipole, the statistical fluctuations in histograms is a greater problem than for leading order calculations. The effects of mis-binnings is a serious problem in NLO calculations, which can be minimized choosing smart mappings for the momenta between the real and the subtraction contributions or simply by increasing the bin-size or the number of Monte Carlo integration points.

Of course, the total contributions from the subtraction terms should be zero. Therefore the same dipoles integrated over the 1-body phase-space are added to the virtual contributions, yielding a vanishing total contribution from the subtraction terms.

4.6 Checks of the calculation

We have checked that all the (tree-level) real subprocesses listed in Table 4.1 agree point-by-point in phase space with the matrix elements generated automatically by the `standalone` version of `MadGraph/MadEvent` [95].

The list of dipole subtraction terms for the reals have been independently generated by `MadDipole` [166], see the appendix A for a description of the code. We have checked that the subtraction terms agree point-by-point in phase-space and found no differences.

For the virtual corrections we have checked gauge invariance for both the external gluon and the W boson vertex. The sum of the loop diagrams should be zero when the external gluon (or W boson) is contracted with its momentum. We have performed this check analytically and verified that the sums indeed give zero.

Finally, and as the most important check we have calculated $e^+e^- \to Z_{V-A} \to b\bar{b}g$ by crossing our calculation to have the W-boson in the s-channel, setting $m_t = m_b$ and removing the QCD corrections to the light quark line. We have checked numerically that we get the same jet rates as presented in Ref. [167], apart from the overall normalization. The difference in normalization can be explained and accounted for by considering the differences in charges of the particles coupling to the (left-handed) Z_{V-A} vector boson.

4.7 Comparison $2 \to 2$ with $2 \to 3$

4.7.1 PDF sets

We have done our calculation in the 4 flavor scheme, in which there are 4 light quarks and the massive quarks are subtracted at zero momentum. To be consistent also a genuine 4-flavor PDF set should be used to extract the parton luminosities to be used in our calculation. However, the most recent set is from the MRST family, `MRST2004FF4` [168], is from 2004 and does not have all the latest updates as in the recent `MSTW2008` [169] or `CTEQ6.6` [170]. In particular the treatment of the massive quarks has been improved considerately, which, as we have checked, has a substantial impact on the prediction of t-channel single top in the $2 \to 2$ approximation.

From 4 to 5 flavors

The other solution would be to use any of the recent 5-flavor PDF sets and compensate for the difference when connecting the 4 flavor scheme matrix elements to the 5 flavor scheme PDF's. This can be done, following Ref. [171], by adding a term

$$-\alpha_s \frac{T_F}{3\pi} \log \frac{m_b^2}{\mu_F^2} \mathcal{M}_{\text{Born}} \tag{4.17}$$

for each initial state gluon and a term

$$-\alpha_s \frac{T_F}{3\pi} \log \frac{\mu_R^2}{m_b^2} \mathcal{M}_{\text{Born}} \tag{4.18}$$

for each α_s to go from 4 flavor running of α_s to 5 flavor running, as explained by M. Cacciari, M. Greco and P. Nason. In our case, which is order $\mathcal{O}(\alpha_s)$ and with one initial state gluon (at the Born level), this results in adding the term

$$-\alpha_s \frac{T_F}{3\pi} \log \frac{\mu_R^2}{\mu_F^2} \mathcal{M}_{\text{Born}} \tag{4.19}$$

to the amplitude. In our case the above term is numerically small and exactly zero for choices of the factorization equal to the renormalization scale: the decrease of the gluon PDF is compensated for by the 5 flavor running of α_s.

We have compared our calculation using the `MRST2004FF4nlo` against the `MRST2004nlo` plus the corrections described above and found excellent agreement between the two approaches. Therefore, we have decided to use the recent `CTEQ6.6` PDF set and compensate for the slightly lower gluon luminosity and the 5 flavor running of the strong coupling.

4.7.2 Total cross section and scale dependence

We now present and discuss the total cross section of the NLO calculation in the 4F scheme (Born $2 \to 3$) and compare with those of the 5F scheme (Born $2 \to 2$), at the Tevatron ($p\bar{p}$, $\sqrt{s} = 1.96$ TeV) and the LHC (pp, $\sqrt{s} = 14$ TeV). In our studies we assume $m_t = 172$ GeV, $m_b = 4.5$ GeV and use the `CTEQ6.6` PDF set [170], unless stated otherwise. For the $2 \to 3$ calculation we pass to the 4F scheme by adding suitable finite terms, as explained in Sec. 4.7.1. As an independent check we have verified that results obtained with the explicit four-flavor MRST set [168] are fully consistent with those obtained in the corresponding five-flavor MRST set plus the finite terms.

In Fig. 4.4 we show the cross sections for top production at the Tevatron and the LHC in the two schemes as a function of μ/m_t, where μ is a common renormalization and factorization scale. The 4F calculation has a stronger dependence on the scale than the 5F one, particularly at the Tevatron, which simply reflects the fact that the $2 \to 3$ Born calculation already contains a factor of α_s. However, we observe that both calculations are much more stable under scale variations at NLO than at LO.

As outlined in the Secs. 4.3 and 4.4 the NLO corrections can be assigned to the light and heavy quark lines. This allows us to vary the scale dependence associated to the heavy and light lines separately to establish an optimal central value for the scales.

In the 4F scheme, most of the overall scale dependence is inherited from the heavy quark line due to the fact that this line contains a factor of α_s at leading order. The scale for this coupling is governed by the initial state gluon splitting to $b\bar{b}$ and therefore should be of the order of the maximum p_T of the spectator b. Numerically this is of the order of $m_t/4$. This is also the scale for which the dependence on the scales is the mildest and close to where the LO and NLO approximations cross, which confirms this value to be appropriate. The scale dependence of the light line is mild and prefers slightly larger scales. We have chosen the central value of $m_t/2$.

In the 5F scheme the scale dependence is very mild and we simply choose m_t for both lines.

Uncertainty from higher orders

The uncertainty from uncalculated higher orders in the perturbative expansion is estimated by varying the factorisation and the renormalisation scales μ_F and

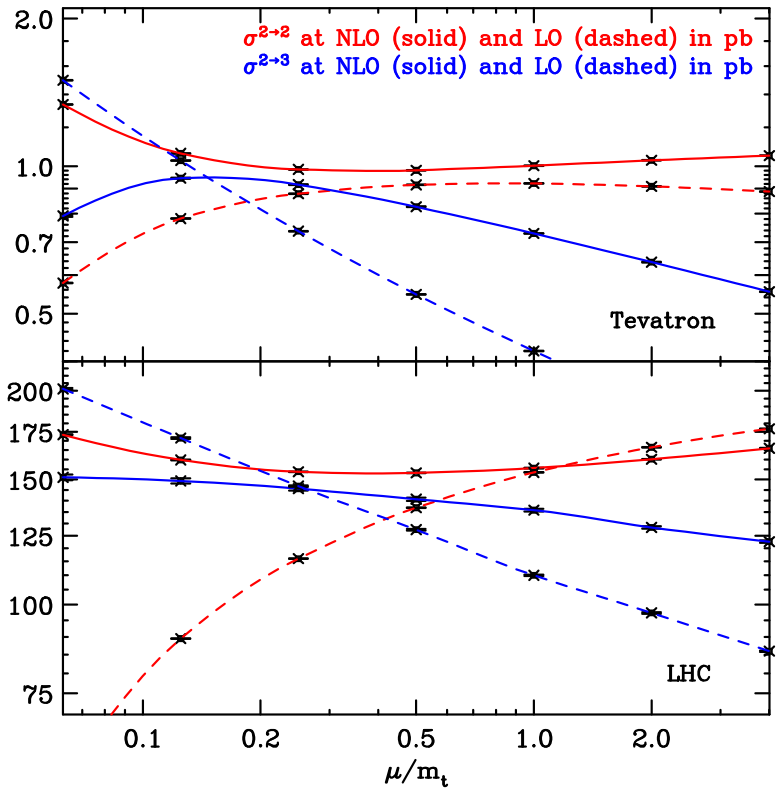

Figure 4.4: Scale dependence of the $2 \to 2$ and $2 \to 3$ calculations, at LO (dashed) and NLO (solid) order at the Tevatron (*upper plots*) and LHC (*lower plots*). Factorization and renormalization scales in the heavy and light quark lines are equal to μ. Plots show only top quark production, anti-top production being the same for the Tevatron at has a very similar behaviour for the LHC.

μ_R independently around the central scale choice, μ_0. As discussed above, in the $2 \to 3$ calculation we have $\mu_0 = \mu^L$ for the light line and $\mu_0 = \mu^H$ for the heavy line, whereas the $2 \to 2$ calculation uses $\mu_0 = m_t/2$.

The values of μ_F and μ_R that we range over are specified by,

$$(\mu_F, \mu_R) \in \Big\{ (2\mu_0, 2\mu_0),\ (2\mu_0, \mu_0),\ (\mu_0, 2\mu_0),\ (\mu_0, \mu_0),\ (\mu_0, \mu_0/2),\ (\mu_0/2, \mu_0),\ (\mu_0/2, \mu_0/2) \Big\} . \quad (4.20)$$

In this way we ensure that none of the ratios, μ_F/μ_0, μ_R/μ_0 and μ_F/μ_R, is outside the interval $[\frac{1}{2}, 2]$. These ratios naturally appear as arguments of logarithms at NLO, so restricting them in this way is motivated by the requirement of good perturbative behaviour.

The uncertainties are then defined with respect to this set of variations as,

$$\Delta\sigma_{\mu+} = \max_{\{\mu_F,\mu_R\}} \Big[\sigma(\mu_F,\mu_R) - \sigma_{\text{central}}\Big], \tag{4.21}$$

$$\Delta\sigma_{\mu-} = -\min_{\{\mu_F,\mu_R\}} \Big[\sigma(\mu_F,\mu_R) - \sigma_{\text{central}}\Big]. \tag{4.22}$$

Because we assign different scales to the light and heavy quark lines for the $2 \to 3$ calculation, the scale uncertainties are evaluated by varying the renormalization and factorization scales independently between $\mu_0^{L,H}/2 < \mu_{F,R} < 2\mu_0^{L,H}$ with $1/2 < \mu_F/\mu_R < 2$ and μ^L/μ^H constant.

PDF uncertainty

Modern PDF sets come with a procedure to evaluate the propagation of their uncertainty onto a given physical observable. This is done by exploring the effect of using, along with a 'central' PDF set, a number of other sets (44 for the `CTEQ6.6` [170] family PDFs) and properly combining their differences. According to the CTEQ6 collaboration, the resulting uncertainty should roughly represent a 90% confidence level. We determine asymmetric uncertainties in the form

$$\Delta\sigma_{\text{PDF}+} = \sqrt{\sum_i \Big(\max\Big[\sigma(set_{+i}) - \sigma(set_0), \sigma(set_{-i}) - \sigma(set_0), 0\Big]\Big)^2}, \tag{4.23}$$

$$\Delta\sigma_{\text{PDF}-} = \sqrt{\sum_i \Big(\max\Big[\sigma(set_0) - \sigma(set_{+i}), \sigma(set_0) - \sigma(set_{-i}), 0\Big]\Big)^2}. \tag{4.24}$$

where all cross sections are evaluated using our central scale choices.

In eqs. (4.23) and (4.24), set_0 represents the central set, and the sums run over all pairs of PDFs in the given PDF error set. For each pair, we denote by set_{+i} and set_{-i} the positive and negative displacement member of the pair.

Results

Table 4.2 shows the predictions for the total cross sections in the two schemes, together with their theory uncertainties. For the Tevatron, we see that the rather large difference of $\sim 30\%$ at LO between the five and four flavor schemes almost vanishes at NLO, where the difference is about 6% and well within the theory uncertainties, which are dominated by the PDF uncertainties. At the LHC the NLO corrections are very small, $\sim 2\%$ in both schemes. The PDF and scale uncertainties are of similar order for the five flavor scheme $(3-4\%)$, while in the four flavor calculation the scale uncertainties are slightly larger and of the order of $4-5\%$. At LO the difference between the four and five flavor schemes is about 8%, which does decrease when including the NLO corrections. For both the Tevatron and the LHC, the small scale uncertainties together with quite modest increases of the cross sections from LO to NLO provide a clear indication that the perturbative expansions in both schemes are very well behaved.

When the PDF and scale uncertainties are combined linearly, as is done in Fig. 4.5, the difference between the NLO predictions in the two schemes is rather small. The figure shows that there is a clear agreement at the Tevatron, while at the LHC the uncertainty bands overlap, but only marginally. This difference could be a hint that the resummation of the logarithms in the PDF in the five flavor scheme is important, or that a NNLO calculation is needed.

Scheme	TeV $t\,(=\bar{t})$	LHC t	LHC $\bar{t}$
	(LO) NLO	(LO) NLO	(LO) NLO
5-flavor $(2 \to 2)$	(0.92) $1.00^{+0.03+0.10}_{-0.02-0.08}$	(153) 156^{+4+3}_{-4-4}	(89) 93^{+3+2}_{-2-2}
4-flavor $(2 \to 3)$	(0.68) $0.94^{+0.07+0.08}_{-0.11-0.07}$	(143) 146^{+4+3}_{-7-3}	(81) 86^{+4+2}_{-3-2}

Table 4.2: Inclusive cross sections (in pb) for t-channel single top production at the Tevatron and LHC using (`CTEQ6L1`) `CTEQ6.6` PDF's for the (LO) NLO predictions and $\mu_0^L = m_t$ ($\mu_0^H = m_t$) and $\mu_0^L = m_t/2$ ($\mu_0^H = m_t/4$) as central values for the factorization and renormalization scales for the light (heavy) line in the 5F and 4F schemes, respectively. The first uncertainty comes from scale variations, the second from PDF errors. The scale uncertainties are evaluated by varying the renormalization and factorization scales independently between $\mu_0^{L,H}/2 < \mu_{F,R} < 2\mu_0^{L,H}$, with $1/2 < \mu_F/\mu_R < 2$ and keeping μ^L/μ^H fixed and the PDF uncertainties by running the 44 `CTEQ6.6` eigenvector PDF sets.

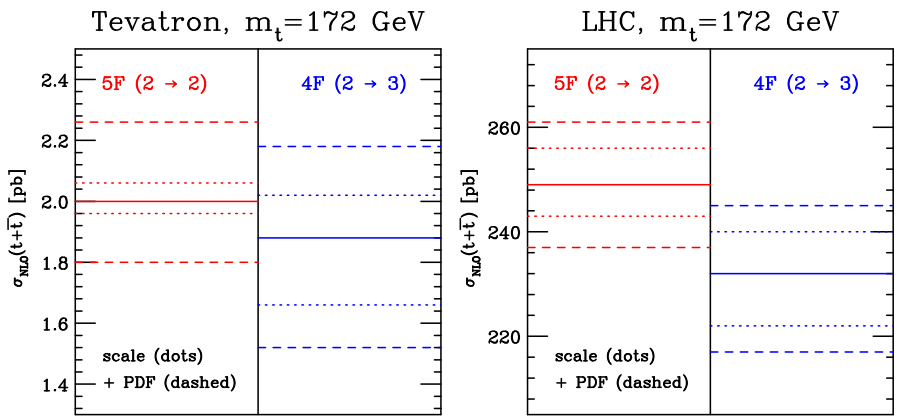

(a) (b)

Figure 4.5: Total NLO cross section including scale and PDF uncertainties at the Tevatron (a) and LHC (b). Cross sections include both top and anti-top production.

$2 \to 2$ and the b quark mass

Most available Monte Carlo implementations so far consistently neglected the bottom quark mass [49, 50, 54–58]. Although there is no difference in the cross section and kinematics for the top quark or light jet, the kinematics for the spectator bottom quark is significantly affected, compared to the procedure described in Ref. [150, 151]. In this procedure the initial state b quarks have to be considered massless, while for the real correction contributions with a final state b quark, $qg \to q' t \bar{b}$, the b mass has to be taken into account. The most striking difference is that the transverse momentum "diverges" at zero for a massless b quark, while the result shows a more physical behaviour if the mass is not neglected. In Fig. 4.6 the b quark p_T distribution is plotted using both the massless b quark approximation and the procedure with the massive final state b quark, both in the five flavor scheme at the Tevatron.

As can be clearly seen, the mass plays a significant role at small transverse momenta, while above ~ 18 GeV the difference can be neglected, as expected. In all our results we explicitly use a finite b quark mass if the b quark is a final state particle.

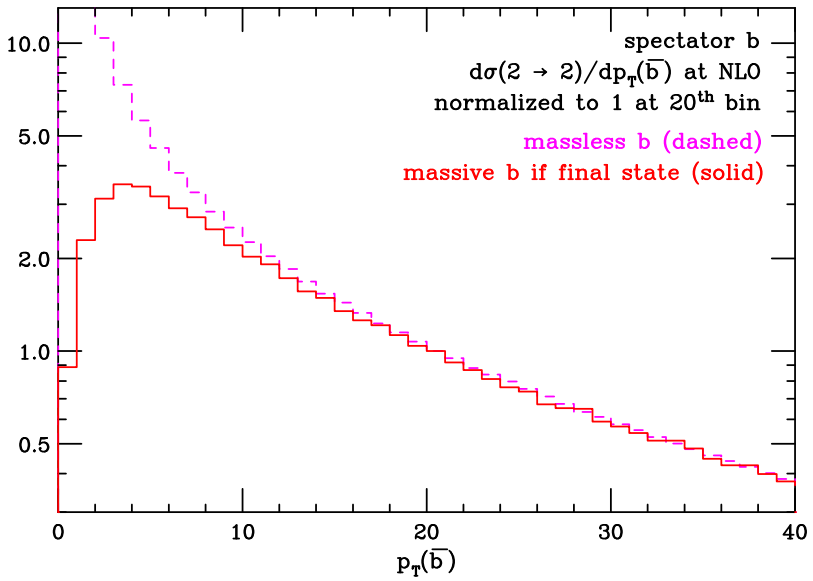

Figure 4.6: Transverse momentum of the spectator b at the Tevatron using the massless approximation (*dashed line*) and the procedure outlined in Refs. [150, 151] with $m_b = 4.5$ GeV (*solid line*).

4.7.3 Differential distributions

In Fig. 4.7 we compare NLO predictions for the top quark pseudo rapidity η and transverse momentum p_T. In this figure (and also in Figs. 4.8 and 4.9) in the upper plots the (normalized) distributions for the Tevatron and LHC are plotted in the 5F (dashed histograms) and 4F (solid histograms) schemes. In the lower plots the the bin-by-bin ratio of the normalized (4F and 5F) distributions is depicted by the dotted histograms, with the solid line a best fit for this ratio to smooth some of the the statistical uncertainties. For the LHC only top production is shown, with the behaviour of the anti-top very similar. Although the predictions differ somewhat, the differences are typically below the 10% level where the cross section is large and always less than 20%.

Similar results can be seen for the differences in the transverse momentum p_T and pseudo rapidity η of the light jet, see Fig. 4.8. There are small differences between the 5F and 4F predictions, but they are of similar size as the differences found for the top quark distributions.

Next, we study the NLO distributions in η and p_T for the spectator b. From Fig. 4.9 we see that the largest effects in the shapes are present at the Tevatron,

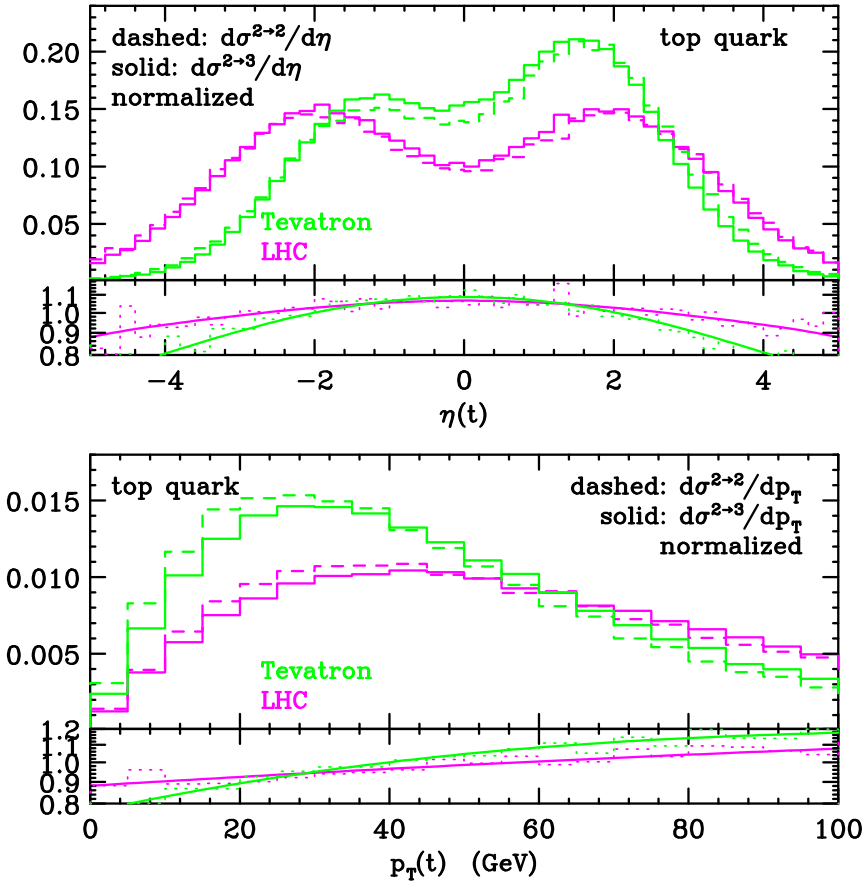

Figure 4.7: Normalized distributions (upper plots) in η and p_T and shape comparison (lower plots) of the $2 \to 3$ and $2 \to 2$ calculations of the top quark at NLO.

where the spectator b tends to be more forward and softer at high p_T than in the 5F calculation (where these observables are effectively only at LO). Even though the b quarks are softer and more forward in the four flavor scheme, the prediction is that more events with a spectator b jet are detectable compared to the five flavor scheme calculation. The reason is that in the five flavor scheme only a subset of the real emission corrections contain the spectator b, while for the $2 \to 3$ already at LO it is present. In the following paragraphs these predictions are quantified, but we first comment on our treatment of the final state b quark.

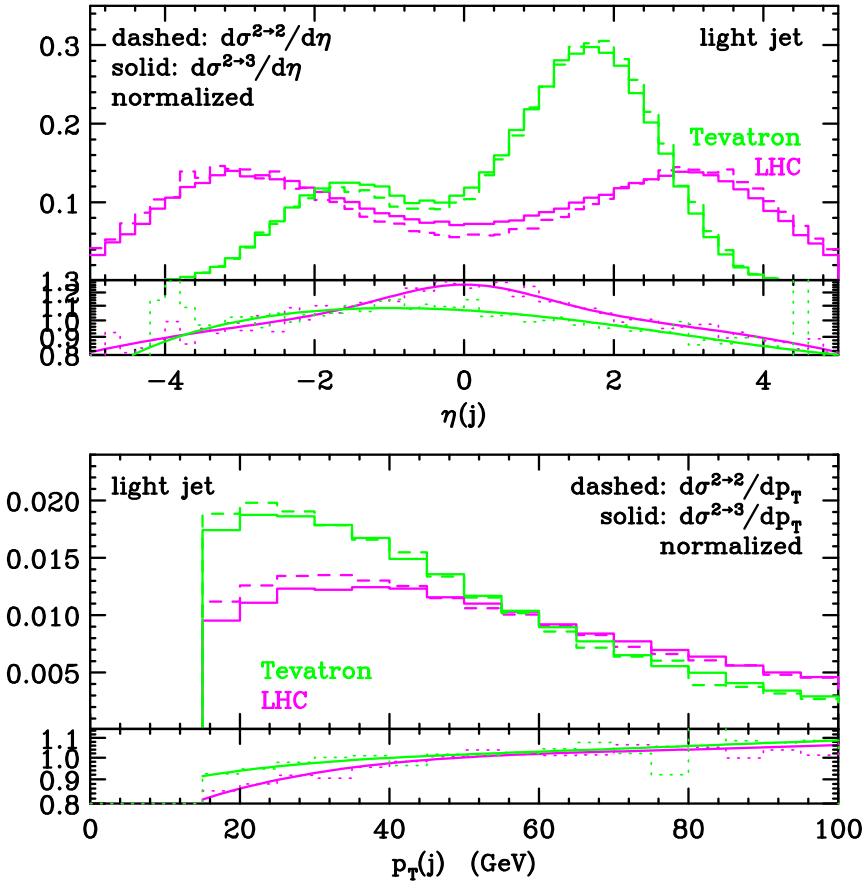

Figure 4.8: Normalized distributions (upper plots) in η and p_T and shape comparison (lower plots) of the $2 \to 3$ and $2 \to 2$ calculations of the light jet at NLO.

Open b quark versus b jet

Because we treat the final state b quark massive there are two ways of describing and studying it. The first, which is the one adopted here, is as an "open" quark, for which we are interested in the momentum of the b quark itself, regardless of the kinematics of the event in which it is embedded. The second way to define it would be as a final state jet which contains the b quark. In this case the momentum of the jet is of interested regardless of the fraction carried by the b quark. A priori, we can expect that the distributions defined by using the jet momenta are better described by perturbative calculations and to have

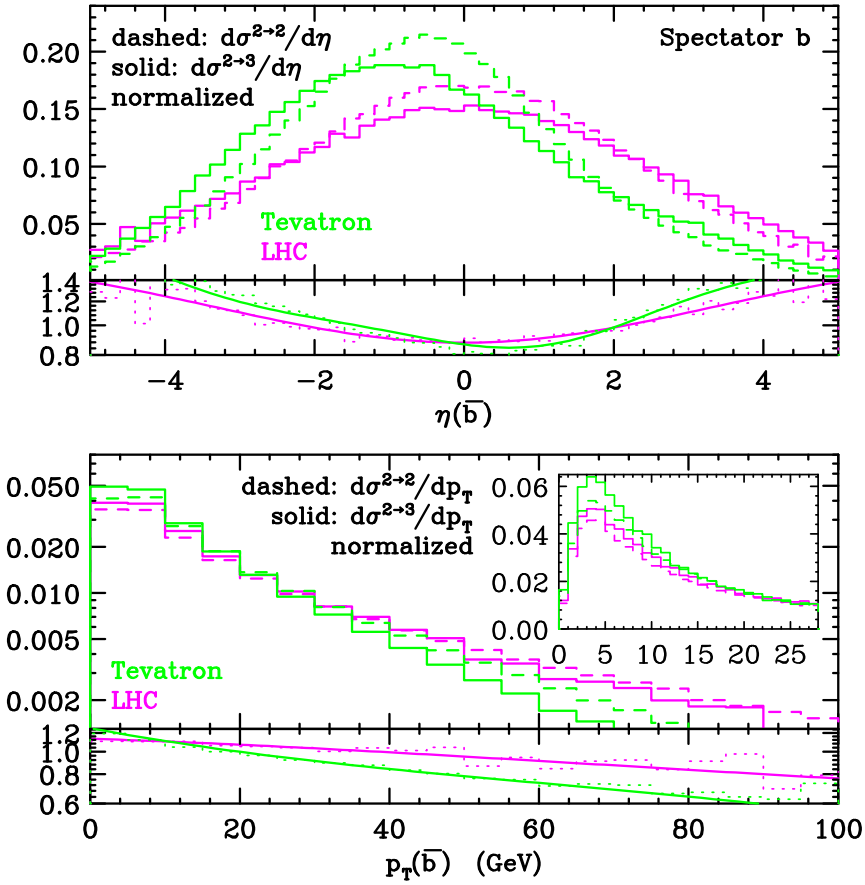

Figure 4.9: Normalized distributions (upper plots) in η and p_T and shape comparison (lower plots) of the $2 \to 3$ and $2 \to 2$ calculations of the spectator b at NLO.

a smaller scale dependence, compared by using the open b quark momentum itself. This is mainly due to the fact that at high transverse momentum for the open b quark description, logarithms of the form $\log(p_T/m_b)$ become large and need to be resummed. In the case where we study b jets, these large logarithms are absent because the jet is insensitive to the momentum fraction carried by the b quark.

As we have seen in Fig. 4.9, the bulk of the cross section is at small p_T. The cross section as a function of the transverse momentum of the b quark drops quickly for increasing masses. Therefore the logarithms $\log(p_T/m_b)$ are small

over most of the phase space and the differences between the open b quark and b jet descriptions are small. Only if stringent cuts on the transverse momenta of the b quark are put or other studies of the large b quark p_T phase space, specification of the description of the open b quark versus b jet needs to be provided.

Furthermore in a study of these phenomena in QCD $b\bar{b}$ production at NLO [172] it has been found that the largest difference is coming from cases in which the two b quarks coming from the gluon splitting are close to each other and (would) end up in the same jet. In our case we do not have such contributions, because one of the b quarks is coupled to the t-channel W boson. Therefore we can expect that the differences between the open b quark and the b jet are very small.

Acceptance b quark and scale dependence

The ratio of events with a b quark in this central region together with a minimum transverse momentum over the total number of t-channel single top events is called the acceptance. It is a measure of the expected fraction of the events with a spectator b quark that can be detected in the experiment.[†]

The two Tevatron experiments, CDF and DØ, use tree-level Monte Carlo generators validated against NLO computations to simulate events [173]. CDF uses `MadGraph/MadEvent` [95] to simulate two event samples, $qb \to tq'$ and $qg \to t\bar{b}q'$, and rescales them to the NLO cross section. In particular, the weight given to each sample is chosen such that the sum matches exactly the acceptance coming from the NLO Monte Carlo `ZTOP` [54, 146]. DØ uses the ("approximate NLO") `SingleTop` [174] event generator. This Monte Carlo program also produces two event samples which are separated by a cut on the transverse momentum of the spectator b quark *after showering*. The value for the cut is chosen in such a way that there is a smooth transition between the $2 \to 2$ and $2 \to 3$ event samples. Although these choices are completely legitimate, the acceptance is effectively a LO quantity, because the spectator b only enters as real emission correction to the LO. Therefore, it has a large scale uncertainty that has to be taken into account properly.

The calculation presented here, *i.e.*, the NLO corrections in the four flavor scheme, predict the distributions of the spectator b quark for the first time beyond leading order. Therefore we expect a more precise and stable prediction

[†]Also events that do not pass the spectator b quark acceptance cuts are detected. In fact, these are in general considered to be "t-channel events", while the events that pass the cuts have more s-channel like kinematics. [173]

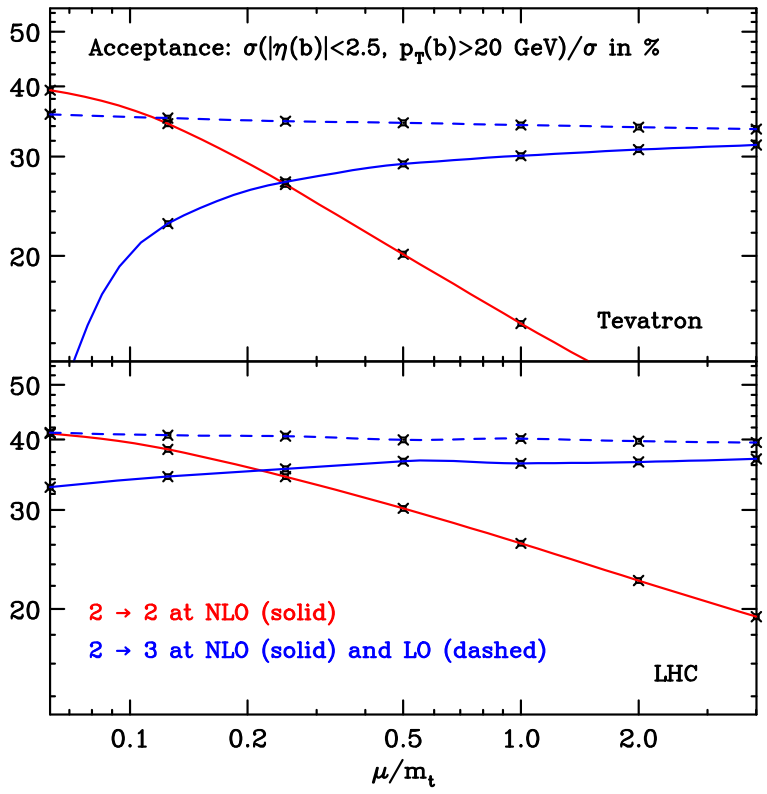

Figure 4.10: The acceptance, $\sigma(|\eta(b)| < 2.5, p_T(b) > 20 \text{ GeV})/\sigma_{\text{Incl.}}$, for t-channel single top production at the Tevatron (*upper plot*) and LHC (*lower plot*). Only top production is considered, anti-top production being the same at the Tevatron and very similar at the LHC.

for the acceptance using the NLO approximation of the $2 \to 3$ process compared to previous results.

In Fig. 4.10 we plot the acceptance as a function of the scales, $\mu_F = \mu_R = \mu$, at the Tevatron and LHC for a generic set of cuts for the spectator b quark,

$$\frac{\sigma(|\eta(b)| < 2.5, p_T(b) > 20 \text{ GeV})}{\sigma_{\text{Incl.}}} . \tag{4.25}$$

These plots show several properties of the calculations in the five and four flavor schemes:

I. The NLO predictions starting from the $2 \to 2$ Born process predict a lower acceptance compared to the predictions starting from the $2 \to 3$ Born process. For our default central choices for the scales, $\mu_R = \mu_F = m_t$ for the $2 \to 2$ and $\mu_R^L = \mu_F^L = 2\mu_R^H = 2\mu_F^H = m_t/2$ for the $2 \to 3$, there is almost a factor two difference at the Tevatron and a factor 1.4 at the LHC.

II. As expected, the NLO predictions starting from the $2 \to 2$ Born process show a very large dependence on the renormalization and factorization scales. As already explained above, the acceptance calculated from the $2 \to 2$ NLO process is truly a LO quantity, because the numerator in Eq. 4.25 is trivial when not including the radiative corrections to the $2 \to 2$ Born process. In fact, this numerator can be calculated by simply using the $2 \to 3$ LO process and has therefore a large scale dependence as can be seen in Fig. 4.4. The denominator in Eq. 4.25 is a NLO number and is very stable under scale variations, see Fig. 4.4. Therefore the ratio inherits the large scale dependence from the numerator.

III. The calculation presented here, *i.e.*, the NLO predictions to the $2 \to 3$ Born process, show only a mild dependence on the scales, except for very small scales at the Tevatron. This reflects the fact that this calculations predicts the acceptance for the first time at NLO.

IV. The dashed line in Fig. 4.10 is very stable under scale uncertainties, even though this is just a pure LO prediction. The reason for this is that there are large cancellations between the numerator and the denominator in the ratio, Eq. 4.25. The $2 \to 3$ LO prediction lacks the more involved dependence on the scales that is needed to correctly access the uncertainty of this quantity by only varying the scales.

Table 4.3 shows the predictions for the acceptance in the two schemes, together with their scale uncertainties. These uncertainties are evaluated in the same way as for the total cross section, see Sec. 4.7.2. We see that the uncertainty for the $2 \to 2$ process at the Tevatron is 25-30% and much larger than for the prediction in the four flavor scheme, which is of the order of 10%. Even though these uncertainties are large, the two approximations are barely in agreement with each other because the acceptance in the four flavor scheme is almost two times larger than using the five flavor scheme.

At the LHC the situation is similar. Also here the prediction in the five flavor scheme underestimates the acceptance by a large amount and has a relatively large scale uncertainty. The NLO prediction starting from the $2 \to 3$ Born is better behaved and has only a small uncertainty.

The large scale uncertainty of the acceptance predicted by the NLO $2 \to 2$ has not been taken into account by the CDF's and DØ's analyses. Only the scale uncertainty in the total cross section, as given in Fig. 4.4, has been considered properly. The prediction used by DØ, by the `SingleTop` MC, gives a value for the acceptance of 30%. This is remarkably close the the NLO prediction, see Table 4.3 and also the (p_T and η) distributions for the spectator b are in agreement. Therefore no extensive modifications to the DØ analyses are needed. On the contrary, CDF uses the value predicted by `ZTOP`, with scales equal to the DDIS scales [146] (which are very similar to our default choices for the scales for the $2 \to 2$, $\mu_R = \mu_F = m_t$), and is therefore almost a factor two smaller than our best prediction, see Table 4.3. The consequences of this difference for the recent discoveries of single top quarks are rather difficult to access without completely redoing CDF's analyses. Even so, naively one can expect that

- the total cross section for single top production (s- and t-channel) does not change significantly, and
- the measured cross section for s-channel will go down and t-channel will go up.

The sum of the s- and t-channel cross section does not go down, because t-channel events that do not pass the acceptance cuts still have a top quark and one or more light jets in the final state. These are the events that are considered to be t-channel by the CDF (and DØ) collaborations [173]. The events that pass the acceptance cuts have very similar kinematics as the s-channel events, a final state top, b and possible light jets. Therefore, in general, these events

Scheme	TeV $t\,(=\bar{t})$ (LO)	TeV $t\,(=\bar{t})$ NLO	LHC t (LO)	LHC t NLO	LHC $\bar{t}$ (LO)	LHC $\bar{t}$ NLO
5-flavor ($2 \to 2$)		15^{+5}_{-3}		26^{+4}_{-3}		26^{+4}_{-4}
4-flavor ($2 \to 3$)	(35)	28^{+2}_{-3}	(40)	36^{+1}_{-2}	(40)	36^{+1}_{-2}

Table 4.3: The acceptances, $\sigma(|\eta(b)| < 2.5,\, p_T(b) > 20\text{ GeV})/\sigma_{\text{Incl.}}$, and their scale uncertainties for t-channel single in percentages (%) at the Tevatron and LHC using the default central scale choices, $\mu_0^L = \mu_0^H = m_t$ ($\mu_0^L = m_t/2$ $\mu_0^H = m_t/4$) for the 5 (4) flavor calculations. The scale uncertainties are evaluated by varying the renormalization and scales independently between $\mu_0^{L,H}/2 < \mu_{F,R} < 2\mu_0^{L,H}$, with $1/2 < \mu_F/\mu_R < 2$ and keeping μ^L/μ^H fixed

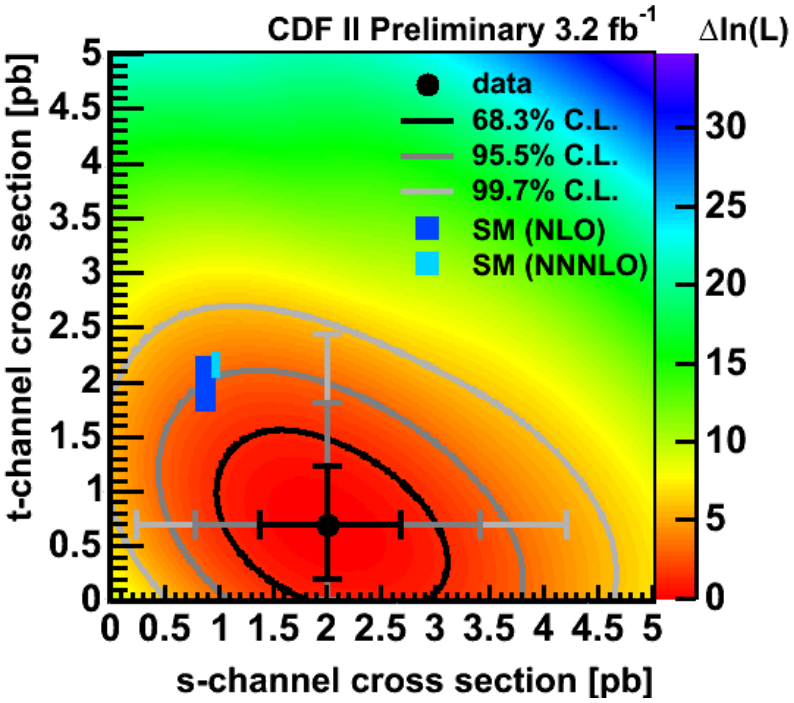

Figure 4.11: Measurement of the single top cross sections by the CDF collaboration. From Ref. [145].

have been considered as s-channel. With the new calculation presented here, a larger fraction of events passes the acceptance cuts, which means that a larger fraction of the tbj events are t-channel events, not s-channel. This might help in the explanation of the two standard deviation excess of s-channel and lack of t-channel events found by CDF using Neural Network techniques [145], see Fig. 4.11.

4.8 From SM single top to a fourth generation

In the previous sections of this chapter it is discussed that the $2 \to 2$ and $2 \to 3$ NLO approximations are in good agreement with each other. The results were presented using a fixed top and bottom quark masses set to $m_t = 172$ GeV and $m_b = 4.5$ GeV, and a single PDF set, `CTEQ6.6`.

In this section we will extend these result for the total cross section to study the dependence on the top and bottom quark masses, use a differnt PDF set and predict the cross section for fourth generation $t'b$, tb' and $t'b'$ production.

As before, our best prediction is computed using for the $2 \to 3$ calculation separate scales on the light and heavy quark lines (μ_l and μ_h respectively), where $\mu_l = (m_t + m_b)/2$ and $\mu_h = (m_t + m_b)/4$. The $2 \to 2$ calculation, which has only a very mild scale dependence, uses a single overall scale, $m_t/2$ and for both processes the renormalisation and factorisation scales are equal. This choice of central scales is motivated by a good agreement between the $2 \to 2$ and $2 \to 3$ calculations for the physical top mass, see Sec. 4.7.2. We have checked that a similar preference for smaller scales on the heavy quark line is shown for much larger top quark masses.

We present results for two choices of recent PDF family, `CTEQ6.6` [170] and `MSTW2008` [169]. Our central prediction for each of these choices corresponds to the best fit for each family. We note that, since these are 5-flavor PDF sets, we pass to the 4-flavor scheme necessary for a consistent calculation of the tb and $t'b$ $2 \to 3$ processes by including the counter terms of Ref. [171] as explained in Sec. 4.7.1. For tb' and $t'b'$ we always use the pure 5-flavor PDFs.

We present here the cross sections for single-top and t' production, obtained from both the $2 \to 2$ and $2 \to 3$ calculations. We show results for the Tevatron and for two LHC energies, 10 TeV and 14 TeV. For single-top production we show results for a number of different values of the top mass around the current best determination [175] and for t' production we investigate masses as large as 2 TeV (at the LHC). The cross sections and uncertainties are tabulated in Appendix B in Tables B.1 and B.2 (Tevatron), Tables B.3 and B.4 (LHC, 10 TeV) and Tables B.5 and B.6 (LHC, 14 TeV). For each machine, the two tables correspond to our two choices of central PDF, `CTEQ6.6` and `MSTW2008`. Note that, at the LHC, the rates for production of a heavy top (or t') are different from those of its antiparticle and the two are thus tabulated separately. In addition, the `CTEQ6.6` results (with t and $\bar{t}$ production summed) are illustrated in Figures 4.12 (Tevatron), 4.13 (LHC, 10 TeV) and 4.14 (LHC, 14 TeV), where we also show the rates for the corresponding strong pair production for comparison, which falls of much steeper with increasing top quark mass, as expected.

A number of global features are evident from these results:

I. As discussed in Sec. 4.7.2, the central cross sections predicted by the $2 \to 2$ and $2 \to 3$ processes differ by 5% or less, both at the Tevatron and at the LHC, for masses around the top quark. At the Tevatron, the

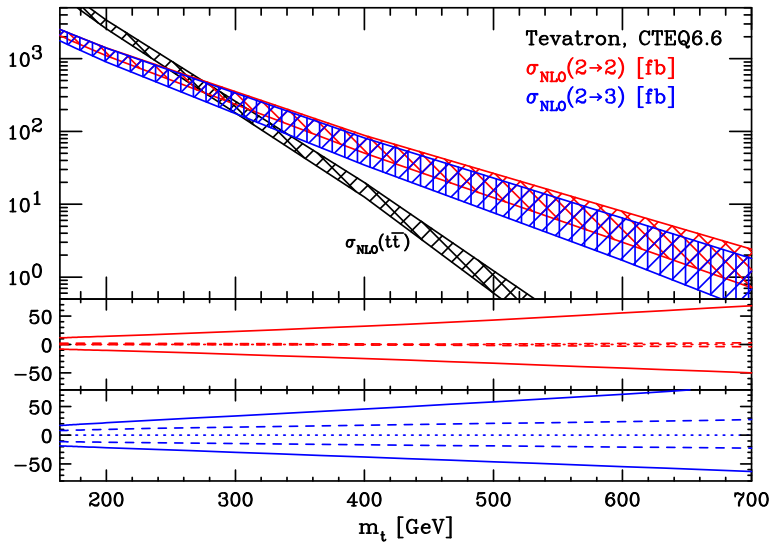

Figure 4.12: Cross sections (fb) at the Tevatron Run II for the sum of top and anti-top quark production in the t channel, as a function of the top mass obtained with the CTEQ6.6 PDF set and $V_{t^{(\prime)}b} = 1$ in the $2 \to 2$ and $2 \to 3$ schemes. Bands are the total uncertainty (scale+PDF). In the lower plots, dashed is scale uncertainty, solid is scale + PDF. The corresponding data is collected in the appendix, Table B.1.

difference is well within the combined uncertainty from higher orders and PDFs, so we conclude that the two calculations are consistent. At the LHC (10 and 14 TeV) the consistency is marginal, in particular because the uncertainties from the PDF's are (almost) 100% correlated between the two approximations. This is demonstrated in Fig. 4.15, which shows a scatter plot of the $2 \to 2$ and $2 \to 3$ cross sections, with each point evaluated using one of the individual PDF uncertainty sets (the set_{+i} and set_{-i} appearing in Eqs. 4.23 and 4.24). We note therefore that in a combined estimate of the total production cross section, the PDF errors should *not* be summed.

II. For larger masses, *i.e.*, for t' production, the differences are much larger. For a mass of 1 TeV, the $2 \to 2$ prediction using the `CTEQ6.6` PDF set is almost twice as large at the Tevatron and 20% bigger at the LHC. However for such large t' masses we expect that the phase space of producing the spectator b quark is lowering the $2 \to 3$ cross section. Moreover, the

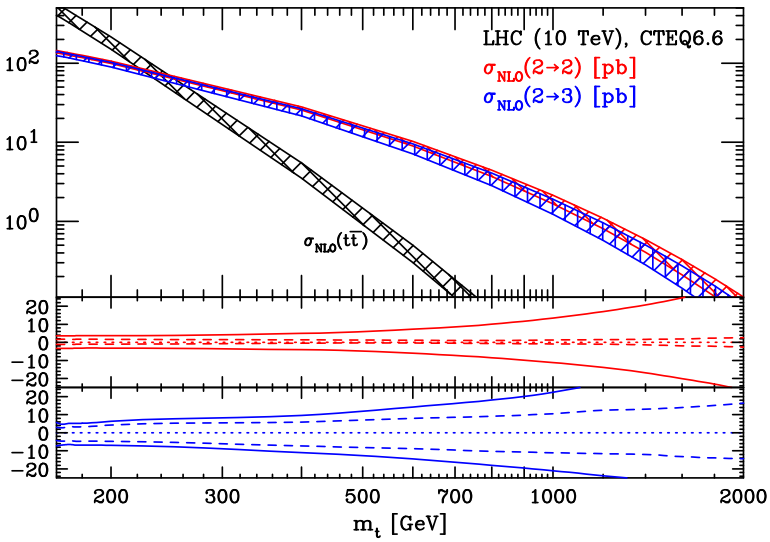

Figure 4.13: The same as Figure 4.12 but for the LHC 10 TeV. The corresponding data is collected in the appendix, Table B.3.

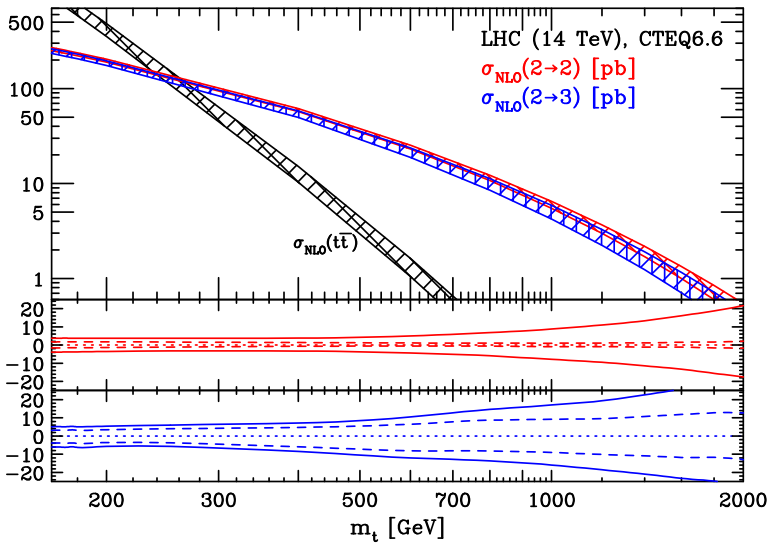

Figure 4.14: The same as Figure 4.12 but for the LHC 14 TeV. The corresponding data is collected in the appendix, Table B.5.

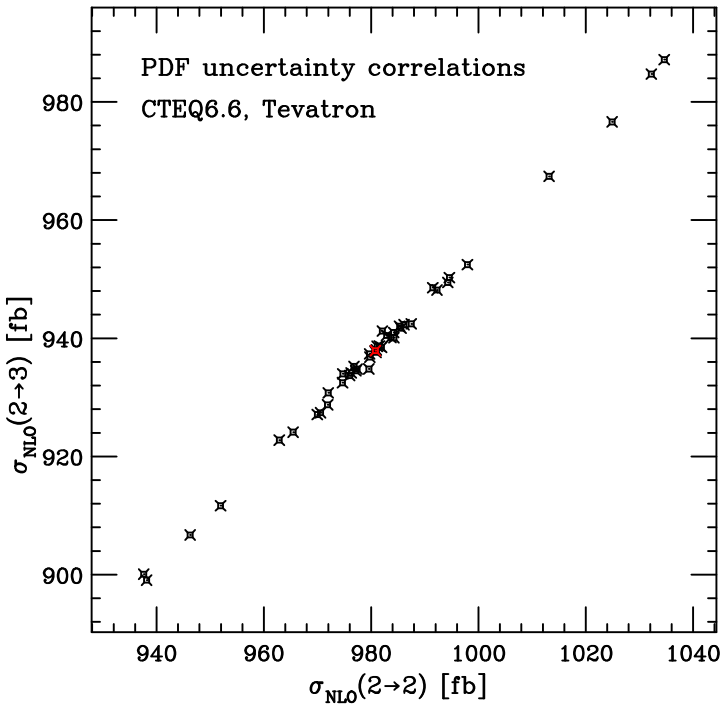

Figure 4.15: Scatter plot that shows the correlations in the PDF uncertainty between the $2 \to 2$ and $2 \to 3$ calculations at the Tevatron. Both LHC 10 TeV and LHC 14 TeV show the same (almost) 100% correlated uncertainties.

scale choice for the heavy quark line in the $2 \to 3$, $(m_{t'} + m_b)/4$, is consistent, but we have checked that a somewhat smaller scale for the very heavy masses, like $m_{t'}/8$, gives a slightly better perturbative behavior. A smaller scale also increases the cross section and brings the results of the two approximations closer. Nevertheless we see that the differences between the two calculations can still be accounted for by their uncertainties (with the same PDF caveats as above).

III. The uncertainty coming from higher orders is estimated to be much larger for the $2 \to 3$ process, particularly at the Tevatron. This is to be expected, since the perturbative series for this process begins at $\mathcal{O}(\alpha_s)$ rather than the purely electroweak leading order for the $2 \to 2$ calculation. Our estimate ascribes uncertainties that are typically at the level of a few percent, except for the $2 \to 3$ calculation at the Tevatron where they

range from about 10% for the top quark to as large as 30% for a 1 TeV t'.

IV. Results from the two different PDF sets are generally in good agreement with one another at NLO. For the top quark, differences are at the level of a couple of percent or less in the $2 \to 2$ calculation, a few percent for the $2 \to 3$ process and are smaller at the LHC than at the Tevatron.

The uncertainty on the cross sections deriving from the PDFs is different between the Tevatron and the LHC. At the Tevatron the PDF uncertainty is particularly large, with the `CTEQ6.6` set yielding approximately a 10% uncertainty for the top quark (slightly smaller for `MSTW2008`), whilst for a t' it can be considerably larger. This simply represents the limitations of current global PDF determinations, where the gluon distribution at large momentum fractions is not greatly constrained by data. This explains not only the much larger percentage uncertainties, but also the greater difference between the `CTEQ6.6` and `MSTW2008` predictions. For such large masses the cross sections presented here clearly have little phenomenological interest at the Tevatron.

At the LHC the PDF uncertainty on the $2 \to 2$ single top quark cross section is comparable to that coming from the unknown higher orders, whilst it is somewhat smaller for the $2 \to 3$ calculation. For single t' production the two sources of uncertainty are comparable in the $2 \to 3$ case, but the uncertainty from the PDFs clearly dominates for the $2 \to 2$ process.

Single top cross sections in the SM: bottom and top mass dependence

For the case of single top production in the Standard Model, whose cross section can be predicted quite accurately, it is important to investigate in detail its dependence on both heavy quark masses. In the following we discuss the bottom and top mass effects independently, having checked explicitly that this is a very good approximation.

To our knowledge the bottom quark mass dependence of the total single top cross section has never been addressed in detail. There are two different ways in which the bottom mass can enter the final results, *i.e.*, through logarithmic and power correction terms. In the $2 \to 3$ calculation both effects explicitly depend on the pole mass parameter that is already present at LO in the matrix element (and in the phase space boundaries). In the $2 \to 3$ based computation it is therefore trivial to quantify the bottom mass dependence. On the other hand, disentangling the relative impact of the logarithmic terms from those that

are power suppressed requires some analytical work. In the $2 \to 2$ calculation the situation is reversed. The two sources are separated from the start: the effect of the logarithms is resummed in the bottom PDF while the power-like terms at NLO come from the (subtracted) real correction diagrams $qg \to tbq'$. The effect of the b mass from the latter source has already been studied, see for instance Ref. [146], and found to be very small. We have checked that changing the bottom mass from $\sim$5 GeV to zero results in a difference below 0.5%. However the logarithmic corrections, which have so far been neglected, are quite sizable. In the $2 \to 2$ calculation the logarithmic dependence on the bottom quark mass is "hidden" in the starting condition for the evolution of the b-PDF. To study its impact we have generated various sets of PDFs for different bottom masses in the range 4 GeV$< m_b <$5 GeV, using the evolution code provided by the CTEQ collaboration. As a result we find that the $2 \to 2$ cross sections on average decrease by about 1.2%, 0.86%, 0.80% per 100 MeV increase of m_b at the Tevatron, LHC at 10 TeV and 14 TeV, respectively. Such a dependence is fully reproduced by the $2 \to 3$ calculation which gives similar (corresponding) results, namely 1.0%, 0.83% and 0.76%. We conclude that the b mass dependence should be included as a source of uncertainty in the final predictions for the SM total cross sections.

As far as the top quark mass dependence is concerned, this can be studied easily in both the $2 \to 2$ and $2 \to 3$ calculations. Here we provide formulae that can be used to obtain the cross section and the corresponding uncertainties for any top quark mass in the range 164 GeV $< m_t <$ 180 GeV, to an accuracy better than 1%. We fit the mass dependence of the cross section using a quadric centered on $\sigma_0 = \sigma(m_t = 172 \text{ GeV})$,

$$\sigma(m_t) = \sigma_0 \left[1 + \left(\frac{m_t - 172}{172} \right) A + \left(\frac{m_t - 172}{172} \right)^2 B \right] , \tag{4.26}$$

where m_t is measured in GeV. The (dimensionless) coefficients A and B for both the $2 \to 2$ and $2 \to 3$ processes are given in Table 4.4.

Collider		Born	MSTW2008			CTEQ6.6		
			σ_0	A	B	σ_0	A	B
Tevatron	$t = \bar{t}$	$2 \to 2$	$994^{+24\ +61}_{-2\ -52}$	-3.01	5.2	$981^{+23\ +98}_{-3\ -82}$	-2.97	5.0
		$2 \to 3$	$942^{+86\ +53}_{-113\ -43}$	-3.11	4.9	$935^{+82\ +88}_{-107\ -74}$	-3.08	5.3
LHC (10 TeV)	t	$2 \to 2$	$84.4^{+1.4\ +1.1}_{-1.0\ -1.0}$	-1.48	1.1	$83.5^{+1.4\ +1.5}_{-1.1\ -1.7}$	-1.50	1.0
		$2 \to 3$	$80.3^{+3.2\ +1.1}_{-3.7\ -1.0}$	-1.60	2.2	$79.8^{+2.9\ +1.4}_{-3.4\ -1.6}$	-1.54	3.3
	$\bar{t}$	$2 \to 2$	$48.3^{+0.8\ +0.7}_{-0.5\ -1.0}$	-1.57	1.7	$46.6^{+0.8\ +1.0}_{-0.5\ -1.1}$	-1.58	1.2
		$2 \to 3$	$45.4^{+1.7\ +0.7}_{-2.1\ -1.0}$	-1.54	0.4	$44.2^{+1.2\ +1.0}_{-2.0\ -1.1}$	-1.68	0.9
LHC (14 TeV)	t	$2 \to 2$	$154.3^{+2.9\ +2.2}_{-2.5\ -2.2}$	-1.32	1.1	$152.9^{+3.0\ +3.0}_{-2.3\ -3.4}$	-1.35	2.2
		$2 \to 3$	$146.8^{+4.3\ +2.2}_{-5.0\ -2.1}$	-1.40	4.6	$147.0^{+5.0\ +2.7}_{-5.7\ -3.1}$	-1.35	0.9
	$\bar{t}$	$2 \to 2$	$94.2^{+1.6\ +1.2}_{-1.5\ -1.9}$	-1.42	1.1	$91.1^{+1.5\ +1.8}_{-1.5\ -2.1}$	-1.42	0.7
		$2 \to 3$	$88.7^{+2.6\ +1.3}_{-3.0\ -1.8}$	-1.49	3.1	$86.8^{+2.4\ +1.8}_{-3.7\ -2.0}$	-1.46	0.9

Table 4.4: Parameters to interpolate the cross section (in fb for the Tevatron, pb for the LHC) and the corresponding uncertainties for top quark masses around the default value of $\sigma_0 = \sigma(m_t = 172\ \text{GeV})$.

4.8.1 tb' and $t'b'$ cross sections and uncertainties

Production of a b', together with either a top quark or an additional t', can be computed at NLO accuracy starting from the $2 \to 3$ Standard Model single-top process. Since the final state contains two heavy particles, the expected rates are probably out of the reach of the sensitivity of the Tevatron and early LHC running. Therefore we present results for the 14 TeV LHC energy only, but explore a range of different t' and b' masses.

For $b'\bar{t}$ (and $\bar{b}'t$) production the cross sections and their uncertainties are tabulated for both choices of PDF set in Tables B.7 and B.8, collected in Appendix B. The two sources of uncertainty considered here are of a comparable size, leading to an overall accuracy running from a few percent for $m_{b'} = 200$ GeV up to about 30% for the highest masses considered, once again due to the PDF uncertainty in that kinematic region. The cross sections for the sum of $b'\bar{t}$ and $\bar{b}'t$ production including uncertainties are also plotted in Figure 4.16 for the CTEQ6.6 PDF set. For comparison strong production of b' pairs is also shown.

In the case of $t'b'$ production we consider five different scenarios: $m_{b'} = m_{t'}$, $m_{t'} - m_{b'} = 200$ GeV and $m_{t'} - m_{b'} = 500$ GeV as a function of the t' mass and $m_{b'} - m_{t'} = 200$ GeV and $m_{b'} - m_{t'} = 500$ GeV as a function of the b' mass. The cross sections and uncertainties in these five scenarios are also tabulated in the appendices, for the first three cases together in Tables B.9 and B.10 and for the latter two together in Tables B.11 and B.12, using the CTEQ6.6 and MSTW2008 PDF sets respectively. The CTEQ6.6 results for the first three scenarios are illustrated in Figure 4.17 as the sum of $t'\bar{b}'$ and $\bar{t}'b'$ production, where we also show the NLO rates for $t'\bar{t}'$ for comparison. The latter two scenarios are plotted in Figure 4.18 together with the NLO $b'\bar{b}'$ cross sections and uncertainties for comparison.

We conclude this section by briefly commenting on the symmetry properties of the results for the cross sections. $\mathcal{CP}$ invariance implies that simultaneously interchanging the t' and b' masses, together with the chirality of the Wtb vertex from left- to right-handed, gives the same cross section. By performing either a $\mathcal{C}$ or $\mathcal{P}$ transformation individually, one can pass from the case with $m_{t'} - m_{b'} = 200(500)$ GeV to the case with $m_{b'} - m_{t'} = 200(500)$ GeV, and vice-versa. It is interesting to note that the above cases, while not related by a symmetry, lead to similar total rates. The differences arise from angular dependences in the matrix elements that are proportional to β, the velocity of the heavy quarks. Since these terms are integrated over the available phase space and

they are themselves small for high heavy quark masses, they result in only minor differences.

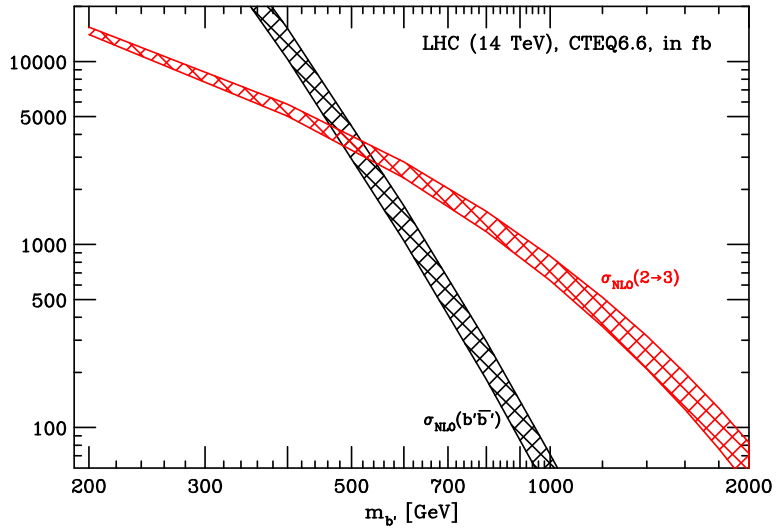

Figure 4.16: Cross sections (fb) at the LHC 14 TeV for $b'\bar{t}$ plus $\bar{b}'t$ production as a function of $m_{b'}$ obtained with the CTEQ6.6 PDF set and $V_{tb'} = 1$. Bands are the total uncertainty (scale+PDF).The corresponding data is collected in Table B.7.

4.9 Conclusions

The recent observation of single top with more than 5 standard deviations significance has opened a new chapter in the study of heavy quarks. The measurement of the cross section is a direct probe of the size of the CKM matrix element $|V_{tb}|$. A value much smaller than one would suggest the presence of new heavy quarks, in particular an extended quark sector. The t-channel mechanism for single top production is particularly sensitive to direct searches of new physics because of the much milder decline of the total cross section with increasing t' (or b') mass compared to pair production.

For both the measurement of single top production in the SM model, as well as the discovery of fourth generation quarks, excellent theory predictions for the cross sections as well as distributions of the final state particles is mandatory.

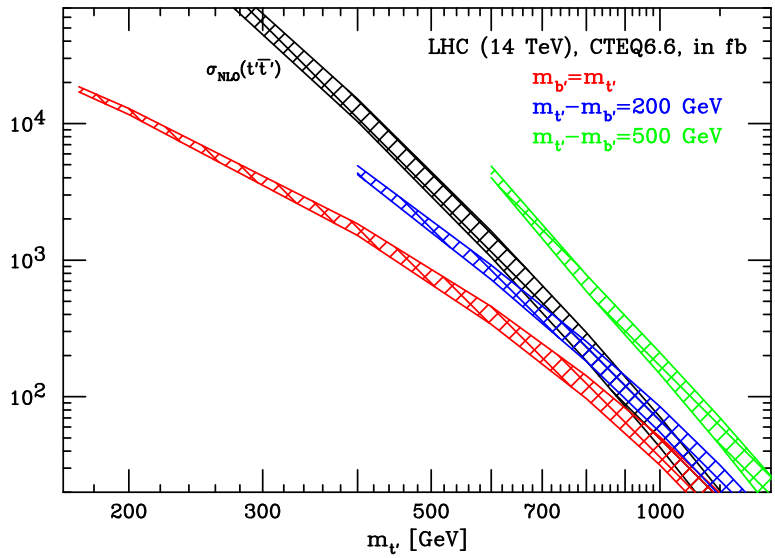

Figure 4.17: Cross sections (fb) at the LHC 14 TeV for $t'\bar{b}'$ plus $\bar{t}'b'$ production as a function of $m_{t\prime}$ obtained with the CTEQ6.6 PDF set and $V_{t'b'} = 1$. Bands are the total uncertainty (scale+PDF). The corresponding data is collected in Table B.9.

We have presented a new NLO calculation of the t-channel single top production mechanism in the four flavor scheme, *i.e.* starting from the $2 \to 3$ Born diagrams. The main advantage of this calculation over previous calculations in the five flavor scheme, *i.e.* with a $2 \to 2$ process at the Born level, is that it gives the spectator b quark distributions, like (pseudo) rapidity, transverse momentum, etc., for the first time at full NLO.

The calculation of the loop diagrams has been performed using conventional Feynman diagram techniques. Similar to the NLO corrections to the 5 flavor scheme approximation (most of) the interferences between the heavy and light quark lines are zero due to the color singlet W boson that connects the two quark lines. This simplifies the calculation, for example, it removes all "pentagons", and allows for a different choice of renormalization and factorization scales for the two quark lines.

The corrections in going from LO to NLO are mild for both the Tevatron and the LHC, for the optimal scale choice. For the $2 \to 3$ the renormalization and factorization scales of the heavy quark line are dictated by initial state gluon splitting to $b\bar{b}$ and should therefore be chosen accordingly. The light quark line

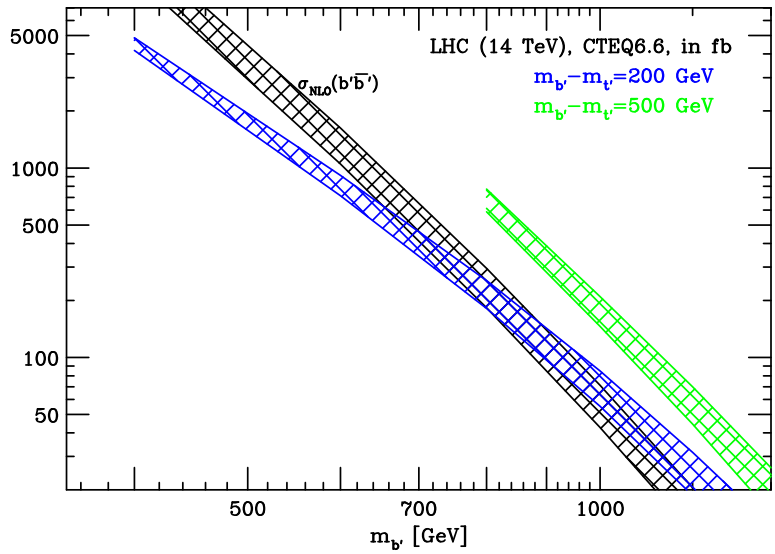

Figure 4.18: Cross sections (fb) at the LHC 14 TeV for $b'\bar{t}'$ plus $\bar{b}'t'$ production as a function of $m_{b'}$ obtained with the CTEQ6.6 PDF set and $V_{t'b'} = 1$. Bands are the total uncertainty (scale+PDF). The corresponding data is collected in able B.11.

shows very limited dependence on the scales, both at LO and at NLO. The NLO approximation shows a very mild scale dependence, so there are no signatures of a badly behaved perturbative series, which suggest that the logarithms of the form $\log(Q^2/m_b^2)$ that are resummed in the PDF in the 5 flavor scheme are not of great importance.

This observation is further confirmed by the fact that the differences between the calculations in the 4 and 5 flavor schemes are small. The total cross section, as well as the distributions for the top quark, light jet and spectator b quark, are similar in the two approximations. However, some observables that were only described (effectively) at LO before, like the ratio of the number of events with an observable spectator b quark over the total number of t-channel events, show significant improvement when calculated at NLO. This may have an effect on the recent observation of EW top production, in particular in the discrimination of t and s-channel events, although due to the rather involved analysis techniques used by the CDF and DØ collaborations this is difficult to quantify.

In Chapter 3 the impact of new physics on the current bounds on the CKM matrix was discussed in detail. In this chapter we have provided an extensive study of the total cross section for heavy colored fermions which are needed to relax the constraint from the unitarity of the CKM matrix. Fourth generation b' and t' production at NLO, including all the theory uncertainties, *i.e.*, scale dependence and PDF uncertainty, has been explored up to masses of 2 TeV (for the LHC). The results are presented in tables that can be used as reference for further experimental and/or theoretical studies.

CHAPTER

FIVE

CONCLUSIONS

Top physics is entering the precision phase at the Tevatron and will be one of the leading priorities at the LHC. The importance of the top quark in the quest for the mechanism of EWSB and new physics is due to the convergence of two factors. First the LHC will be a top factory with tens of millions of top quarks produced (about 5/6 of them in pairs and the rest as EW single top production) in the first years of running at the nominal low luminosity, $2 \times 10^{33}\text{cm}^{-2}\text{s}^{-1}$, allowing studies at an unprecedented level of accuracy. Second, due to its large mass, top is the optimal probe for new physics at TeV scales. Many different models, including the SM, predict the existence of heavy states that preferably couple to the top quark, and that could affect its SM couplings via loop corrections or be directly produced at the LHC. Third, the existence of a fourth generation or more involved models with heavy colored fermions, has serious impact on the currents bounds on the third row of the CKM matrix.

Given the large number of BSM scenarios that have been considered in the literature, and should be searched for at the Tevatron and LHC, a top down approach covering all possibilities of all models is a hopeless task. To narrow down the number of new physics models a more pragmatic bottom up approach might be a more efficient way to make progress. In the second chapter of this thesis we have presented an example on how such a study could be performed.

As a first step the accuracy of an observable, in this case the top pair invariant mass, has been assessed. (In fact we have found that the shape is under such a good theoretical control that it might even be used to measure the top quark

mass). Once the uncertainties on a variable are known, any excess (or deficit) of events hints towards new physics. If this new physics comes as a resonance, the peak in the top pair invariant mass distributions is directly related to the mass of the resonance. In fact, in a recent study by CDF this idea has been followed and used to search for new physics in the top pair invariant mass distribution in a model independent way [103].

The second step is to determine the spin of the resonance. This can be inferred from the angular distribution of the top and anti-top. Finally, more involved observables, like correlations between the (anti) top quark decay products can be used to infer information about the couplings of the resonance.

All the necessary Monte Carlo tools to perform model independent studies to BSM resonances in the top pair invariant mass distribution have been provided and are available on the web.

In the third chapter we used a slightly different approach to set limits on the third row of the CKM matrix in a model independent way. BSM scenarios relax the unitary constraint on this matrix, and constraints from loop induced observables can easily be polluted by BSM contributions. Therefore, the available limits on the third row of the CKM matrix can be seriously relaxed when only direct constraints from top quark decays and single top production are taken into account. Our outline for a possible strategy to use top quark events to set these limits has been communicated to the CDF and DØ collaborations and should be followed in a future analysis.

In the context of single top production we have also calculated the NLO corrections to the t-channel single top production mechanism using a four flavor scheme, as presented in Chapter 4. The corrections are stable compared with the $2 \to 3$ LO prediction if the renormalization and factorization scales are chosen in a reasonable way. The results agree for most observables with a similar NLO calculation in the five flavor scheme, suggesting that the b quark mass logarithms that are resummed in the PDF in the five flavor scheme are not very important.

The important improvement compared to previous calculation has been that the spectator b quark distributions are, for the first time, computed at NLO. This has lead to a prediction of a much larger number of events with an observable spectator b quark compared to estimations based on naive $2 \to 2$ calculations. From discussions with the CDF and DØ top quark group members, it can be concluded that the theoretical predictions used by DØ are in agreement with our computation and need no modification. However, the Monte Carlo

predictions used by CDF differ and they are working to take this difference into account in their analyses.

This new prediction has also been used to give NLO predictions for fourth generation quark production, both t' and/or b', at the Tevatron and LHC. The results are presented in table form and in plots.

5.1 Outlook

The model independent approach to look for BSM signatures in the top pair invariant mass as introduced in the second chapter of the thesis, can be extended to other discovery channels. A similar study, for instance, could be performed in the context of single top production as this process is sensitive to different new physics effects.

Another direction would be to search for more experimentally-friendly observables that distinguish between the different natures of the possible resonances. To make fully use of the three-step analysis proposed here it is mandatory that most of the event can be reconstructed. It might be possible to look for angles or other observables that are defined in the laboratory frame that are experimentally more appealing and give a better precision when all sources of contamination (like from extra radiation, underlying event, miss-identification, etc.) are taken into account. One of such contaminations for particular interest to heavy BSM resonances is the problem that the decay products of fast-moving top quarks will be very collimated, which leads to problems in identifying the top quarks, and distinguishing them from "normal" QCD jets.

In the context of the NLO single top production in the four flavor scheme presented in this thesis there are various improvements possible. Although we have gained some insights in the (none-)importance of resumming logarithms due to initial state gluon splitting to heavy quarks in the context of t-channel single top production, it must be stressed that the issue is not yet settled in general. Other processes with heavy quarks in the initial state that can be described in fixed or variable flavor number schemes could help in the understanding of the best treatment of the possibly large logarithms to improve predictions.

From a more phenomenological point of view several technical improvements can be made. First, the inclusion of the decay of the top quark is an important next step. Including the decay allows for an easier comparison with experiment. In this perspective, matching this NLO computation to a parton shower, by including it in the `MC@NLO` or `POWHEG` frameworks would be the final goal of the

calculation as it stands now. Alternatively, the threshold logarithms could also be included analytically, possible up to NLL, to improve the predictions close to threshold. This last option is particularly interesting in the context of fourth generation heavy quark (t' and/or b') production, where the process is close to threshold due to limited availability of the phase space. Furthermore this calculation can be adapted and used to predict the rates and distributions for single top +1 jet production at NLO. This would also be one of the building blocks for the full next-to-next-to leading order (NNLO) corrections to the t-channel single top production mechanism.

Precise predictions are important for Tevatron and LHC phenomenology. An outstanding example is the acceptance for b quarks in t-channel single top events for which NLO computations are needed for a reliable prediction, as we have seen in Sec. 4.7.3. Automation of NLO computations, including matching to parton showers, is a very active field of research to which I am (and will be) contributing too. In the appendix of this thesis, a part of this automation, *i.e.*, the automation of the subtraction terms for the real emission of any NLO correction has been presented.

APPENDIX

A

AUTOMATION OF THE DIPOLE SUBTRACTION FOR NLO COMPUTATIONS

Physics studies at the upcoming CERN LHC collider will frequently involve multi-particle final states. Especially searches for physics beyond the standard model rely on the reconstruction of new particles from their decay products, often through decay chains. Equally, requiring accompanying particles in the final state may serve to improve the ratio of signal to background processes, as done for example in the Higgs boson search through the vector boson fusion channel. Meaningful searches for these signals require not only a very good anticipation of the expected signal, but also of all standard model backgrounds yielding identical final state signatures. From the theoretical point of view, high precision implies that one has to go beyond the leading order in perturbation theory to be able to keep up with the precision of the measurements.

For leading order processes there have been many developments concerning event generation and simulation tools in the last two decades such as `MadGraph/MadEvent` [93–95] `CompHEP/CalcHEP` [176]/ [177], `SHERPA` [178] and `WHIZARD` [179] and also programs using different approaches such as `ALPGEN` [180] and `HELAC` [181]. All these programs are multi-purpose event generator tools, which are able to compute any process (up to technical restrictions in the multiplicity) within the standard model, or within alternative theories specified by their interaction Lagrangian or Feynman rules. They usually provide event information which can be interfaced into parton shower, hadronization and/or detector simulation.

Next-to-leading order (NLO) calculations are at present performed on a process-by-process basis. The widely-used programs `MCFM` [96, 182], `NLOJET++` [183], `MC@NLO` [40, 184] and programs based on the `POWHEG` method [41, 185–189] collect a variety of different processes in a standardized framework, the latter two methods also matches the NLO calculation onto a parton shower.

The NLO QCD corrections to a given process with a n-parton final state receive two types of contributions: the one-loop virtual correction to the $(2 \to n)$-parton scattering process, and the real emission correction from all possible $(2 \to n+1)$-parton scattering processes. For the numerical evaluation, one has to be able to compute both types of contributions separately.

The computation of one-loop corrections to multi-particle scattering amplitudes was performed on a case-by-case basis up-to-now, the calculational complexity increased considerably with increasing number of external partons. Since only a limited number of one-loop integrals can appear [190, 191] in the final result, the calculation of one-loop corrections can be reformulated as determination of the coefficients of these basis integrals, plus potential rational terms. Enormous progress [192–211] has been made in the recent past in the systematic determination of the one-loop integral coefficients and rational terms, and steps towards fully automated programs for the calculation of one-loop multi-parton amplitudes were made with the packages `CutTools` [212], `BlackHat` [213], `Rocket` [214] and `GOLEM` [215].

The real emission corrections contain soft and collinear singularities, which become explicit only after integration over the appropriate real radiation phase space yielding a hard n-parton final state. They are canceled by the singularities from the virtual one-loop contributions, thus yielding a finite NLO correction. To systematically extract the real radiation singularities from arbitrary processes, a variety of methods, based either on phase-space slicing [157] or on the introduction of process-independent subtraction terms [158] have been proposed. Several different algorithms to derive subtraction terms are available: residue subtraction [159], dipole subtraction [160, 161] and antenna subtraction [162–165].

Especially the dipole subtraction formalism, which provides local subtraction terms for all possible initial and final state configurations [160] and allows to account for radiation off massive partons [161], is used very widely in NLO calculations. It has recently also been automated in the SHERPA framework [216] and the TeVJet framework [217], and most recently in the form of independent libraries [218] interfaced to `MadGraph`. The dipole subtraction within the SHERPA framework is not available as a stand-alone tool, while within the TeVJet framework, the user needs to provide all the necessary process de-

pendent information. Moreover both approaches have only included massless particles for the dipoles. There is still no general tool available which is able to produce the dipole terms for an arbitrary process and which can also deal with massive partons.

In this appendix we present `MadDipole`, an automatic generation of the dipole subtraction terms using the `MadGraph/MadEvent` framework. The results are `Fortran` subroutines which return the squared amplitude for all possible dipole configurations in the usual `MadGraph` style. We describe the construction of the dipole subtraction terms and their implementation in Section A.1. Results from various checks of the implementation are provided Section A.2.

A.1 Construction of dipole terms

Using the notation introduced in Refs. [160, 161] we can write, independently whether we have initial or final state particles, an arbitrary dipole in the form

$$\mathcal{D}_{ij,k} \sim {}_m\langle 1,\dots \tilde{ij},\dots,\tilde{k},\dots,m{+}1|\frac{\mathbf{T}_k\cdot\mathbf{T}_{ij}}{\mathbf{T}_{ij}^2}\mathbf{V}_{ij,k}|1,\dots \tilde{ij},\dots,\tilde{k},\dots,m{+}1\rangle_m. \tag{A.1}$$

The (Born) amplitude factors $\langle\dots|$ ('bra') and $|\dots\rangle$ ('ket') on the right hand side are tensors in color space. The helicities of the external particles in them are a priori fixed (but can be summed over for unpolarized processes), while the helicities of the pseudo-partons have to be summed over after contraction with the dipole splitting function. The two elements that combine the ket with the bra are the additional color structure $\frac{\mathbf{T}_k\cdot\mathbf{T}_{ij}}{\mathbf{T}_{ij}^2}$ and the dipole splitting function $\mathbf{V}_{ij,k}$.

These Born-level amplitude factors are provided by the usual `MadGraph` code.

A.1.1 Color and helicity management

For the calculation of the color factors there already exist routines in the `MadGraph` program. Our intention was to use exactly these routines because this code is very well-confirmed and efficient. We have included the additional color operator, $\mathbf{T}_k\cdot\mathbf{T}_{ij}$, by rewriting the internal `MadGraph` color labelling for the ket-side only. After insertion of this color operator the color structure is no longer multiplied by its own complex conjugate and therefore the routine that squares the color needed to be altered, to multiply the modified ket by its

original complex conjugate. We emphasize that due to the factorial growth of the color factors `MadGraph` can not handle more than seven colored particles.

For the insertion of the splitting function $\mathbf{V}_{ij,k}$ several changes with respect to the original code are required. One has to keep in mind that in general the splitting function is a tensor in helicity space, *i.e.*,

$$\mathbf{V}_{ij,k} \equiv \langle\mu|\mathbf{V}_{ij,k}|\nu\rangle = \mathbf{V}^{\mu\nu}_{ij,k}.$$

As `MadGraph` deals with helicity amplitudes, we have to write the dipole in a slightly different way to be able to include the calculation of the splitting function in the code. Neglecting the color for a moment we start from the definition of the dipole in (A.1) and by inserting a full set of helicity states $-g_{\mu\nu} = \sum_\lambda \epsilon^*_\mu(\lambda)\epsilon_\nu(\lambda)$ we get

$$\begin{aligned}
\mathcal{D}_{ij,k} \sim {}& {}_m\langle 1,\dots \tilde{ij},\dots,\tilde{k},\dots,m+1|_\mu \\
& \times \mathbf{V}^{\mu\nu}_{ij,k}\ {}_\nu|1,\dots \tilde{ij},\dots,\tilde{k},\dots,m+1\rangle_m \\
= {}& {}_m\langle 1,\dots \tilde{ij},\dots,\tilde{k},\dots,m+1|_{\mu'} \\
& \times \left(-g^{\mu'}_{\ \mu}\right) \mathbf{V}^{\mu\nu}_{ij,k} \left(-g_\nu^{\ \nu'}\right) {}_{\nu'}|1,\dots \tilde{ij},\dots,\tilde{k},\dots,m+1\rangle_m \\
= {}& \sum_{\lambda_a,\lambda_b} {}_m\langle\dots|_{\mu'}\ \epsilon^{*\mu'}(\lambda_b)\epsilon_\mu(\lambda_b)\mathbf{V}^{\mu\nu}_{ij,k}\ \epsilon^*_\nu(\lambda_a)\epsilon^{\nu'}(\lambda_a)\ {}_{\nu'}|\dots\rangle_m \\
= {}& \sum_{\lambda_a,\lambda_b} {}_m\langle\dots|_{\lambda_b}\ V(\lambda_b,\lambda_a)\ {}_{\lambda_a}|\dots\rangle_m
\end{aligned} \tag{A.2}$$

with $V(\lambda_b,\lambda_a) = \epsilon_\mu(\lambda_b)\ \mathbf{V}^{\mu\nu}_{ij,k}\ \epsilon^*_\nu(\lambda_a)$ and $\epsilon^\mu(\lambda)\ {}_\mu|\dots\rangle_m = {}_\lambda|\dots\rangle_m$.

The polarization vectors are calculated using the HELAS routines [219] already available in the `MadGraph` code. The parts that are diagonal in helicity space are trivial to calculate in that sense that one only has to multiply the `MadGraph` output for the squared amplitude for a given helicity combination with the splitting function. To calculate the off-diagonal helicity terms, the amplitude for each helicity combination is stored and then combined with the according amplitude with opposite helicity.

For the calculation of the splitting functions and for the remaping of the momenta we use modified versions of the routines used in `MCFM` [96, 182].

A.1.2 Massive particles

If some of the masses of the external particles are non-zero, in particular for processes involving top and/or bottom quarks, there are dipoles for which the

unresolved parton is massive. In this case the collinear/soft singularities are regulated by the mass of the unresolved parton and the unsubtracted matrix element does therefore no longer diverge in these collinear/soft limits, but only develops potentially large logarithms. Our code still calculates all possible dipoles, also in which the unresolved parton is massive, but puts them in a separate subroutine, `dipolsumfinite(...)`, that is not evaluated by default. In the limit of large center of momentum energy or, similarly, small external masses, the user can easily include the non-divergent dipoles to subtract the associated large logarithms, which can then be included analytically through the integrated subtraction terms. In the limit of zero external masses we have checked that the results obtained after summing all dipoles are the same as obtained by generating the code with massless particles from the start.

A.1.3 Phase space restriction

The calculation of the subtraction terms is only necessary in the vicinity of a soft and/or collinear limit. Away from these limits the amplitude is finite and there is in principal no need to calculate the computationally heavy subtraction terms. The distinction between regions near to a singularity from regions without need for a subtraction can be parametrized by the introduction of a parameter usually labelled α with $\alpha \in [0, 1]$, which was introduced in Ref. [220] for processes involving partons only in the final state. The case with incoming hadrons, *i.e.*, with partons in the initial state, is described in Ref. [183].

Using the notation of Ref. [183], the contribution from the subtraction term to the differential cross section can be written as

$$
\begin{aligned}
d\sigma^A_{ab} = \sum_{\{n+1\}} d\Gamma^{(n+1)}(p_a,p_b,p_1,\ldots,p_n+1)\frac{1}{S_{\{n+1\}}} \\
\times \Bigg\{ \sum_{\substack{\text{pairs}\\ i,j}} \sum_{k\neq i,j} \mathcal{D}_{ij,k}(p_a,p_b,p_1,\ldots,p_{n+1}) \\
\times F_J^{(n)}(p_a,p_b,p_1,\ldots,\tilde{p}_{ij},\tilde{p}_k,\ldots,p_{n+1})\Theta(y_{ij,k}<\alpha) \\
+ \sum_{\substack{\text{pairs}\\ i,j}} \Big[\mathcal{D}^a_{ij}(p_a,p_b,p_1,\ldots,p_{n+1}) \\
\times F_J^{(n)}(\tilde{p}_a,p_b,p_1,\ldots,\tilde{p}_{ij},\ldots,p_{n+1})\Theta(1-x_{ij,a}<\alpha) \\
+ (a\leftrightarrow b)\Big] \\
+ \sum_{i\neq k} \Big[\mathcal{D}^{ai}_{k}(p_a,p_b,p_1,\ldots,p_{n+1}) \\
\times F_J^{(n)}(\tilde{p}_a,p_b,p_1,\ldots,\tilde{p}_k,\ldots,p_{n+1})\Theta(u_i<\alpha) + (a\leftrightarrow b)\Big] \\
+ \sum_{i} \Big[\mathcal{D}^{ai,b}(p_a,p_b,p_1,\ldots,p_{n+1}) \\
\times F_J^{(n)}(\tilde{p}_a,p_b,\tilde{p}_1,\ldots,\tilde{p}_{n+1})\Theta(\tilde{v}_i<\alpha) + (a\leftrightarrow b)\Big] \Bigg\} \ .
\end{aligned}
\tag{A.3}
$$

The functions $\mathcal{D}_{ij,k}$, $\mathcal{D}^a_{ij}$, $\mathcal{D}^{ai}_k$ and $\mathcal{D}^{ai,b}$ are the dipole terms for the various combinations for emitter and spectator. $\sum_{\{n+1\}}$ denotes the summation over all possible configurations for this $(n+1)$-particle phase space which is labelled as $d\Gamma^{(n+1)}$ and the factor $S_{\{n+1\}}$ is the symmetry factor for identical particles. We have introduced four different α-parameters, one for each type of dipoles. In our code they are called `alpha_ff`, `alpha_fi`, `alpha_if` and `alpha_ii` for the final-final, finial-initial, initial-final and initial-initial dipoles, respectively. The actual values for these parameters are by default set to unity, corresponding to the original formulation of the dipole subtraction method [160, 161], but can be changed by the user in the file `dipolsum.f`.

It has to be kept in mind that the integrated dipole factors, which are to be added with the virtual n-parton contribution, will also depend on α. For case of massless partons, the α-dependence of the integrated terms is stated

in [183, 220] while for massive partons results for most cases can be found in [49, 55].

A.2 Checks

The `MadDipole` package provides a code, `check_dip.f`, which allows the user to test the limits of the $(n+1)$-particle matrix element and the dipole subtraction terms. This code builds up a trajectory of randomly selected phase space point approaching a given soft or collinear limit of the $(n+1)$-parton matrix element and yields the values of matrix element, sum of all the dipoles, and their ratio along this trajectory. The result is printed to the screen in a small table for which each successive row is closer to the singularity. The ratio between matrix element and the sum of the dipoles should go to unity. We have tested our code in all possible limits, both for massless as well as massive dipoles and found no inconsistencies. Choosing small values for α-parameters, *e.g.*, $\alpha = 0.1$, improves the computation time and the convergence of the subtraction procedure.

To show that the subtraction terms are implemented correctly we provide a couple of examples in the form of plots and argue that the cancellation between the matrix element squared and the subtraction term is as expected. In the Figs. A.1, A.2, A.3 and A.4 we show the matrix element squared and the subtraction term as a function of a variable that represents a soft and/or collinear limit of the process specified. For these figures we have binned the x-axis (equally sized bins for the logarithmic scale) and generated random points in phase space to fill each of the bins with exactly 100 events. In the upper plot, $|M_R|^2$ and D are the per bin averages of the matrix element squared and the subtraction term, respectively. The second to upper plot shows the per bin average of the ratio of the matrix element squared and the subtraction term, while the third plot from the top shows the per bin average of the difference. The lowest plot shows the absolute value of the maximal difference among the 100 points in a bin. To show the effects of the phase space restriction for the dipoles, see Sec. A.1.3, all the plots are given for $\alpha = 1$ (dashed lines), $\alpha = 0.1$ (dotted lines) and $\alpha = 0.01$ (dot-dashed lines).

In Fig. A.1 we show the matrix element squared and the subtraction term as a function of $1 - x_{\bar{q}}$, where $x_{\bar{q}}$ is the fraction of the energy carried by the anti-quark, $x_{\bar{q}} = \frac{s_{34}+s_{45}}{s_{12}} = 1 - \frac{s_{35}}{s_{12}}$, with $s_{ij} = p_i.p_j$. For this process, $e^+(p_1)e^-(p_2) \to Z \to q(p_3)\bar{q}(p_4)g(p_5)$, there are only final-final state dipoles contributing to the subtraction term. The center of mass energy is set equal to the Z boson mass $\sqrt{s} = m_Z$. To restrict the discussion to the collinear

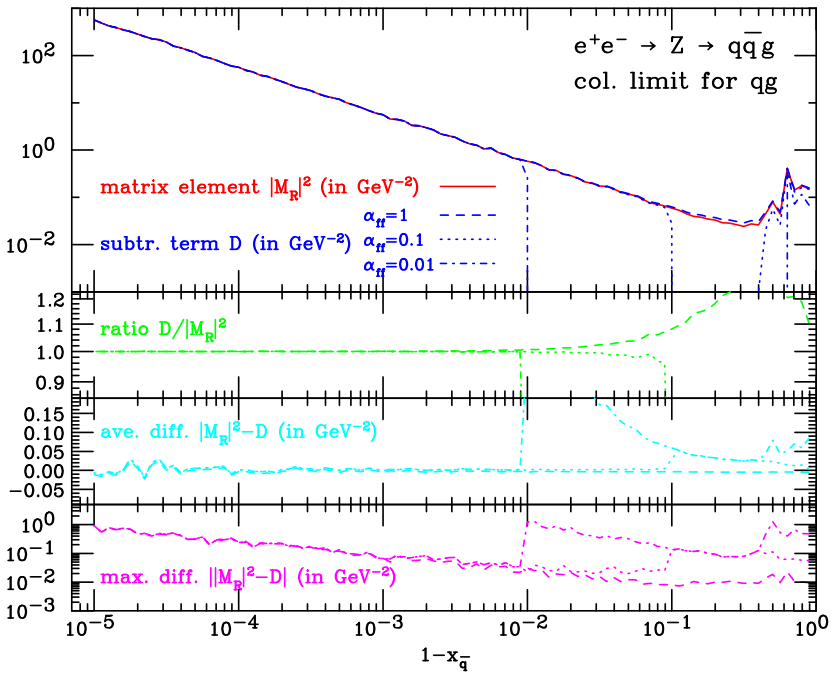

(a)

Figure A.1: Matrix element squared $|M_R|^2$ (upper plots, solid line) and the subtraction terms D (upper plots, dashed/dotted/dot-dashed lines) for the process $e^+(p_1)e^-(p_2) \to Z \to q(p_3)\bar{q}(p_4)g(p_5)$ as a function of $1-x_{\bar{q}} = (p_3.p_5)/(p_1.p_2)$. Also plotted are the ratio $D/|M_R|^2$, the difference $|M_R|^2-D$ (averaged over 100 random points per bin) and the maximal difference $\max(||M_R|^2 - D|)$ per bin. The dashed lines include the dipoles for each point in phase space, $\alpha_{ff} = 1$, while for the dotted $\alpha_{ff} = 0.1$ and dot-dashed $\alpha_{ff} = 0.01$ the phase space for the dipoles has been restricted to the collinear/soft regions.

divergence only, points close to the soft divergence ($x_{\bar{q}} = x_{\bar{q}} = 1$) have been removed by forcing $x_q + x_{\bar{q}} < 1.5$ in the generation of the phase space points.

From the upper plot it is clear that both the matrix element squared and the subtraction term diverge in the collinear limit $x_{\bar{q}} \to 1$, as $1/x_{\bar{q}}$. The ratio $D/|M_R|^2$ goes to 1 and the average values of the differences fluctuate close to 0 as can be seen in the second and third plots from the top. The numerical fluctuations for small $1-x_{\bar{q}}$ can be completely explained by statistical fluctuations. They are of the order of 1% of the maximal difference given in the lower plot. As can be expected, the cancellations are not exact, which is shown by the lower plot. The maximal difference between $|M_R|^2$ and D rises like

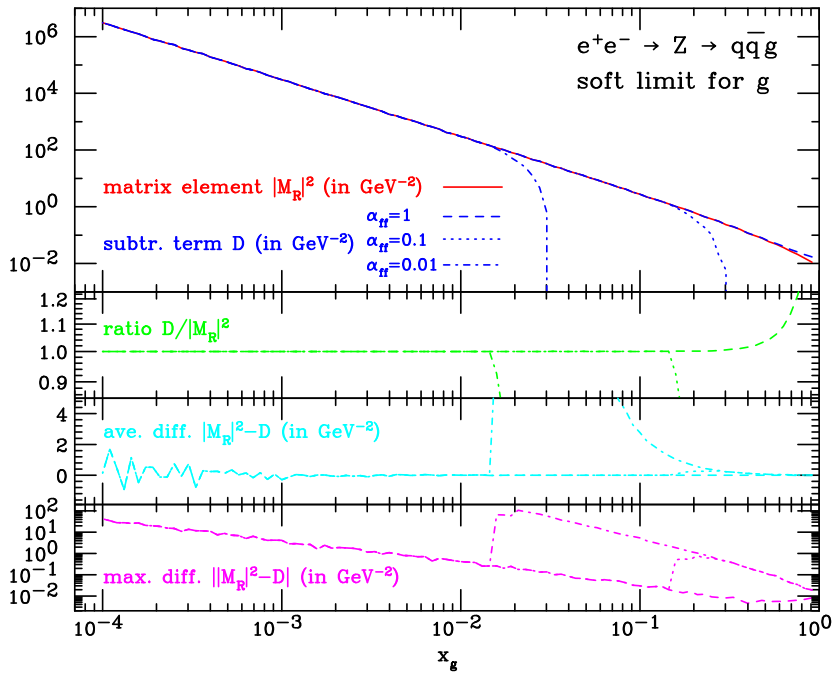

(a)

Figure A.2: Matrix element squared $|M_R|^2$ (upper plots, solid line) and the subtraction terms D (upper plots, dashed/dotted/dot-dashed lines) for the process $e^+(p_1)e^-(p_2) \to Z \to q(p_3)\bar{q}(p_4)g(p_5)$ as a function of $x_g = 1-(p_3.p_4)/(p_1.p_2)$. Also plotted are the ratio $D/|M_R|^2$, the difference $|M_R|^2-D$ (averaged over 100 random points per bin) and the maximal difference $\max(||M_R|^2 - D|)$ per bin. The dashed lines include the dipoles for each point in phase space, $\alpha_{ff} = 1$, while for the dotted $\alpha_{ff} = 0.1$ and dot-dashed $\alpha_{ff} = 0.01$ the phase space for the dipoles has been restricted to the collinear/soft regions.

$1/\sqrt{1-x_{\bar{q}}}$, which does not lead to a divergent phase space integral, because the integration measure is proportional to $x_{\bar{q}}$. The small peaks/fluctuations in the region for small $x_{\bar{q}}$ are due to the fact that we are approaching the other collinear limit, *i.e.*, for which the gluon is collinear to the anti-quark $x_q \to 1$, where the matrix elements squared and the subtraction term also diverge.

In Fig. A.2 the same matrix elements and subtraction terms are presented, but as a function of the fraction of the energy carried away by the gluon $x_g = 2 - x_q - x_{\bar{q}}$. The limit for which x_g goes to zero represents the soft divergence of this process, while the collinear divergences for this process are removed by excluding phase space points for which $x_{\bar{q}} > (1+x_q)/2$ or $x_q > (1+x_{\bar{q}})/2$.

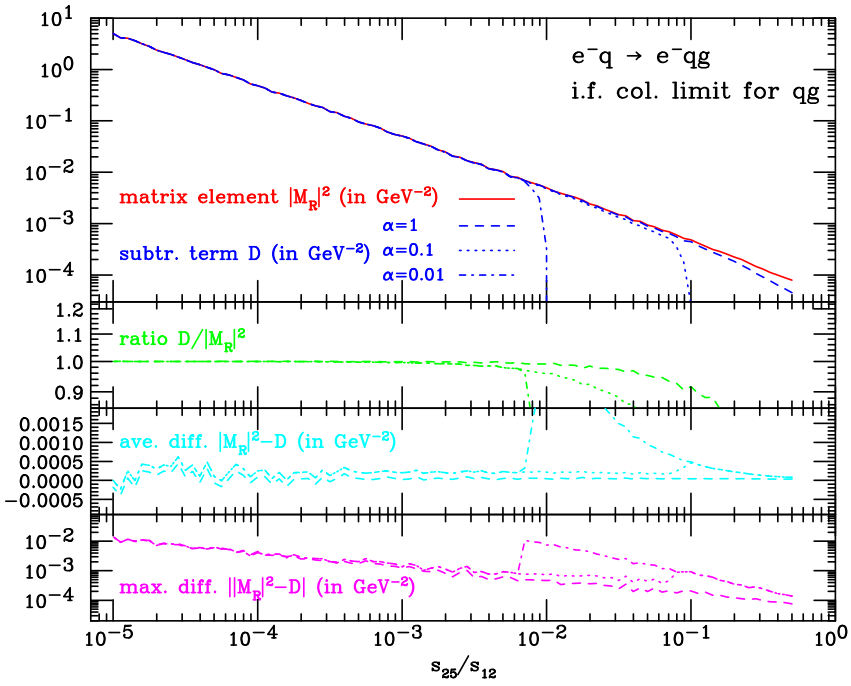

(a)

Figure A.3: Matrix element squared $|M_R|^2$ (upper plots, solid line) and the subtraction term D (upper plots, dashed/dotted/dot-dashed lines) for the process $e^-(p_1)q(p_2) \to e^-(p_3)q(p_4)g(p_5)$ as a function of $s_{25}/s_{12} = (p_2.p_5)/(p_1.p_2)$. Also plotted are the ratio $D/|M_R|^2$, the difference $|M_R|^2 - D$ (averaged over 100 random points per bin) and the maximal difference $\max(||M_R|^2 - D|)$ per bin. The dashed lines include the dipoles for each point in phase space, $\alpha = 1$, while for the dotted $\alpha = 0.1$ and dot-dashed $\alpha = 0.01$ the phase space for the dipoles has been restricted to the collinear/soft regions.

The same conclusion as for Fig. A.1 can be drawn here: the matrix element squared and the subtraction term diverge in the soft limit, their ratio goes to one and the average difference to zero, while the absolute value of the maximal difference still rises when approaching the soft limit, but does not lead to a divergent phase space integral.

An example for a collinear limit between final state and initial state particles is given in Fig. A.3. In this plot the matrix element squared and the subtraction term for the process $e^-(p_1)q(p_2) \to e^-(p_3)q(p_4)g(p_5)$ are given as a function of the invariant mass of the initial state quark and the final state gluon s_{25}/s_{12}. As this invariant mass goes to zero, the matrix element squared and the subtraction

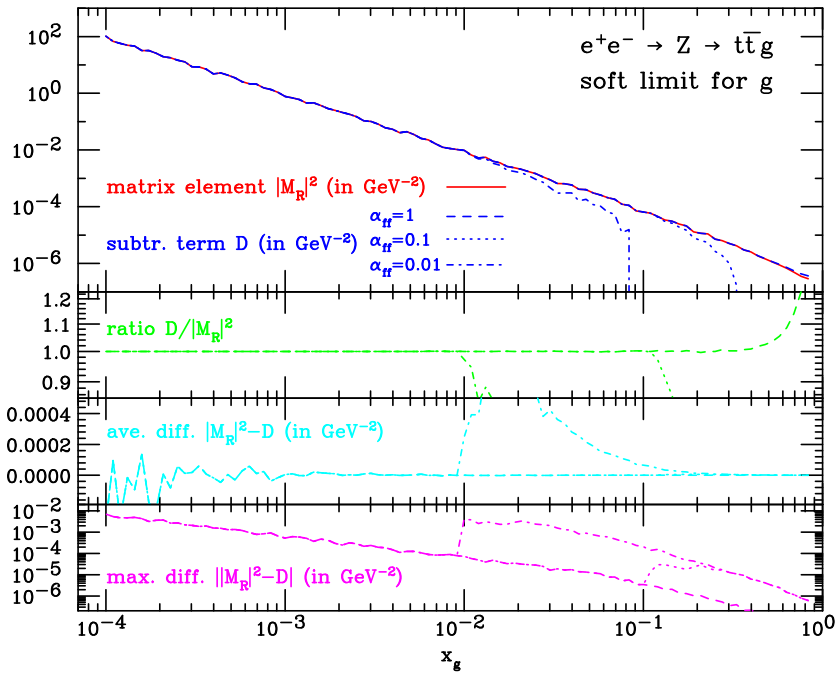

(a)

Figure A.4: Matrix element squared $|M_R|^2$ (upper plots, solid line) and the subtraction term D (upper plots, dashed/dotted/dot-dashed lines) for the process $e^+(p_1)e^-(p_2) \to Z \to t(p_3)\bar{t}(p_4)g(p_5)$ as a function of $x_g = 1 - (p_3.p_4)/(p_1.p_2)$. Also plotted are the ratio $D/|M_R|^2$, the difference $|M_R|^2 - D$ (averaged over 100 random points per bin) and the maximal difference $\max(||M_R|^2 - D|)$ per bin. The dashed lines include the dipoles for each point in phase space, $\alpha = 1$, while for the dotted $\alpha = 0.1$ and dot-dashed $\alpha = 0.01$ the phase space for the dipoles has been restricted to the collinear/soft regions.

term diverge like $1/s_{25}$, and their ratio goes to one. To remove the other possible divergences a cut on the momentum transferred $s_{13}/s_{12} > 0.5$ and on the invariant mass of the final state quark and gluon $s_{45}/s_{12} > 0.2$ have been imposed. Like for the final-final state dipoles the average difference goes to a constant, as can be seen from the second plot from the bottom, but the dipoles have a sizable constant contribution. Therefore the normalization of the average value for the difference $|M_R|^2 - D$ depends on the number of dipoles included for the phase space point. If all the dipoles are included for all points the difference goes to a smaller constant than if we restrict the phase space of the subtraction term to be close to the singularities by setting $\alpha < 1$. Due to

this restriction only the dipoles to cancel that divergence are included in the subtraction term and therefore give a smaller constant contribution, hence the difference $|M_R|^2 - D$ is larger. Also here the maximal left-over difference, the lowest plot, increases for small invariant masses but does not lead to a divergent phase space integral.

In Fig. A.4 an example with massive final state particles is shown. The process is $t\bar{t}$ production at a linear collider, $e^+(p_1)e^-(p_2) \to t(p_3)\bar{t}(p_4)g(p_5)$ at 1 TeV center of mass energy. The plot shows a behavior very similar to the massless case, Figs. A.1 and A.2, and the conclusions drawn there apply to this plot as well.

As a further check we have tested the code extensively against `MCFM` [96, 182]. We have generated random points in phase space and compared the subtraction terms calculated by `MCFM` with the subtraction terms calculated by our code. See Table A.1 for a list of processes that have been checked. We observed

process	subprocesses
Drell-Yan (W)	$q\bar{q}' \to W^+(\to e^+\nu_e)g$ $qg \to W^+(\to e^+\nu_e)q'$
Drell-Yan (Z)	$q\bar{q} \to Z(\to e^+e^-)g$ $qg \to Z(\to e^+e^-)q$
Drell-Yan (Z+jet)	$q\bar{q} \to Z(\to e^+e^-)q'\bar{q}'$ $q\bar{q} \to Z(\to e^+e^-)q\bar{q}$ $q\bar{q} \to Z(\to e^+e^-)gg$ $q\bar{g} \to Z(\to e^+e^-)qg$ $g\bar{g} \to Z(\to e^+e^-)q\bar{q}$
top quark pair ($t\bar{t}$)	$q\bar{q} \to t(\to bl^+\nu_l)\bar{t}(\to \bar{b}l^-\bar{\nu}_l)g$ $qg \to t(\to bl^+\nu_l)\bar{t}(\to \bar{b}l^-\bar{\nu}_l)q$ $gg \to t(\to bl^+\nu_l)\bar{t}(\to \bar{b}l^-\bar{\nu}_l)g$
t-channel single top with massive b-quark ($t\bar{b}q$) [59]	$gg \to t\bar{b}q\bar{q}'$ $qq' \to t\bar{b}q'q''$ $qq' \to t\bar{b}q'q''$ $qg \to t\bar{b}q'g$

Table A.1: Set of processes for which the `MadDipole` code has been tested against `MCFM` for random points in phase space. All the possible initial-initial, initial-final and final-initial, dipoles for massless and massive final state particles have been checked with this set of subprocesses. No inconsistencies were found.

differences only in the case where dipoles were introduced entirely to cancel collinear limits, which can be made independently of the spectator particle. In our code all possible dipoles are calculated, which implies a sum over all spectator particles. However, if there is only a collinear divergence, *i.e.*, the unresolved parton cannot go soft, this sum is redundant and one dipole with the appropriate coefficient is enough to cancel the singularity. In `MCFM`, these special limits are implemented using a single spectator momentum, while `MadDipole` sums over all spectator momenta, thereby yielding a different subtraction term. We have checked in the relevant cases that close to the singularities the `MCFM` subtraction terms behave identical to the subtraction terms calculated by our code.

We also tested the CPU time which is needed to produce the squared matrix element and the dipoles for a given phase space point. These checks were performed with an Intel Pentium 4 processor with 3.20Ghz. As an example we picked out three different processes:

1) $gg \to gggg$: $|\mathcal{M}|^2$: 26ms, $\sum_{\text{dipoles}}$: 68ms

2) $u\bar{u} \to d\bar{d}ggg$: $|\mathcal{M}|^2$: 10ms, $\sum_{\text{dipoles}}$: 45ms

3) $u\bar{u} \to u\bar{u}ggg$: $|\mathcal{M}|^2$: 34ms, $\sum_{\text{dipoles}}$: 0.15s

The time which is needed to produce the `FORTRAN` code is strongly dependent on the process and ranges from a few seconds to at most a few minutes. The process $gg \to 5g$ is currently not yet feasible within `MadGraph` because of the size of the color factors. Once `MadGraph` has been adjusted to handle this process, it will equally become accessible for `MadDipole`.

A.3 Conclusions

In this appendix we have presented `MadDipole`, an implementation to fully automate the calculation of the dipole subtraction formalism for massless and massive partons in the `MadGraph/MadEvent` framework. The implementation is done in such a way that the user only needs to specify the desired $(n+1)$-particle process and our code returns a FORTRAN code for all dipoles combined with possible Born processes which can lead to the $(n+1)$ process specified by the user.

For the calculation of the new color factors we have used as far as possible the routines already provided by the original `MadGraph` code. We inserted the two

additional operators for emitter and spectator and modified the evaluation of the squared color factors.

For the contributions that are not diagonal in helicity space we again used the already available routines for calculating amplitudes for a given helicity combination and combined amplitudes with different helicity combinations to yield the off-diagonal helicity contributions to the subtraction terms.

We have validated the code on numerous different processes with massive and massless partons using two checking procedures. The ratio of $\mathcal{M}^2_{n+1}/\sum_{\text{dipoles}}$ was confirmed to approach unity as one approaches any soft or collinear limit. The package includes a file `check_dip.f` which allows the user to reproduce this check for any process under consideration.

Secondly, we compared our code against the results of `MCFM` [96, 182], where subtraction is performed using the dipole formalism, finding point-wise agreement wherever anticipated. Differences with `MCFM` are understood to be due to different details in the implementation.

The `MadDipole` package allows the automated computation of real radiation dipole subtraction terms required for NLO calculations. Together with the fast developing automation of one-loop calculations of multi-leg processes, it could lead to a full automation of NLO calculations for collider processes. In view of the large number of potentially relevant multi-particle production processes at LHC, such automation will be crucial for precision phenomenology, in order to establish and interpret potential deviations from Standard Model expectations.

APPENDIX

B

PREDICTIONS FOR T-CHANNEL SINGLE TOP AND FOURTH GENERATION QUARKS

top mass (GeV)	$2 \to 2$ (fb)	$2 \to 3$ (fb)
164	(1059) $1127^{+27\ +106}_{-2\ -89}$	(790) $1080^{+88\ +96}_{-121\ -80}$
168	(985) $1052^{+23\ +102}_{-3\ -86}$	(729) $1006^{+83\ +93}_{-115\ -77}$
172	(917) $981^{+23\ +98}_{-3\ -82}$	(672) $935^{+82\ +88}_{-107\ -74}$
176	(854) $916^{+21\ +95}_{-2\ -79}$	(621) $872^{+76\ +85}_{-101\ -71}$
180	(796) $856^{+20\ +91}_{-3\ -76}$	(575) $812^{+74\ +82}_{-95\ -68}$
200	(561) $613^{+13\ +75}_{-2\ -62}$	(391) $575^{+58\ +66}_{-71\ -54}$
400	(23.7) $33.5^{+0.4\ +10.4}_{-0.3\ -8.0}$	(13.1) $27.9^{+4.9\ +7.9}_{-4.7\ -6.0}$
600	(1.24) $2.57^{+0.05\ +1.38}_{-0.07\ -0.99}$	(0.59) $1.88^{+0.45\ +0.90}_{-0.39\ -0.64}$
800	(0.064) $0.202^{+0.009\ +0.155}_{-0.010\ -0.107}$	(0.026) $0.126^{+0.039\ +0.088}_{-0.031\ -0.060}$
1000	(0.003) $0.013^{+0.001\ +0.013}_{-0.001\ -0.008}$	(0.001) $0.007^{+0.002\ +0.006}_{-0.002\ -0.004}$

Table B.1: NLO cross sections (fb) at the Tevatron Run II for top quark production in the t channel, as a function of the top mass obtained with the CTEQ6.6 PDF set and $V_{t^{(\prime)}b} = 1$. In the second (third) column the $2 \to 2$ ($2 \to 3$) results are shown, where the first uncertainty comes from renormalisation and factorisation scales variation and the second from PDF errors. Numbers in parenthesis refer to the corresponding LO results. Cross sections for anti-top are the same and are not displayed. These results are plotted in Fig. 4.12 where the scale and PDF uncertainties are combined linearly.

top mass (GeV)	$2 \to 2$ (fb)	$2 \to 3$ (fb)
164	(1211) $1145^{+28\ +66}_{-2\ -57}$	(893) $1089^{+94\ +58}_{-127\ -47}$
168	(1131) $1067^{+27\ +63}_{-2\ -54}$	(827) $1013^{+88\ +56}_{-122\ -45}$
172	(1056) $994^{+24\ +61}_{-2\ -52}$	(764) $942^{+86\ +53}_{-113\ -43}$
176	(987) $928^{+23\ +58}_{-3\ -50}$	(707) $876^{+80\ +51}_{-107\ -41}$
180	(922) $866^{+21\ +56}_{-3\ -47}$	(655) $816^{+75\ +49}_{-100\ -39}$
200	(661) $618^{+14\ +45}_{-3\ -38}$	(450) $574^{+61\ +39}_{-74\ -31}$
400	(33.0) $30.0^{+0.4\ +5.1}_{-0.3\ -4.0}$	(16.6) $24.9^{+4.7\ +3.7}_{-4.4\ -2.8}$
600	(2.032) $1.811^{+0.040\ +0.512}_{-0.060\ -0.389}$	(0.813) $1.352^{+0.342\ +0.323}_{-0.290\ -0.235}$
800	(0.116) $0.100^{+0.005\ +0.042}_{-0.005\ -0.030}$	(0.038) $0.067^{+0.022\ +0.023}_{-0.016\ -0.016}$
1000	(0.005) $0.004^{+0.001\ +0.002}_{-0.000\ -0.002}$	(0.001) $0.003^{+0.000\ +0.001}_{-0.001\ -0.001}$

Table B.2: Same as Table B.1 but for the MSTW2008 PDF set.

top mass (GeV)		$2 \to 2$ (pb)	$2 \to 3$ (pb)
164	t	(80.9) $89.5^{+1.5\ +1.7}_{-1.1\ -1.8}$	(80.9) $86.0^{+2.6\ +1.6}_{-3.8\ -1.7}$
	$\bar{t}$	(44.1) $50.2^{+0.8\ +1.1}_{-0.5\ -1.2}$	(43.3) $47.7^{+1.4\ +1.9}_{-2.0\ -2.2}$
168	t	(78.2) $86.4^{+1.6\ +1.6}_{-1.0\ -1.8}$	(77.7) $83.0^{+2.4\ +1.5}_{-3.9\ -1.6}$
	$\bar{t}$	(42.6) $48.4^{+0.7\ +1.0}_{-0.6\ -1.2}$	(41.6) $46.0^{+1.2\ +1.0}_{-2.1\ -1.1}$
172	t	(75.6) $83.5^{+1.4\ +1.5}_{-1.1\ -1.7}$	(74.8) $79.8^{+2.9\ +1.4}_{-3.4\ -1.6}$
	$\bar{t}$	(41.1) $46.6^{+0.8\ +1.0}_{-0.5\ -1.1}$	(39.8) $44.2^{+1.2\ +1.0}_{-2.0\ -1.1}$
176	t	(73.1) $80.6^{+1.4\ +1.5}_{-0.9\ -1.6}$	(71.9) $77.2^{+2.6\ +1.4}_{-3.8\ -1.5}$
	$\bar{t}$	(39.7) $44.9^{+0.7\ +1.0}_{-0.5\ -1.1}$	(38.3) $42.4^{+1.3\ +0.9}_{-1.9\ -1.1}$
180	t	(70.8) $77.9^{+1.3\ +1.4}_{-0.8\ -1.6}$	(68.8) $74.6^{+2.3\ +1.4}_{-3.7\ -1.4}$
	$\bar{t}$	(38.3) $43.3^{+0.8\ +0.9}_{-0.4\ -1.1}$	(36.6) $40.9^{+1.5\ +0.9}_{-1.8\ -1.0}$
200	t	(60.1) $66.1^{+1.1\ +1.2}_{-0.7\ -1.3}$	(57.1) $62.6^{+2.6\ +1.2}_{-3.1\ -1.2}$
	$\bar{t}$	(32.3) $36.4^{+0.6\ +0.8}_{-0.3\ -0.9}$	(30.0) $33.8^{+1.5\ +0.8}_{-1.4\ -0.9}$
400	t	(15.86) $17.65^{+0.24\ +0.53}_{-0.08\ -0.52}$	(12.65) $16.13^{+0.93\ +0.49}_{-1.21\ -0.47}$
	$\bar{t}$	(7.87) $8.99^{+0.13\ +0.41}_{-0.04\ -0.43}$	(6.13) $8.01^{+0.50\ +0.39}_{-0.56\ -0.40}$
600	t	(5.65) $6.46^{+0.07\ +0.35}_{-0.03\ -0.31}$	(4.09) $5.68^{+0.46\ +0.31}_{-0.50\ -0.27}$
	$\bar{t}$	(2.62) $3.10^{+0.04\ +0.23}_{-0.01\ -0.23}$	(1.84) $2.66^{+0.20\ +0.21}_{-0.24\ -0.20}$
800	t	(2.35) $2.77^{+0.03\ +0.23}_{-0.02\ -0.19}$	(1.58) $2.39^{+0.22\ +0.19}_{-0.25\ -0.16}$
	$\bar{t}$	(1.025) $1.263^{+0.012\ +0.138}_{-0.009\ -0.127}$	(0.672) $1.053^{+0.093\ +0.116}_{-0.104\ -0.106}$
1000	t	(1.071) $1.311^{+0.019\ +0.146}_{-0.012\ -0.121}$	(0.680) $1.093^{+0.121\ +0.118}_{-0.121\ -0.096}$
	$\bar{t}$	(0.442) $0.570^{+0.006\ +0.082}_{-0.005\ -0.073}$	(0.274) $0.462^{+0.043\ +0.066}_{-0.051\ -0.059}$
1200	t	(0.518) $0.660^{+0.010\ +0.095}_{-0.006\ -0.077}$	(0.315) $0.537^{+0.068\ +0.073}_{-0.062\ -0.059}$
	$\bar{t}$	(0.203) $0.275^{+0.004\ +0.050}_{-0.003\ -0.043}$	(0.120) $0.217^{+0.026\ +0.038}_{-0.026\ -0.033}$
1400	t	(0.262) $0.348^{+0.006\ +0.062}_{-0.005\ -0.049}$	(0.153) $0.276^{+0.037\ +0.045}_{-0.033\ -0.036}$
	$\bar{t}$	(0.097) $0.140^{+0.002\ +0.031}_{-0.002\ -0.026}$	(0.056) $0.108^{+0.013\ +0.023}_{-0.013\ -0.019}$
1600	t	(0.136) $0.190^{+0.004\ +0.041}_{-0.004\ -0.032}$	(0.077) $0.148^{+0.021\ +0.029}_{-0.020\ -0.022}$
	$\bar{t}$	(0.048) $0.074^{+0.001\ +0.019}_{-0.001\ -0.016}$	(0.027) $0.055^{+0.008\ +0.014}_{-0.007\ -0.011}$
1800	t	(0.072) $0.107^{+0.003\ +0.027}_{-0.002\ -0.021}$	(0.040) $0.081^{+0.012\ +0.018}_{-0.011\ -0.014}$
	$\bar{t}$	(0.025) $0.040^{+0.001\ +0.012}_{-0.001\ -0.010}$	(0.013) $0.029^{+0.004\ +0.008}_{-0.004\ -0.007}$
2000	t	(0.039) $0.061^{+0.002\ +0.018}_{-0.002\ -0.014}$	(0.021) $0.045^{+0.007\ +0.012}_{-0.006\ -0.009}$
	$\bar{t}$	(0.013) $0.022^{+0.001\ +0.008}_{-0.001\ -0.006}$	(0.007) $0.016^{+0.003\ +0.005}_{-0.002\ -0.004}$

Table B.3: NLO cross sections (pb) at the LHC 10 TeV for top and anti-top quarks production, as a function of the top mass obtained with the CTEQ6.6 PDF set and $V_{t^{(\prime)}b} = 1$. In the second (third) column the $2 \to 2$ ($2 \to 3$) results are shown, where the first uncertainty comes from renormalisation and factorisation scales variation and the second from PDF errors. Numbers in parenthesis refer to the corresponding LO results. These results are plotted in Fig. 4.13 where the scale and PDF uncertainties are combined linearly.

top mass (GeV)		$2 \to 2$ (pb)	$2 \to 3$ (pb)
164	t	(82.0) $90.4^{+1.6\ +1.2}_{-1.1\ -1.1}$	(82.3) $86.7^{+2.6\ +1.2}_{-4.0\ -1.0}$
	$\bar{t}$	(46.4) $52.1^{+0.9\ +0.8}_{-0.6\ -1.1}$	(45.8) $48.7^{+1.8\ +0.7}_{-1.8\ -1.0}$
168	t	(79.2) $87.3^{+1.6\ +1.1}_{-1.1\ -1.1}$	(79.1) $83.5^{+2.7\ +1.2}_{-4.0\ -1.0}$
	$\bar{t}$	(44.7) $50.2^{+0.9\ +0.8}_{-0.6\ -1.0}$	(43.8) $47.3^{+1.1\ +0.8}_{-2.2\ -1.0}$
172	t	(76.6) $84.4^{+1.4\ +1.1}_{-1.0\ -1.0}$	(76.0) $80.3^{+3.2\ +1.1}_{-3.7\ -0.9}$
	$\bar{t}$	(43.2) $48.3^{+0.8\ +0.7}_{-0.5\ -1.0}$	(42.0) $45.4^{+1.7\ +0.7}_{-2.1\ -0.9}$
176	t	(74.1) $81.6^{+1.4\ +1.1}_{-0.9\ -1.0}$	(73.1) $77.6^{+2.3\ +1.1}_{-3.4\ -0.9}$
	$\bar{t}$	(41.7) $46.6^{+0.8\ +0.7}_{-0.5\ -1.0}$	(40.3) $43.7^{+1.2\ +0.7}_{-1.9\ -0.9}$
180	t	(71.7) $78.8^{+1.4\ +1.0}_{-0.8\ -0.9}$	(70.3) $74.6^{+3.0\ +1.0}_{-3.2\ -0.9}$
	$\bar{t}$	(40.3) $45.0^{+0.7\ +0.7}_{-0.5\ -0.9}$	(38.6) $42.3^{+1.0\ +0.7}_{-2.2\ -0.9}$
200	t	(61.1) $67.0^{+1.1\ +0.9}_{-0.6\ -0.8}$	(58.2) $63.3^{+2.6\ +0.9}_{-3.2\ -0.7}$
	$\bar{t}$	(34.1) $37.8^{+0.6\ +0.6}_{-0.4\ -0.8}$	(31.7) $35.3^{+0.9\ +0.6}_{-1.7\ -0.8}$
400	t	(16.43) $18.02^{+0.22\ +0.38}_{-0.10\ -0.30}$	(13.02) $16.37^{+0.98\ +0.35}_{-1.31\ -0.26}$
	$\bar{t}$	(8.51) $9.33^{+0.13\ +0.29}_{-0.06\ -0.32}$	(6.55) $8.33^{+0.45\ +0.26}_{-0.65\ -0.28}$
600	t	(6.01) $6.60^{+0.08\ +0.23}_{-0.03\ -0.19}$	(4.27) $5.78^{+0.48\ +0.20}_{-0.53\ -0.15}$
	$\bar{t}$	(2.90) $3.19^{+0.04\ +0.15}_{-0.02\ -0.16}$	(1.99) $2.74^{+0.21\ +0.16}_{-0.26\ -0.16}$
800	t	(2.57) $2.82^{+0.03\ +0.14}_{-0.02\ -0.11}$	(1.68) $2.40^{+0.24\ +0.12}_{-0.25\ -0.09}$
	$\bar{t}$	(1.167) $1.281^{+0.012\ +0.084}_{-0.010\ -0.082}$	(0.734) $1.064^{+0.092\ +0.068}_{-0.114\ -0.064}$
1000	t	(1.207) $1.324^{+0.015\ +0.088}_{-0.014\ -0.070}$	(0.733) $1.091^{+0.127\ +0.069}_{-0.124\ -0.050}$
	$\bar{t}$	(0.516) $0.568^{+0.007\ +0.048}_{-0.005\ -0.045}$	(0.303) $0.453^{+0.052\ +0.037}_{-0.051\ -0.033}$
1200	t	(0.602) $0.658^{+0.011\ +0.055}_{-0.008\ -0.043}$	(0.344) $0.529^{+0.070\ +0.041}_{-0.066\ -0.030}$
	$\bar{t}$	(0.244) $0.268^{+0.004\ +0.028}_{-0.003\ -0.025}$	(0.134) $0.209^{+0.025\ +0.021}_{-0.027\ -0.018}$
1400	t	(0.314) $0.342^{+0.006\ +0.034}_{-0.006\ -0.027}$	(0.170) $0.268^{+0.039\ +0.024}_{-0.034\ -0.018}$
	$\bar{t}$	(0.120) $0.132^{+0.003\ +0.017}_{-0.002\ -0.015}$	(0.063) $0.100^{+0.014\ +0.012}_{-0.013\ -0.010}$
1600	t	(0.168) $0.183^{+0.004\ +0.022}_{-0.003\ -0.017}$	(0.086) $0.141^{+0.021\ +0.015}_{-0.020\ -0.011}$
	$\bar{t}$	(0.061) $0.068^{+0.001\ +0.010}_{-0.002\ -0.009}$	(0.030) $0.050^{+0.008\ +0.007}_{-0.007\ -0.006}$
1800	t	(0.092) $0.100^{+0.003\ +0.014}_{-0.002\ -0.011}$	(0.045) $0.075^{+0.013\ +0.009}_{-0.011\ -0.006}$
	$\bar{t}$	(0.032) $0.035^{+0.001\ +0.006}_{-0.001\ -0.005}$	(0.015) $0.025^{+0.004\ +0.004}_{-0.004\ -0.003}$
2000	t	(0.051) $0.056^{+0.002\ +0.009}_{-0.002\ -0.007}$	(0.024) $0.041^{+0.007\ +0.005}_{-0.006\ -0.004}$
	$\bar{t}$	(0.017) $0.019^{+0.001\ +0.004}_{-0.001\ -0.003}$	(0.008) $0.013^{+0.002\ +0.002}_{-0.002\ -0.002}$

Table B.4: Same as Table B.3 but for the MSTW2008 PDF set.

top mass (GeV)		$2 \to 2$ (pb)	$2 \to 3$ (pb)
164	t	(146.1) $163.2^{+2.8\ +3.2}_{-2.7\ -3.7}$	(152.3) $156.5^{+5.2\ +3.0}_{-5.9\ -3.4}$
	$\bar{t}$	(85.1) $97.3^{+1.7\ +1.9}_{-1.5\ -2.2}$	(86.7) $92.8^{+2.6\ +1.8}_{-3.6\ -2.0}$
168	t	(141.9) $158.2^{+2.7\ +3.1}_{-2.6\ -3.6}$	(146.7) $151.9^{+5.0\ +2.9}_{-5.7\ -3.3}$
	$\bar{t}$	(82.4) $94.1^{+1.6\ +1.9}_{-1.5\ -2.2}$	(83.4) $89.8^{+2.8\ +1.8}_{-3.6\ -2.0}$
172	t	(137.6) $152.9^{+3.0\ +3.0}_{-2.3\ -3.4}$	(141.8) $147.0^{+5.0\ +2.7}_{-5.7\ -3.1}$
	$\bar{t}$	(79.8) $91.1^{+1.5\ +1.8}_{-1.5\ -2.1}$	(80.5) $86.8^{+2.4\ +1.8}_{-3.7\ -2.0}$
176	t	(133.6) $148.5^{+2.6\ +2.9}_{-2.3\ -3.3}$	(136.8) $142.6^{+4.9\ +2.7}_{-5.6\ -3.0}$
	$\bar{t}$	(77.5) $88.1^{+1.5\ +1.7}_{-1.3\ -2.0}$	(77.8) $83.6^{+2.7\ +1.6}_{-3.0\ -1.8}$
180	t	(129.6) $144.0^{+2.5\ +2.8}_{-2.2\ -3.2}$	(131.6) $138.1^{+4.9\ +2.6}_{-5.3\ -2.9}$
	$\bar{t}$	(75.0) $85.3^{+1.5\ +1.7}_{-1.2\ -2.0}$	(74.6) $81.1^{+2.1\ +1.6}_{-3.6\ -1.8}$
200	t	(112.2) $124.2^{+2.2\ +2.3}_{-1.7\ -2.6}$	(111.1) $117.0^{+4.4\ +2.1}_{-3.8\ -2.4}$
	$\bar{t}$	(64.5) $72.9^{+1.3\ +1.5}_{-1.0\ -1.7}$	(62.4) $68.9^{+2.1\ +1.4}_{-2.8\ -1.6}$
400	t	(34.5) $38.3^{+0.5\ +0.8}_{-0.3\ -0.8}$	(28.9) $35.2^{+1.9\ +0.8}_{-2.0\ -0.8}$
	$\bar{t}$	(18.4) $20.9^{+0.3\ +0.6}_{-0.1\ -0.7}$	(15.1) $19.1^{+0.7\ +0.6}_{-1.3\ -0.6}$
600	t	(14.01) $15.92^{+0.17\ +0.53}_{-0.09\ -0.51}$	(10.71) $14.25^{+0.94\ +0.48}_{-1.18\ -0.46}$
	$\bar{t}$	(7.06) $8.20^{+0.10\ +0.41}_{-0.04\ -0.42}$	(5.25) $7.18^{+0.44\ +0.37}_{-0.56\ -0.38}$
800	t	(6.60) $7.66^{+0.08\ +0.39}_{-0.05\ -0.35}$	(4.71) $6.64^{+0.60\ +0.34}_{-0.55\ -0.30}$
	$\bar{t}$	(3.15) $3.77^{+0.04\ +0.27}_{-0.02\ -0.26}$	(2.19) $3.20^{+0.25\ +0.24}_{-0.26\ -0.23}$
1000	t	(3.40) $4.05^{+0.04\ +0.28}_{-0.04\ -0.24}$	(2.30) $3.43^{+0.33\ +0.24}_{-0.31\ -0.20}$
	$\bar{t}$	(1.546) $1.907^{+0.019\ +0.179}_{-0.014\ -0.169}$	(1.020) $1.585^{+0.129\ +0.152}_{-0.143\ -0.142}$
1200	t	(1.86) $2.27^{+0.03\ +0.21}_{-0.02\ -0.17}$	(1.21) $1.90^{+0.19\ +0.17}_{-0.19\ -0.14}$
	$\bar{t}$	(0.810) $1.033^{+0.009\ +0.123}_{-0.009\ -0.112}$	(0.513) $0.842^{+0.070\ +0.100}_{-0.086\ -0.091}$
1400	t	(1.064) $1.333^{+0.016\ +0.149}_{-0.016\ -0.123}$	(0.663) $1.090^{+0.124\ +0.118}_{-0.117\ -0.096}$
	$\bar{t}$	(0.444) $0.585^{+0.006\ +0.085}_{-0.006\ -0.075}$	(0.270) $0.470^{+0.043\ +0.067}_{-0.053\ -0.060}$
1600	t	(0.626) $0.807^{+0.012\ +0.109}_{-0.010\ -0.089}$	(0.378) $0.651^{+0.074\ +0.083}_{-0.077\ -0.067}$
	$\bar{t}$	(0.252) $0.343^{+0.006\ +0.059}_{-0.003\ -0.051}$	(0.149) $0.268^{+0.034\ +0.044}_{-0.031\ -0.039}$
1800	t	(0.378) $0.503^{+0.008\ +0.080}_{-0.008\ -0.064}$	(0.221) $0.396^{+0.051\ +0.059}_{-0.046\ -0.047}$
	$\bar{t}$	(0.146) $0.208^{+0.004\ +0.041}_{-0.003\ -0.035}$	(0.084) $0.159^{+0.020\ +0.030}_{-0.019\ -0.026}$
2000	t	(0.233) $0.319^{+0.007\ +0.059}_{-0.005\ -0.047}$	(0.133) $0.251^{+0.030\ +0.042}_{-0.033\ -0.033}$
	$\bar{t}$	(0.087) $0.128^{+0.002\ +0.029}_{-0.002\ -0.024}$	(0.049) $0.096^{+0.014\ +0.021}_{-0.012\ -0.018}$

Table B.5: NLO cross sections (pb) at the LHC 14 TeV for top and anti-top quarks production, as a function of the top mass obtained with the CTEQ6.6 PDF set and $V_{t^{(\prime)}b} = 1$. In the second (third) column the $2 \to 2$ ($2 \to 3$) results are shown, where the first uncertainty comes from renormalisation and factorisation scales variation and the second from PDF errors. Numbers in parenthesis refer to the corresponding LO results. These results are plotted in Fig. 4.14 where the scale and PDF uncertainties are combined linearly.

top mass (GeV)		$2 \to 2$ (pb)	$2 \to 3$ (pb)
164	t	(148.1) $164.1^{+3.1\ +2.4}_{-2.8\ -2.4}$	(155.1) $157.8^{+4.4\ +2.4}_{-6.9\ -2.3}$
	$\bar{t}$	(88.8) $100.6^{+1.7\ +1.3}_{-1.8\ -2.0}$	(91.4) $95.5^{+2.2\ +1.4}_{-4.1\ -1.9}$
168	t	(143.7) $159.3^{+2.6\ +2.3}_{-2.9\ -2.3}$	(149.1) $152.1^{+4.7\ +2.4}_{-5.9\ -2.2}$
	$\bar{t}$	(86.1) $97.3^{+1.7\ +1.3}_{-1.6\ -1.9}$	(87.6) $91.7^{+2.6\ +1.3}_{-3.5\ -1.8}$
172	t	(139.4) $154.3^{+2.9\ +2.2}_{-2.5\ -2.2}$	(143.9) $146.8^{+4.3\ +2.2}_{-5.0\ -2.1}$
	$\bar{t}$	(83.4) $94.2^{+1.6\ +1.2}_{-1.5\ -1.9}$	(84.6) $88.7^{+2.6\ +1.3}_{-3.0\ -1.8}$
176	t	(135.2) $149.6^{+2.6\ +2.1}_{-2.4\ -2.1}$	(138.9) $142.7^{+4.6\ +2.2}_{-6.1\ -2.0}$
	$\bar{t}$	(80.8) $91.1^{+1.6\ +1.2}_{-1.4\ -1.8}$	(81.4) $85.8^{+2.1\ +1.2}_{-3.5\ -1.7}$
180	t	(131.3) $145.2^{+2.5\ +2.0}_{-2.3\ -2.0}$	(134.1) $138.6^{+5.1\ +2.1}_{-5.6\ -1.9}$
	$\bar{t}$	(78.4) $88.2^{+1.6\ +1.2}_{-1.3\ -1.8}$	(78.5) $83.1^{+2.1\ +1.2}_{-3.4\ -1.6}$
200	t	(113.6) $125.5^{+2.0\ +1.7}_{-1.9\ -1.7}$	(112.8) $119.3^{+3.7\ +1.7}_{-5.4\ -1.6}$
	$\bar{t}$	(67.4) $75.5^{+1.2\ +1.0}_{-1.1\ -1.5}$	(65.5) $70.9^{+2.1\ +1.0}_{-3.1\ -1.4}$
400	t	(35.1) $38.9^{+0.5\ +0.6}_{-0.2\ -0.5}$	(29.5) $35.6^{+2.1\ +0.5}_{-2.1\ -0.4}$
	$\bar{t}$	(19.5) $21.7^{+0.3\ +0.5}_{-0.1\ -0.6}$	(15.9) $19.6^{+0.9\ +0.5}_{-1.3\ -0.5}$
600	t	(14.51) $16.22^{+0.19\ +0.38}_{-0.10\ -0.30}$	(11.01) $14.42^{+0.98\ +0.34}_{-1.15\ -0.25}$
	$\bar{t}$	(7.61) $8.49^{+0.11\ +0.28}_{-0.05\ -0.31}$	(5.58) $7.36^{+0.48\ +0.25}_{-0.58\ -0.26}$
800	t	(6.97) $7.81^{+0.08\ +0.26}_{-0.05\ -0.21}$	(4.91) $6.78^{+0.54\ +0.22}_{-0.64\ -0.17}$
	$\bar{t}$	(3.46) $3.88^{+0.04\ +0.17}_{-0.03\ -0.18}$	(2.34) $3.29^{+0.26\ +0.15}_{-0.31\ -0.15}$
1000	t	(3.66) $4.11^{+0.05\ +0.18}_{-0.03\ -0.15}$	(2.42) $3.50^{+0.31\ +0.15}_{-0.36\ -0.11}$
	$\bar{t}$	(1.732) $1.945^{+0.018\ +0.112}_{-0.015\ -0.111}$	(1.101) $1.604^{+0.158\ +0.092}_{-0.162\ -0.087}$
1200	t	(2.05) $2.30^{+0.03\ +0.13}_{-0.03\ -0.10}$	(1.28) $1.89^{+0.20\ +0.10}_{-0.20\ -0.07}$
	$\bar{t}$	(0.925) $1.040^{+0.011\ +0.074}_{-0.009\ -0.070}$	(0.556) $0.831^{+0.087\ +0.058}_{-0.088\ -0.053}$
1400	t	(1.192) $1.339^{+0.020\ +0.089}_{-0.014\ -0.071}$	(0.709) $1.088^{+0.123\ +0.068}_{-0.126\ -0.050}$
	$\bar{t}$	(0.516) $0.583^{+0.007\ +0.049}_{-0.007\ -0.046}$	(0.296) $0.458^{+0.051\ +0.037}_{-0.054\ -0.033}$
1600	t	(0.718) $0.806^{+0.014\ +0.063}_{-0.010\ -0.050}$	(0.409) $0.642^{+0.079\ +0.047}_{-0.078\ -0.033}$
	$\bar{t}$	(0.299) $0.337^{+0.005\ +0.033}_{-0.004\ -0.030}$	(0.164) $0.259^{+0.032\ +0.024}_{-0.030\ -0.021}$
1800	t	(0.443) $0.497^{+0.010\ +0.045}_{-0.008\ -0.035}$	(0.242) $0.389^{+0.050\ +0.032}_{-0.049\ -0.023}$
	$\bar{t}$	(0.177) $0.200^{+0.004\ +0.023}_{-0.003\ -0.020}$	(0.093) $0.151^{+0.019\ +0.016}_{-0.018\ -0.014}$
2000	t	(0.279) $0.312^{+0.007\ +0.032}_{-0.006\ -0.025}$	(0.147) $0.240^{+0.033\ +0.022}_{-0.031\ -0.016}$
	$\bar{t}$	(0.107) $0.121^{+0.003\ +0.016}_{-0.002\ -0.014}$	(0.054) $0.089^{+0.013\ +0.011}_{-0.012\ -0.009}$

Table B.6: Same as Table B.5 but for the MSTW2008 PDF set.

$m_{b'}$ (GeV)		cross section (fb)
200	$b'\bar{t}$	(9394) $9556^{+105\ +202}_{-317\ -203}$
	$\bar{b}'t$	(5211) $5334^{+41\ +173}_{-131\ -193}$
400	$b'\bar{t}$	(3256) $3607^{+82\ +132}_{-172\ -120}$
	$\bar{b}'t$	(1696) $1907^{+18\ +98}_{-89\ -102}$
600	$b'\bar{t}$	(1457) $1738^{+54\ +92}_{-105\ -79}$
	$\bar{b}'t$	(713) $863^{+17\ +64}_{-44\ -63}$
800	$b'\bar{t}$	(729) $920^{+41\ +64}_{-61\ -54}$
	$\bar{b}'t$	(338) $435^{+13\ +41}_{-27\ -39}$
1000	$b'\bar{t}$	(390) $518^{+29\ +46}_{-37\ -38}$
	$\bar{b}'t$	(172) $235^{+9\ +28}_{-18\ -26}$
1200	$b'\bar{t}$	(219) $307^{+16\ +32}_{-27\ -26}$
	$\bar{b}'t$	(92.0) $132.1^{+7.2\ +19.9}_{-10.7\ -18.3}$
1400	$b'\bar{t}$	(126.5) $184.6^{+13.6\ +23.2}_{-16.1\ -18.4}$
	$\bar{b}'t$	(51.1) $77.7^{+4.4\ +13.0}_{-7.0\ -11.7}$
1600	$b'\bar{t}$	(75.1) $114.4^{+9.5\ +16.5}_{-10.5\ -13.0}$
	$\bar{b}'t$	(29.2) $46.7^{+2.7\ +8.7}_{-4.6\ -7.5}$
1800	$b'\bar{t}$	(45.5) $72.5^{+6.7\ +11.9}_{-7.2\ -9.3}$
	$\bar{b}'t$	(17.0) $28.5^{+2.1\ +6.0}_{-2.8\ -5.1}$
2000	$b'\bar{t}$	(28.0) $46.8^{+3.9\ +8.5}_{-5.2\ -6.5}$
	$\bar{b}'t$	(10.10) $17.90^{+1.39\ +4.18}_{-1.95\ -3.52}$

Table B.7: NLO cross sections (fb) at the LHC 14 TeV for $b'\bar{t}$ and $\bar{b}'t$ as a function of $m_{b'}$ obtained with the CTEQ6.6 PDF set and $V_{tb'} = 1$. The first uncertainty comes from renormalisation and factorisation scales variation and the second from PDF errors. Numbers in parenthesis refer to the corresponding LO results. These results are plotted in Fig. 4.16 where the scale and PDF uncertainties are combined linearly.

$m_{b'}$ (GeV)		cross section (fb)
200	$b'\bar{t}$	(9719) $9797^{+121\ +160}_{-315\ -121}$
	$\bar{b}'t$	(5551) $5575^{+27\ +133}_{-121\ -142}$
400	$b'\bar{t}$	(3401) $3696^{+73\ +92}_{-184\ -64}$
	$\bar{b}'t$	(1820) $1959^{+49\ +66}_{-73\ -67}$
600	$b'\bar{t}$	(1537) $1771^{+66\ +60}_{-104\ -42}$
	$\bar{b}'t$	(772) $884^{+31\ +39}_{-41\ -38}$
800	$b'\bar{t}$	(777) $937^{+41\ +40}_{-65\ -28}$
	$\bar{b}'t$	(369) $441^{+15\ +24}_{-27\ -21}$
1000	$b'\bar{t}$	(421) $526^{+29\ +27}_{-43\ -20}$
	$\bar{b}'t$	(189) $235^{+11\ +16}_{-18\ -14}$
1200	$b'\bar{t}$	(238) $307^{+19\ +19}_{-28\ -13}$
	$\bar{b}'t$	(102.0) $131.4^{+7.7\ +10.4}_{-11.3\ -9.1}$
1400	$b'\bar{t}$	(139.1) $183.6^{+13.2\ +13.1}_{-16.8\ -9.1}$
	$\bar{b}'t$	(57.0) $75.0^{+5.7\ +6.9}_{-6.7\ -6.0}$
1600	$b'\bar{t}$	(83.4) $112.7^{+10.2\ +9.1}_{-11.0\ -6.3}$
	$\bar{b}'t$	(32.7) $44.1^{+3.1\ +4.5}_{-4.1\ -3.8}$
1800	$b'\bar{t}$	(51.0) $70.9^{+6.1\ +6.3}_{-7.8\ -4.4}$
	$\bar{b}'t$	(19.2) $26.4^{+2.7\ +3.0}_{-2.5\ -2.4}$
2000	$b'\bar{t}$	(31.7) $44.6^{+4.7\ +4.4}_{-4.9\ -3.0}$
	$\bar{b}'t$	(11.46) $16.23^{+1.56\ +2.08}_{-1.80\ -1.71}$

Table B.8: Same as Table B.7 but for the MSTW2008 PDF set.

$m_{t'}$ (GeV)		$m_{b'} = m_{t'}$	$m_{t'} - m_{b'}$=200 GeV	$m_{t'} - m_{b'}$=500 GeV
172	$t'\bar{b}'$	(11423) $11503^{+116\ +235}_{-359\ -240}$	–	–
	$\bar{t}'b'$	(6381) $6479^{+31\ +180}_{-150\ -205}$	–	–
200	$t'\bar{b}'$	(7777) $8011^{+110\ +183}_{-313\ -183}$	–	–
	$\bar{t}'b'$	(4239) $4391^{+24\ +155}_{-124\ -171}$	–	–
400	$t'\bar{b}'$	(992) $1147^{+27\ +64}_{-60\ -55}$	(2763) $3072^{+74\ +117}_{-134\ -106}$	–
	$\bar{t}'b'$	(470) $553^{+10\ +42}_{-29\ -41}$	(1370) $1547^{+15\ +86}_{-70\ -87}$	–
600	$t'\bar{b}'$	(219) $279^{+10\ +25}_{-19\ -21}$	(465) $565^{+21\ +41}_{-31\ -34}$	(2538) $3022^{+114\ +138}_{-179\ -122}$
	$\bar{t}'b'$	(93.7) $121.7^{+4.7\ +16.2}_{-6.3\ -15.6}$	(207.3) $258.2^{+6.3\ +25.7}_{-14.7\ -24.3}$	(1207.3) $1474.6^{+34.2\ +95.4}_{-82.6\ -94.9}$
800	$t'\bar{b}'$	(61.6) $85.5^{+4.1\ +10.9}_{-7.1\ -8.6}$	(116.1) $154.3^{+5.9\ +16.7}_{-11.2\ -13.5}$	(377.5) $479.3^{+19.6\ +39.0}_{-30.1\ -32.2}$
	$\bar{t}'b'$	(24.2) $34.6^{+1.3\ +5.8}_{-2.5\ -5.1}$	(47.3) $64.6^{+2.5\ +9.5}_{-4.5\ -8.5}$	(163.2) $213.2^{+7.1\ +23.2}_{-15.0\ -22.2}$
1000	$t'\bar{b}'$	(19.8) $29.7^{+1.8\ +4.9}_{-2.6\ -3.8}$	(34.9) $50.2^{+2.8\ +7.4}_{-4.3\ -5.8}$	(92.7) $126.7^{+7.1\ +15.0}_{-9.4\ -12.0}$
	$\bar{t}'b'$	(7.19) $11.26^{+0.66\ +2.44}_{-0.88\ -2.09}$	(13.15) $19.80^{+0.91\ +3.80}_{-1.59\ -3.29}$	(36.86) $52.55^{+1.43\ +8.20}_{-4.17\ -7.28}$
1200	$t'\bar{b}'$	(6.90) $11.21^{+0.80\ +2.32}_{-1.12\ -1.76}$	(11.69) $18.24^{+1.28\ +3.37}_{-1.69\ -2.57}$	(27.87) $41.23^{+2.51\ +6.49}_{-3.71\ -5.05}$
	$\bar{t}'b'$	(2.34) $4.08^{+0.24\ +1.08}_{-0.38\ -0.90}$	(4.09) $6.78^{+0.33\ +1.63}_{-0.62\ -1.37}$	(10.28) $16.05^{+0.60\ +3.26}_{-1.54\ -2.80}$
1400	$t'\bar{b}'$	(2.54) $4.47^{+0.38\ +1.12}_{-0.48\ -0.84}$	(4.19) $7.09^{+0.54\ +1.61}_{-0.72\ -1.21}$	(9.37) $14.91^{+1.17\ +2.93}_{-1.39\ -2.24}$
	$\bar{t}'b'$	(0.80) $1.54^{+0.10\ +0.49}_{-0.16\ -0.40}$	(1.37) $2.51^{+0.15\ +0.73}_{-0.26\ -0.60}$	(3.22) $5.44^{+0.39\ +1.42}_{-0.48\ -1.20}$
1600	$t'\bar{b}'$	(0.97) $1.86^{+0.16\ +0.54}_{-0.22\ -0.40}$	(1.57) $2.88^{+0.25\ +0.77}_{-0.31\ -0.57}$	(3.37) $5.83^{+0.47\ +1.38}_{-0.61\ -1.04}$
	$\bar{t}'b'$	(0.29) $0.61^{+0.05\ +0.23}_{-0.07\ -0.18}$	(0.48) $0.96^{+0.07\ +0.34}_{-0.10\ -0.27}$	(1.08) $2.03^{+0.14\ +0.61}_{-0.22\ -0.50}$
1800	$t'\bar{b}'$	(0.38) $0.79^{+0.08\ +0.27}_{-0.10\ -0.19}$	(0.61) $1.21^{+0.13\ +0.38}_{-0.14\ -0.28}$	(1.26) $2.37^{+0.21\ +0.66}_{-0.25\ -0.49}$
	$\bar{t}'b'$	(0.10) $0.24^{+0.03\ +0.11}_{-0.03\ -0.08}$	(0.17) $0.38^{+0.04\ +0.15}_{-0.04\ -0.12}$	(0.38) $0.78^{+0.07\ +0.28}_{-0.09\ -0.23}$
2000	$t'\bar{b}'$	(0.15) $0.34^{+0.04\ +0.13}_{-0.04\ -0.09}$	(0.24) $0.52^{+0.06\ +0.19}_{-0.07\ -0.14}$	(0.49) $0.99^{+0.10\ +0.33}_{-0.12\ -0.24}$
	$\bar{t}'b'$	(0.04) $0.10^{+0.01\ +0.05}_{-0.01\ -0.04}$	(0.06) $0.16^{+0.02\ +0.08}_{-0.02\ -0.06}$	(0.14) $0.31^{+0.03\ +0.13}_{-0.03\ -0.10}$

Table B.9: NLO cross sections (fb) at the LHC 14 TeV for $t'\bar{b}'$ and $\bar{t}'b'$ as a function of $m_{t'}$ obtained with the CTEQ6.6 PDF set and $V_{t'b'} = 1$. The first uncertainty comes from renormalisation and factorisation scales variation and the second from PDF errors. Numbers in parenthesis refer to the corresponding LO results. These results are plotted in Fig. 4.17 where the scale and PDF uncertainties are combined linearly.

$m_{t'}$ (GeV)		$m_{b'} = m_{t'}$	$m_{t'} - m_{b'}$=200 GeV	$m_{t'} - m_{b'}$=500 GeV
172	$t'\bar{b}'$	(11808) $11795^{+115\ +185}_{-369\ -140}$	–	–
	$\bar{t}'b'$	(6793) $6741^{+48\ +161}_{-173\ -172}$	–	–
200	$t'\bar{b}'$	(8058) $8220^{+76\ +143}_{-309\ -107}$	–	–
	$\bar{t}'b'$	(4522) $4584^{+29\ +115}_{-154\ -122}$	–	–
400	$t'\bar{b}'$	(1047) $1173^{+24\ +41}_{-69\ -28}$	(2887) $3149^{+58\ +81}_{-156\ -57}$	–
	$\bar{t}'b'$	(510) $570^{+5\ +28}_{-29\ -26}$	(1476) $1597^{+19\ +56}_{-65\ -57}$	–
600	$t'\bar{b}'$	(237) $280^{+11\ +15}_{-18\ -10}$	(497) $577^{+19\ +26}_{-39\ -17}$	(2660) $3105^{+111\ +92}_{-200\ -65}$
	$\bar{t}'b'$	(103.4) $121.7^{+4.6\ +8.6}_{-7.7\ -7.6}$	(227.2) $262.1^{+8.6\ +15.3}_{-16.0\ -14.1}$	(1306.1) $1514.7^{+49.9\ +61.7}_{-85.2\ -61.5}$
800	$t'\bar{b}'$	(67.9) $84.3^{+4.2\ +6.1}_{-7.2\ -4.1}$	(126.7) $154.6^{+6.2\ +9.7}_{-12.6\ -6.6}$	(405.1) $484.2^{+20.2\ +23.8}_{-34.0\ -16.3}$
	$\bar{t}'b'$	(27.1) $33.4^{+1.7\ +3.1}_{-2.6\ -2.7}$	(52.6) $63.7^{+2.4\ +5.2}_{-4.7\ -4.5}$	(179.5) $213.9^{+7.1\ +13.5}_{-13.5\ -12.3}$
1000	$t'\bar{b}'$	(22.2) $28.7^{+1.8\ +2.6}_{-2.7\ -1.8}$	(38.9) $49.0^{+3.2\ +4.0}_{-4.2\ -2.7}$	(101.7) $126.2^{+6.5\ +8.5}_{-10.4\ -5.8}$
	$\bar{t}'b'$	(8.15) $10.55^{+0.60\ +1.26}_{-1.03\ -1.04}$	(14.82) $18.71^{+0.96\ +1.96}_{-1.48\ -1.63}$	(41.13) $51.02^{+2.51\ +4.58}_{-3.98\ -3.95}$
1200	$t'\bar{b}'$	(7.90) $10.56^{+0.80\ +1.13}_{-1.11\ -0.76}$	(13.26) $17.38^{+1.25\ +1.71}_{-1.71\ -1.16}$	(31.18) $39.97^{+2.67\ +3.42}_{-3.61\ -2.33}$
	$\bar{t}'b'$	(2.67) $3.57^{+0.23\ +0.51}_{-0.37\ -0.41}$	(4.66) $6.12^{+0.39\ +0.79}_{-0.60\ -0.65}$	(11.61) $15.06^{+0.60\ +1.67}_{-1.52\ -1.39}$
1400	$t'\bar{b}'$	(2.95) $4.04^{+0.37\ +0.51}_{-0.45\ -0.35}$	(4.83) $6.53^{+0.57\ +0.76}_{-0.70\ -0.52}$	(10.66) $14.12^{+1.13\ +1.45}_{-1.37\ -0.99}$
	$\bar{t}'b'$	(0.93) $1.26^{+0.12\ +0.21}_{-0.13\ -0.17}$	(1.57) $2.13^{+0.19\ +0.33}_{-0.22\ -0.26}$	(3.67) $4.88^{+0.28\ +0.66}_{-0.50\ -0.54}$
1600	$t'\bar{b}'$	(1.14) $1.61^{+0.17\ +0.23}_{-0.19\ -0.16}$	(1.84) $2.55^{+0.26\ +0.34}_{-0.29\ -0.23}$	(3.89) $5.32^{+0.50\ +0.64}_{-0.60\ -0.44}$
	$\bar{t}'b'$	(0.33) $0.47^{+0.04\ +0.09}_{-0.06\ -0.07}$	(0.55) $0.77^{+0.08\ +0.14}_{-0.09\ -0.11}$	(1.24) $1.70^{+0.15\ +0.27}_{-0.20\ -0.22}$
1800	$t'\bar{b}'$	(0.45) $0.65^{+0.07\ +0.10}_{-0.08\ -0.07}$	(0.72) $1.02^{+0.11\ +0.15}_{-0.12\ -0.11}$	(1.48) $2.08^{+0.19\ +0.29}_{-0.26\ -0.20}$
	$\bar{t}'b'$	(0.12) $0.17^{+0.02\ +0.04}_{-0.02\ -0.03}$	(0.20) $0.28^{+0.03\ +0.06}_{-0.04\ -0.05}$	(0.44) $0.61^{+0.07\ +0.12}_{-0.07\ -0.09}$
2000	$t'\bar{b}'$	(0.18) $0.27^{+0.04\ +0.05}_{-0.04\ -0.03}$	(0.28) $0.42^{+0.05\ +0.07}_{-0.05\ -0.05}$	(0.58) $0.83^{+0.09\ +0.13}_{-0.11\ -0.09}$
	$\bar{t}'b'$	(0.04) $0.07^{+0.01\ +0.02}_{-0.01\ -0.01}$	(0.07) $0.11^{+0.01\ +0.03}_{-0.01\ -0.02}$	(0.16) $0.23^{+0.02\ +0.05}_{-0.03\ -0.04}$

Table B.10: Same as Table B.9 but for the MSTW2008 PDF set.

$m_{b'}$ (GeV)		$m_{b'} - m_{t'}$=200 GeV	$m_{b'} - m_{t'}$=500 GeV
400	$b'\bar{t}'$	(1394) $1568^{+10\ +87}_{-74\ -89}$	–
	$\bar{b}'t'$	(2712) $3012^{+65\ +116}_{-147\ -104}$	–
600	$b'\bar{t}'$	(209) $260^{+6\ +26}_{-16\ -24}$	–
	$\bar{b}'t'$	(462) $565^{+19\ +41}_{-36\ -34}$	–
800	$b'\bar{t}'$	(47.5) $65.2^{+2.3\ +9.4}_{-4.9\ -8.5}$	(165.5) $215.0^{+5.2\ +23.1}_{-14.0\ -21.3}$
	$\bar{b}'t'$	(115.6) $153.7^{+7.5\ +16.6}_{-10.8\ -13.4}$	(371.8) $472.6^{+19.6\ +38.7}_{-32.7\ -31.9}$
1000	$b'\bar{t}'$	(13.18) $19.79^{+1.00\ +3.78}_{-1.60\ -3.25}$	(37.17) $52.68^{+1.66\ +8.20}_{-3.98\ -7.26}$
	$\bar{b}'t'$	(34.8) $50.3^{+2.5\ +7.4}_{-4.3\ -5.8}$	(91.9) $125.6^{+6.6\ +15.0}_{-9.3\ -12.0}$
1200	$b'\bar{t}'$	(4.10) $6.76^{+0.39\ +1.63}_{-0.60\ -1.37}$	(10.33) $16.07^{+0.79\ +3.18}_{-1.34\ -2.70}$
	$\bar{b}'t'$	(11.67) $18.15^{+1.19\ +3.40}_{-1.64\ -2.60}$	(27.69) $40.97^{+2.60\ +6.37}_{-3.49\ -4.95}$
1400	$b'\bar{t}'$	(1.37) $2.48^{+0.18\ +0.94}_{-0.25\ -0.76}$	(3.23) $5.49^{+0.39\ +1.38}_{-0.50\ -1.15}$
	$\bar{b}'t'$	(4.18) $7.10^{+0.52\ +1.61}_{-0.74\ -1.21}$	(9.32) $14.85^{+1.14\ +2.93}_{-1.36\ -2.24}$
1600	$b'\bar{t}'$	(0.48) $0.96^{+0.08\ +0.34}_{-0.10\ -0.27}$	(1.08) $2.03^{+0.15\ +0.62}_{-0.20\ -0.51}$
	$\bar{b}'t'$	(1.57) $2.88^{+0.25\ +0.78}_{-0.32\ -0.57}$	(3.35) $5.80^{+0.49\ +1.38}_{-0.59\ -1.03}$
1800	$b'\bar{t}'$	(0.17) $0.39^{+0.03\ +0.16}_{-0.05\ -0.12}$	(0.38) $0.78^{+0.07\ +0.28}_{-0.09\ -0.23}$
	$\bar{b}'t'$	(0.61) $1.21^{+0.12\ +0.38}_{-0.14\ -0.28}$	(1.26) $2.37^{+0.22\ +0.67}_{-0.27\ -0.49}$
2000	$b'\bar{t}'$	(0.06) $0.16^{+0.02\ +0.07}_{-0.02\ -0.06}$	(0.14) $0.31^{+0.03\ +0.15}_{-0.04\ -0.13}$
	$\bar{b}'t'$	(0.24) $0.52^{+0.06\ +0.19}_{-0.07\ -0.14}$	(0.49) $0.99^{+0.10\ +0.33}_{-0.12\ -0.24}$

Table B.11: Cross sections (fb) at the LHC 14 TeV for $b'\bar{t}'$ and $\bar{b}'t'$ as a function of $m_{b'}$ obtained with the CTEQ6.6 PDF set and $V_{t'b'} = 1$. The first uncertainty comes from renormalisation and factorisation scales variation and the second from PDF errors. Numbers in parenthesis refer to the corresponding LO results. These results are plotted in Fig. 4.18 where the scale and PDF uncertainties are combined linearly.

$m_{b'}$ (GeV)		$m_{b'} - m_{t'}$=200 GeV	$m_{b'} - m_{t'}$=500 GeV
400	$b'\bar{t}'$	(1498) $1616^{+28\ +57}_{-58\ -58}$	–
	$\bar{b}'t'$	(2837) $3096^{+66\ +80}_{-160\ -56}$	–
600	$b'\bar{t}'$	(229) $265^{+5\ +15}_{-16\ -14}$	–
	$\bar{b}'t'$	(493) $572^{+19\ +25}_{-37\ -17}$	–
800	$b'\bar{t}'$	(52.8) $64.0^{+2.1\ +5.1}_{-4.6\ -4.4}$	(181.7) $217.5^{+6.8\ +14.2}_{-15.8\ -13.0}$
	$\bar{b}'t'$	(126.2) $153.8^{+6.8\ +9.7}_{-12.5\ -6.6}$	(399.2) $480.0^{+19.9\ +23.7}_{-35.4\ -15.9}$
1000	$b'\bar{t}'$	(14.84) $18.68^{+1.11\ +1.97}_{-1.56\ -1.66}$	(41.44) $51.09^{+2.15\ +4.51}_{-3.91\ -3.89}$
	$\bar{b}'t'$	(38.8) $49.0^{+3.2\ +4.0}_{-4.1\ -2.7}$	(100.8) $125.2^{+6.7\ +8.4}_{-10.2\ -5.7}$
1200	$b'\bar{t}'$	(4.67) $6.07^{+0.44\ +0.79}_{-0.55\ -0.65}$	(11.67) $15.09^{+0.78\ +1.67}_{-1.50\ -1.39}$
	$\bar{b}'t'$	(13.24) $17.28^{+1.43\ +1.71}_{-1.66\ -1.17}$	(31.00) $39.80^{+2.57\ +3.39}_{-3.69\ -2.29}$
1400	$b'\bar{t}'$	(1.57) $2.13^{+0.17\ +0.36}_{-0.22\ -0.29}$	(3.68) $4.89^{+0.33\ +0.66}_{-0.51\ -0.54}$
	$\bar{b}'t'$	(4.83) $6.53^{+0.60\ +0.76}_{-0.70\ -0.52}$	(10.62) $14.05^{+1.19\ +1.45}_{-1.41\ -0.99}$
1600	$b'\bar{t}'$	(0.55) $0.76^{+0.08\ +0.14}_{-0.08\ -0.11}$	(1.24) $1.70^{+0.16\ +0.28}_{-0.18\ -0.22}$
	$\bar{b}'t'$	(1.83) $2.55^{+0.26\ +0.34}_{-0.29\ -0.23}$	(3.88) $5.30^{+0.48\ +0.64}_{-0.60\ -0.44}$
1800	$b'\bar{t}'$	(0.20) $0.28^{+0.04\ +0.06}_{-0.03\ -0.05}$	(0.44) $0.62^{+0.05\ +0.12}_{-0.08\ -0.09}$
	$\bar{b}'t'$	(0.72) $1.02^{+0.11\ +0.15}_{-0.13\ -0.11}$	(1.48) $2.07^{+0.22\ +0.29}_{-0.25\ -0.20}$
2000	$b'\bar{t}'$	(0.07) $0.11^{+0.01\ +0.03}_{-0.01\ -0.02}$	(0.16) $0.23^{+0.03\ +0.05}_{-0.03\ -0.04}$
	$\bar{b}'t'$	(0.28) $0.41^{+0.05\ +0.07}_{-0.05\ -0.05}$	(0.58) $0.83^{+0.10\ +0.13}_{-0.10\ -0.09}$

Table B.12: Same as Table B.11 but for the MSTW2008 PDF set.

BIBLIOGRAPHY

[1] M. L. Perl *et. al.*, "Evidence for anomalous lepton production in e+ e- annihilation," *Phys. Rev. Lett.* **35** (1975) 1489–1492.

[2] S. W. Herb *et. al.*, "Observation of a dimuon resonance at 9.5-GeV in 400-GeV proton - nucleus collisions," *Phys. Rev. Lett.* **39** (1977) 252–255.

[3] **ALEPH, DELPHI, L3, OPAL** Collaboration, "Combined preliminary data on Z parameters from the LEP experiments and constraints on the Standard Model,". Contributed to the 27th International Conference on High- Energy Physics - ICHEP 94, Glasgow, Scotland, UK, 20 - 27 Jul 1994.

[4] **CDF** Collaboration, F. Abe *et. al.*, "Observation of top quark production in $\bar{p}p$ collisions," *Phys. Rev. Lett.* **74** (1995) 2626–2631 [hep-ex/9503002].

[5] **D0** Collaboration, S. Abachi *et. al.*, "Observation of the top quark," *Phys. Rev. Lett.* **74** (1995) 2632–2637 [hep-ex/9503003].

[6] **Tevatron Electroweak Working Group** Collaboration, "Combination of CDF and D0 Results on the Mass of the Top Quark," arXiv:0808.1089 [hep-ex].

[7] **The CDF** Collaboration, T. Aaltonen *et. al.*, "First Observation of Electroweak Single Top Quark Production," arXiv:0903.0885 [hep-ex].

[8] **The D0** Collaboration, . V. M. Abazov, "Observation of Single Top Quark Production," arXiv:0903.0850 [hep-ex].

[9] R. Frederix, "Constraining CKM elements with direct top measurements," *Nuovo Cim.* **123B** (2008) 1118–1121.

[10] **JADE** Collaboration, W. Bartel *et. al.*, "A Measurement of the Electroweak Induced Charge Asymmetry in e+ e- → B anti-B," *Phys. Lett.* **B146** (1984) 437.

[11] P. Nason, S. Dawson and R. K. Ellis, "The Total Cross-Section for the Production of Heavy Quarks in Hadronic Collisions," *Nucl. Phys.* **B303** (1988) 607.

[12] W. Beenakker, H. Kuijf, W. L. van Neerven and J. Smith, "QCD Corrections to Heavy Quark Production in p anti-p Collisions," *Phys. Rev.* **D40** (1989) 54–82.

[13] W. Beenakker, W. L. van Neerven, R. Meng, G. A. Schuler and J. Smith, "QCD corrections to heavy quark production in hadron hadron collisions," *Nucl. Phys.* **B351** (1991) 507–560.

[14] G. Sterman, "Summation of Large Corrections to Short Distance Hadronic Cross-Sections," *Nucl. Phys.* **B281** (1987) 310.

[15] S. Catani and L. Trentadue, "Resummation of the QCD Perturbative Series for Hard Processes," *Nucl. Phys.* **B327** (1989) 323.

[16] S. Catani and L. Trentadue, "Comment on QCD exponentiation at large x," *Nucl. Phys.* **B353** (1991) 183–186.

[17] E. Laenen, J. Smith and W. L. van Neerven, "All order resummation of soft gluon contributions to heavy quark production in hadron hadron collisions," *Nucl. Phys.* **B369** (1992) 543–599.

[18] E. Laenen, J. Smith and W. L. van Neerven, "Top quark production cross-section," *Phys. Lett.* **B321** (1994) 254–258 [hep-ph/9310233].

[19] E. L. Berger and H. Contopanagos, "Perturbative gluon resummation of the top quark production cross-section," *Phys. Lett.* **B361** (1995) 115–120 [hep-ph/9507363].

[20] E. L. Berger and H. Contopanagos, "The Perturbative resummed series for top quark production in hadron reactions," *Phys. Rev.* **D54** (1996) 3085–3113 [hep-ph/9603326].

[21] E. L. Berger and H. Contopanagos, "Threshold resummation of the total cross-section for heavy quark production in hadronic collisions," *Phys. Rev.* **D57** (1998) 253–264 [hep-ph/9706206].

[22] S. Catani, M. L. Mangano, P. Nason and L. Trentadue, "The Top cross-section in hadronic collisions," *Phys. Lett.* **B378** (1996) 329–336 [hep-ph/9602208].

[23] S. Catani, M. L. Mangano, P. Nason and L. Trentadue, "The Resummation of Soft Gluon in Hadronic Collisions," *Nucl. Phys.* **B478** (1996) 273–310 [hep-ph/9604351].

[24] M. Cacciari, S. Frixione, M. L. Mangano, P. Nason and G. Ridolfi, "The t anti-t cross-section at 1.8-TeV and 1.96-TeV: A study of the systematics due to parton densities and scale dependence," *JHEP* **04** (2004) 068 [hep-ph/0303085].

[25] M. Cacciari, S. Frixione, M. L. Mangano, P. Nason and G. Ridolfi, "Updated predictions for the total production cross sections of top and of heavier quark pairs at the Tevatron and at the LHC," *JHEP* **09** (2008) 127 [arXiv:0804.2800 [hep-ph]].

[26] R. Bonciani, S. Catani, M. L. Mangano and P. Nason, "NLL resummation of the heavy-quark hadroproduction cross- section," *Nucl. Phys.* **B529** (1998) 424–450 [hep-ph/9801375].

[27] N. Kidonakis and G. Sterman, "Resummation for QCD hard scattering," *Nucl. Phys.* **B505** (1997) 321–348 [hep-ph/9705234].

[28] N. Kidonakis, E. Laenen, S. Moch and R. Vogt, "Sudakov resummation and finite order expansions of heavy quark hadroproduction cross sections," *Phys. Rev.* **D64** (2001) 114001 [hep-ph/0105041].

[29] N. Kidonakis and R. Vogt, "Next-to-next-to-leading order soft gluon corrections in top quark hadroproduction," *Phys. Rev.* **D68** (2003) 114014 [hep-ph/0308222].

[30] N. Kidonakis, "Single top production at the Tevatron: Threshold resummation and finite-order soft gluon corrections," *Phys. Rev.* **D74** (2006) 114012 [hep-ph/0609287].

[31] N. Kidonakis and R. Vogt, "The Theoretical top quark cross section at the Tevatron and the LHC," *Phys. Rev.* **D78** (2008) 074005 [arXiv:0805.3844 [hep-ph]].

[32] A. Banfi and E. Laenen, "Joint resummation for heavy quark production," *Phys. Rev.* **D71** (2005) 034003 [hep-ph/0411241].

[33] S. Moch and P. Uwer, "Theoretical status and prospects for top-quark pair production at hadron colliders," *Phys. Rev.* **D78** (2008) 034003 [arXiv:0804.1476 [hep-ph]].

[34] A. D. Martin, W. J. Stirling, R. S. Thorne and G. Watt, "Update of parton distributions at NNLO," *Phys. Lett.* **B652** (2007) 292–299 [arXiv:0706.0459 [hep-ph]].

[35] W. Bernreuther, A. Brandenburg, Z. G. Si and P. Uwer, "Top quark spin correlations at hadron colliders: Predictions at next-to-leading order QCD," *Phys. Rev. Lett.* **87** (2001) 242002 [hep-ph/0107086].

[36] W. Bernreuther, A. Brandenburg, Z. G. Si and P. Uwer, "Top quark pair production and decay at hadron colliders," *Nucl. Phys.* **B690** (2004) 81–137 [hep-ph/0403035].

[37] J. H. Kuhn, A. Scharf and P. Uwer, "Electroweak effects in top-quark pair production at hadron colliders," *Eur. Phys. J.* **C51** (2007) 37–53 [hep-ph/0610335].

[38] W. Bernreuther, M. Fuecker and Z.-G. Si, "Weak interaction corrections to hadronic top quark pair production," *Phys. Rev.* **D74** (2006) 113005 [hep-ph/0610334].

[39] W. Beenakker, F. A. Berends and A. P. Chapovsky, "One-loop QCD interconnection effects in pair production of top quarks," *Phys. Lett.* **B454** (1999) 129–136 [hep-ph/9902304].

[40] S. Frixione and B. R. Webber, "The MC@NLO 3.3 event generator," hep-ph/0612272.

[41] S. Frixione, P. Nason and G. Ridolfi, "A Positive-Weight Next-to-Leading-Order Monte Carlo for Heavy Flavour Hadroproduction," *JHEP* **09** (2007) 126 [arXiv:0707.3088 [hep-ph]].

[42] S. S. D. Willenbrock and D. A. Dicus, "Production of Heavy Quarks from W Gluon Fusion," *Phys. Rev.* **D34** (1986) 155.

[43] C. P. Yuan, "A New Method to Detect a Heavy Top Quark at the Tevatron," *Phys. Rev.* **D41** (1990) 42.

[44] R. K. Ellis and S. J. Parke, "Top quark production by W gluon fusion," *Phys. Rev.* **D46** (1992) 3785–3788.

[45] S. Cortese and R. Petronzio, "The Single top production channel at Tevatron energies," *Phys. Lett.* **B253** (1991) 494–498.

[46] T. Stelzer and S. Willenbrock, "Single top quark production via $q\bar{q} \to t\bar{b}$," *Phys. Lett.* **B357** (1995) 125–130 [hep-ph/9505433].

[47] A. Heinson, A. S. Belyaev and E. E. Boos, "Single top quarks at the Fermilab Tevatron," *Phys. Rev.* **D56** (1997) 3114–3128 [hep-ph/9612424].

[48] T. M. P. Tait, "The tW^- mode of single top production," *Phys. Rev.* **D61** (2000) 034001 [hep-ph/9909352].

[49] J. M. Campbell and F. Tramontano, "Next-to-leading order corrections to W t production and decay," *Nucl. Phys.* **B726** (2005) 109–130 [hep-ph/0506289].

[50] S. Frixione, E. Laenen, P. Motylinski, B. R. Webber and C. D. White, "Single-top hadroproduction in association with a W boson," *JHEP* **07** (2008) 029 [arXiv:0805.3067 [hep-ph]].

[51] C. D. White, S. Frixione, E. Laenen and F. Maltoni, "Isolating Wt production at the LHC," arXiv:0908.0631 [hep-ph].

[52] G. Bordes and B. van Eijk, "Calculating QCD corrections to single top production in hadronic interactions," *Nucl. Phys.* **B435** (1995) 23–58.

[53] T. Stelzer, Z. Sullivan and S. Willenbrock, "Single-top-quark production via W-gluon fusion at next-to- leading order," *Phys. Rev.* **D56** (1997) 5919–5927 [hep-ph/9705398].

[54] B. W. Harris, E. Laenen, L. Phaf, Z. Sullivan and S. Weinzierl, "The fully differential single top quark cross section in next-to-leading order QCD," *Phys. Rev.* **D66** (2002) 054024 [hep-ph/0207055].

[55] J. M. Campbell, R. K. Ellis and F. Tramontano, "Single top production and decay at next-to-leading order," *Phys. Rev.* **D70** (2004) 094012 [hep-ph/0408158].

[56] Q.-H. Cao, R. Schwienhorst and C. P. Yuan, "Next-to-leading order corrections to single top quark production and decay at Tevatron. I: s-channel process," *Phys. Rev.* **D71** (2005) 054023 [hep-ph/0409040].

[57] Q.-H. Cao, R. Schwienhorst, J. A. Benitez, R. Brock and C. P. Yuan, "Next-to-leading order corrections to single top quark production and decay at the Tevatron. II: t-channel process," *Phys. Rev.* **D72** (2005) 094027 [hep-ph/0504230].

[58] S. Frixione, E. Laenen, P. Motylinski and B. R. Webber, "Single-top production in MC@NLO," *JHEP* **03** (2006) 092 [hep-ph/0512250].

[59] J. M. Campbell, R. Frederix, F. Maltoni and F. Tramontano, "t-channel single-top production at hadron colliders," *Phys. Rev. Lett.* **102** (2009) 182003 [arXiv:0903.0005 [hep-ph]].

[60] N. Arkani-Hamed, A. G. Cohen and H. Georgi, "Electroweak symmetry breaking from dimensional deconstruction," *Phys. Lett.* **B513** (2001) 232–240 [hep-ph/0105239].

[61] N. Arkani-Hamed, A. G. Cohen, T. Gregoire and J. G. Wacker, "Phenomenology of electroweak symmetry breaking from theory space," *JHEP* **08** (2002) 020 [hep-ph/0202089].

[62] N. Arkani-Hamed *et. al.*, "The Minimal Moose for a Little Higgs," *JHEP* **08** (2002) 021 [hep-ph/0206020].

[63] N. Arkani-Hamed, A. G. Cohen, E. Katz and A. E. Nelson, "The littlest Higgs," *JHEP* **07** (2002) 034 [hep-ph/0206021].

[64] I. Low, W. Skiba and D. Tucker-Smith, "Little Higgses from an antisymmetric condensate," *Phys. Rev.* **D66** (2002) 072001 [hep-ph/0207243].

[65] T. Han, H. E. Logan, B. McElrath and L.-T. Wang, "Phenomenology of the little Higgs model," *Phys. Rev.* **D67** (2003) 095004 [hep-ph/0301040].

[66] G. Azuelos *et. al.*, "Exploring little Higgs models with ATLAS at the LHC," *Eur. Phys. J.* **C39S2** (2005) 13–24 [hep-ph/0402037].

[67] M. Schmaltz and D. Tucker-Smith, "Little Higgs Review," *Ann. Rev. Nucl. Part. Sci.* **55** (2005) 229–270 [hep-ph/0502182].

[68] C. T. Hill, "Topcolor: Top quark condensation in a gauge extension of the standard model," *Phys. Lett.* **B266** (1991) 419–424.

[69] C. T. Hill, "Topcolor assisted technicolor," *Phys. Lett.* **B345** (1995) 483–489 [hep-ph/9411426].

[70] C. T. Hill and S. J. Parke, "Top production: Sensitivity to new physics," *Phys. Rev.* **D49** (1994) 4454–4462 [hep-ph/9312324].

[71] R. M. Harris, C. T. Hill and S. J. Parke, "Cross section for topcolor Z'(t) decaying to t anti-t," hep-ph/9911288.

[72] B. A. Dobrescu and C. T. Hill, "Electroweak symmetry breaking via top condensation seesaw," *Phys. Rev. Lett.* **81** (1998) 2634–2637 [hep-ph/9712319].

[73] R. S. Chivukula, B. A. Dobrescu, H. Georgi and C. T. Hill, "Top quark seesaw theory of electroweak symmetry breaking," *Phys. Rev.* **D59** (1999) 075003 [hep-ph/9809470].

[74] H.-J. He, C. T. Hill and T. M. P. Tait, "Top quark seesaw, vacuum structure and electroweak precision constraints," *Phys. Rev.* **D65** (2002) 055006 [hep-ph/0108041].

[75] N. Arkani-Hamed, S. Dimopoulos and G. R. Dvali, "The hierarchy problem and new dimensions at a millimeter," *Phys. Lett.* **B429** (1998) 263–272 [hep-ph/9803315].

[76] L. Randall and R. Sundrum, "A large mass hierarchy from a small extra dimension," *Phys. Rev. Lett.* **83** (1999) 3370–3373 [hep-ph/9905221].

[77] A. L. Fitzpatrick, J. Kaplan, L. Randall and L.-T. Wang, "Searching for the Kaluza-Klein graviton in bulk RS models," *JHEP* **09** (2007) 013 [hep-ph/0701150].

[78] M. Arai, N. Okada, K. Smolek and V. Simak, "Top spin correlations in theories with large extra- dimensions at the Large Hadron Collider," *Phys. Rev.* **D70** (2004) 115015 [hep-ph/0409273].

[79] M. Arai, N. Okada, K. Smolek and V. Simak, "Top quark spin correlations in the Randall-Sundrum model at the CERN Large Hadron Collider," *Phys. Rev.* **D75** (2007) 095008 [hep-ph/0701155].

[80] C. D. McMullen and S. Nandi, "Collider implications of Kaluza-Klein excitations of the electroweak gauge bosons," hep-ph/0110275.

[81] K. Agashe, A. Delgado, M. J. May and R. Sundrum, "RS1, custodial isospin and precision tests," *JHEP* **08** (2003) 050 [hep-ph/0308036].

[82] K. Agashe, A. Belyaev, T. Krupovnickas, G. Perez and J. Virzi, "LHC signals from warped extra dimensions," *Phys. Rev.* **D77** (2008) 015003 [hep-ph/0612015].

[83] B. Lillie, L. Randall and L.-T. Wang, "The Bulk RS KK-gluon at the LHC," *JHEP* **09** (2007) 074 [hep-ph/0701166].

[84] A. Djouadi, G. Moreau and R. K. Singh, "Kaluza–Klein excitations of gauge bosons at the LHC," *Nucl. Phys.* **B797** (2008) 1–26 [arXiv:0706.4191 [hep-ph]].

[85] R. Ghavri, C. D. McMullen and S. Nandi, "Collider implications of multiple non-universal extra dimensions," *Phys. Rev.* **D74** (2006) 015012 [hep-ph/0602014].

[86] G. Burdman, B. A. Dobrescu and E. Ponton, "Resonances from Two Universal Extra Dimensions," *Phys. Rev.* **D74** (2006) 075008 [hep-ph/0601186].

[87] B. Lillie, J. Shu and T. M. P. Tait, "Kaluza-Klein Gluons as a Diagnostic of Warped Models," *Phys. Rev.* **D76** (2007) 115016 [arXiv:0706.3960 [hep-ph]].

[88] K. Agashe *et. al.*, "LHC Signals for Warped Electroweak Neutral Gauge Bosons," *Phys. Rev.* **D76** (2007) 115015 [arXiv:0709.0007 [hep-ph]].

[89] J. Alwall *et. al.*, "Is V(tb) $= 1$?," *Eur. Phys. J.* **C49** (2007) 791–801 [hep-ph/0607115].

[90] G. D. Kribs, T. Plehn, M. Spannowsky and T. M. P. Tait, "Four generations and Higgs physics," *Phys. Rev.* **D76** (2007) 075016 [arXiv:0706.3718 [hep-ph]].

[91] M. S. Chanowitz, "Bounding CKM Mixing with a Fourth Family," arXiv:0904.3570 [hep-ph].

[92] B. Holdom *et. al.*, "Four Statements about the Fourth Generation," arXiv:0904.4698 [hep-ph].

[93] T. Stelzer and W. F. Long, "Automatic generation of tree level helicity amplitudes," *Comput. Phys. Commun.* **81** (1994) 357–371 [hep-ph/9401258].

[94] F. Maltoni and T. Stelzer, "MadEvent: Automatic event generation with MadGraph," *JHEP* **02** (2003) 027 [hep-ph/0208156].

[95] J. Alwall *et. al.*, "MadGraph/MadEvent v4: The New Web Generation," *JHEP* **09** (2007) 028 [arXiv:0706.2334 [hep-ph]].

[96] J. M. Campbell and R. K. Ellis, "An update on vector boson pair production at hadron colliders," *Phys. Rev.* **D60** (1999) 113006 [hep-ph/9905386].

[97] J. Pumplin *et. al.*, "New generation of parton distributions with uncertainties from global QCD analysis," *JHEP* **07** (2002) 012 [hep-ph/0201195].

[98] M. Beneke *et. al.*, "Top quark physics," hep-ph/0003033.

[99] S. Frixione, P. Nason and B. R. Webber, "Matching NLO QCD and parton showers in heavy flavour production," *JHEP* **08** (2003) 007 [hep-ph/0305252].

[100] P. Ferrari, "Early physics with top quarks at the LHC," arXiv:0705.3021 [hep-ex].

[101] U. Baur and L. H. Orr, "High p_T Top Quarks at the Large Hadron Collider," *Phys. Rev.* **D76** (2007) 094012 [arXiv:0707.2066 [hep-ph]].

[102] U. Baur and L. H. Orr, "Searching for t-bar t Resonances at the Large Hadron Collider," *Phys. Rev.* **D77** (2008) 114001 [arXiv:0803.1160 [hep-ph]].

[103] **CDF** Collaboration, T. Aaltonen *et. al.*, "First Measurement of the $t\bar{t}$ Differential Cross Section $d\sigma/dM_{t\bar{t}}$ in $p\bar{p}$ Collisions at $\sqrt{s} = 1.96$ TeV," arXiv:0903.2850 [hep-ex].

[104] M. C. Smith and S. S. Willenbrock, "Top-quark pole mass," *Phys. Rev. Lett.* **79** (1997) 3825–3828 [hep-ph/9612329].

[105] K. Hagiwara, Y. Sumino and H. Yokoya, "Bound-state Effects on Top Quark Production at Hadron Colliders," *Phys. Lett.* **B666** (2008) 71–76 [arXiv:0804.1014 [hep-ph]].

[106] Y. Kiyo, J. H. Kuhn, S. Moch, M. Steinhauser and P. Uwer, "Top-quark pair production near threshold at LHC," *Eur. Phys. J.* **C60** (2009) 375–386 [arXiv:0812.0919 [hep-ph]].

[107] T. Sjostrand, S. Mrenna and P. Skands, "PYTHIA 6.4 physics and manual," *JHEP* **05** (2006) 026 [hep-ph/0603175].

[108] G. Corcella *et. al.*, "HERWIG 6.4 release note," hep-ph/0201201.

[109] K. J. F. Gaemers and F. Hoogeveen, "Higgs production and decay into heavy flavors with the gluon fusion mechanism," *Phys. Lett.* **B146** (1984) 347.

[110] D. Dicus, A. Stange and S. Willenbrock, "Higgs decay to top quarks at hadron colliders," *Phys. Lett.* **B333** (1994) 126–131 [hep-ph/9404359].

[111] W. Bernreuther, M. Flesch and P. Haberl, "Signatures of Higgs bosons in the top quark decay channel at hadron colliders," *Phys. Rev.* **D58** (1998) 114031 [hep-ph/9709284].

[112] A. V. Manohar and M. B. Wise, "Flavor changing neutral currents, an extended scalar sector, and the Higgs production rate at the LHC," *Phys. Rev.* **D74** (2006) 035009 [hep-ph/0606172].

[113] M. I. Gresham and M. B. Wise, "Color Octet Scalar Production at the LHC," *Phys. Rev.* **D76** (2007) 075003 [arXiv:0706.0909 [hep-ph]].

[114] E. H. Simmons, "Coloron phenomenology," *Phys. Rev.* **D55** (1997) 1678–1683 [hep-ph/9608269].

[115] D. Choudhury, R. M. Godbole, R. K. Singh and K. Wagh, "Top production at the Tevatron / LHC and nonstandard, strongly interacting spin one particles," *Phys. Lett.* **B657** (2007) 69–76 [arXiv:0705.1499 [hep-ph]].

[116] D. A. Dicus, C. D. McMullen and S. Nandi, "Collider implications of Kaluza-Klein excitations of the gluons," *Phys. Rev.* **D65** (2002) 076007 [hep-ph/0012259].

[117] A. Djouadi, "The anatomy of electro-weak symmetry breaking. II: The Higgs bosons in the minimal supersymmetric model," *Phys. Rept.* **459** (2008) 1–241 [hep-ph/0503173].

[118] K. Cheung and W.-Y. Keung, "Split supersymmetry, stable gluino, and gluinonium," *Phys. Rev.* **D71** (2005) 015015 [hep-ph/0408335].

[119] C.-N. Yang, "Selection Rules for the Dematerialization of a Particle Into Two Photons," *Phys. Rev.* **77** (1950) 242–245.

[120] P. H. Frampton and S. L. Glashow, "Unifiable chiral color with natural GIM mechanism," *Phys. Rev. Lett.* **58** (1987) 2168.

[121] P. H. Frampton and S. L. Glashow, "Chiral Color: An Alternative to the Standard Model," *Phys. Lett.* **B190** (1987) 157.

[122] O. Antunano, J. H. Kuhn and G. Rodrigo, "Top Quarks, Axigluons and Charge Asymmetries at Hadron Colliders," *Phys. Rev.* **D77** (2008) 014003 [arXiv:0709.1652 [hep-ph]].

[123] N. Arkani-Hamed, S. Dimopoulos and G. R. Dvali, "Phenomenology, astrophysics and cosmology of theories with sub-millimeter dimensions and TeV scale quantum gravity," *Phys. Rev.* **D59** (1999) 086004 [hep-ph/9807344].

[124] L. Randall and R. Sundrum, "An alternative to compactification," *Phys. Rev. Lett.* **83** (1999) 4690–4693 [hep-th/9906064].

[125] J. C. Collins and D. E. Soper, "Angular Distribution of Dileptons in High-Energy Hadron Collisions," *Phys. Rev.* **D16** (1977) 2219.

[126] V. Barger, T. Han and D. G. E. Walker, "Top Quark Pairs at High Invariant Mass - A Model- Independent Discriminator of New Physics at the LHC," *Phys. Rev. Lett.* **100** (2008) 031801 [hep-ph/0612016].

[127] S. Willenbrock, "The standard model and the top quark," hep-ph/0211067.

[128] M. Jezabek and J. H. Kuhn, "V-A tests through leptons from polarized top quarks," *Phys. Lett.* **B329** (1994) 317–324 [hep-ph/9403366].

[129] A. Czarnecki, M. Jezabek and J. H. Kuhn, "Lepton spectra from decays of polarized top quarks," *Nucl. Phys.* **B351** (1991) 70–80.

[130] R. H. Dalitz and G. R. Goldstein, "Analysis of top-antitop production and dilepton decay events and the top quark mass," *Phys. Lett.* **B287** (1992) 225–230.

[131] L. Sonnenschein, "Analytical solution of t anti-t dilepton equations," *Phys. Rev.* **D73** (2006) 054015 [hep-ph/0603011].

[132] **CDF** Collaboration, D. E. Acosta *et. al.*, "Search for anomalous kinematics in $t\bar{t}$ dilepton events at CDF II," *Phys. Rev. Lett.* **95** (2005) 022001 [hep-ex/0412042].

[133] M. Baarmand, H. Mermerkaya and I. Vodopianov, "Measurement of spin correlation in top quark pair production in semi-leptonic final state,". CERN-CMS-NOTE-2006-111.

[134] G. Mahlon and S. J. Parke, "Angular Correlations in Top Quark Pair Production and Decay at Hadron Colliders," *Phys. Rev.* **D53** (1996) 4886–4896 [hep-ph/9512264].

[135] B. C. Allanach *et. al.*, "The Snowmass points and slopes: Benchmarks for SUSY searches," *Eur. Phys. J.* **C25** (2002) 113–123 [hep-ph/0202233].

[136] **CMS** Collaboration, G. L. Bayatian *et. al.*, "CMS technical design report, volume II: Physics performance," *J. Phys.* **G34** (2007) 995–1579.

[137] I. Borjanovic *et. al.*, "Investigation of top mass measurements with the ATLAS detector at LHC," *Eur. Phys. J.* **C39S2** (2005) 63–90 [hep-ex/0403021].

[138] **Particle Data Group** Collaboration, W. M. Yao *et. al.*, "Review of particle physics," *J. Phys.* **G33** (2006) 1–1232.

[139] F. del Aguila *et. al.*, "Collider aspects of flavour physics at high Q," *Eur. Phys. J.* **C57** (2008) 183–308 [arXiv:0801.1800 [hep-ph]].

[140] **Particle Data Group** Collaboration, S. Eidelman *et. al.*, "Review of particle physics," *Phys. Lett.* **B592** (2004) 1.

[141] P. Bamert, C. P. Burgess, J. M. Cline, D. London and E. Nardi, "R(b) and new physics: A Comprehensive analysis," *Phys. Rev.* **D54** (1996) 4275–4300 [hep-ph/9602438].

[142] **CDF** Collaboration, J. Conway *et. al.*, "Search for heavy top $t' \to Wq$ in lepton plus jets events,". NOTE 9446.

[143] F. J. Botella and L.-L. Chau, "Anticipating the Higher Generations of Quarks from Rephasing Invariance of the Mixing Matrix," *Phys. Lett.* **B168** (1986) 97.

[144] **D0** Collaboration, V. M. Abazov *et. al.*, "Simultaneous measurement of the ratio B($t \to Wb$) /B($t \to Wq$) and the top quark pair production cross section with the D0 detector at $\sqrt{s} = 1.96$-TeV," *Phys. Rev. Lett.* **100** (2008) 192003 [arXiv:0801.1326 [hep-ex]].

[145] **CDF** Collaboration, D. Hirschbühl *et. al.*, "Search for Electroweak Single Top-Quark Production using Neural Networks with 3.2 fb-1 of CDF II data,". NOTE 9716.

[146] Z. Sullivan, "Understanding single-top-quark production and jets at hadron colliders," *Phys. Rev.* **D70** (2004) 114012 [hep-ph/0408049].

[147] T. Stelzer, Z. Sullivan and S. Willenbrock, "Single top quark production at hadron colliders," *Phys. Rev.* **D58** (1998) 094021 [hep-ph/9807340].

[148] M. T. Bowen, S. D. Ellis and M. J. Strassler, "In search of lonely top quarks at the Tevatron," *Phys. Rev.* **D72** (2005) 074016 [hep-ph/0412223].

[149] T. M. P. Tait and C. P. Yuan, "Single top quark production as a window to physics beyond the Standard Model," *Phys. Rev.* **D63** (2001) 014018 [hep-ph/0007298].

[150] J. C. Collins, "Hard-scattering factorization with heavy quarks: A general treatment," *Phys. Rev.* **D58** (1998) 094002 [hep-ph/9806259].

[151] M. Kramer, F. I. Olness and D. E. Soper, "Treatment of heavy quarks in deeply inelastic scattering," *Phys. Rev.* **D62** (2000) 096007 [hep-ph/0003035].

[152] J. A. M. Vermaseren, "New features of FORM," math-ph/0010025.

[153] A. Signer and D. Stockinger, "Using Dimensional Reduction for Hadronic Collisions," *Nucl. Phys.* **B808** (2009) 88–120 [arXiv:0807.4424 [hep-ph]].

[154] G. Passarino and M. J. G. Veltman, "One Loop Corrections for e+ e- Annihilation Into mu+ mu- in the Weinberg Model," *Nucl. Phys.* **B160** (1979) 151.

[155] R. K. Ellis and G. Zanderighi, "Scalar one-loop integrals for QCD," *JHEP* **02** (2008) 002 [arXiv:0712.1851 [hep-ph]].

[156] S. Frixione, E. Laenen, P. Motylinski and B. R. Webber, "Angular correlations of lepton pairs from vector boson and top quark decays in Monte Carlo simulations," *JHEP* **04** (2007) 081 [hep-ph/0702198].

[157] W. T. Giele and E. W. N. Glover, "Higher order corrections to jet cross-sections in e+ e- annihilation," *Phys. Rev.* **D46** (1992) 1980–2010.

[158] Z. Kunszt and D. E. Soper, "Calculation of jet cross-sections in hadron collisions at order alpha-s**3," *Phys. Rev.* **D46** (1992) 192–221.

[159] S. Frixione, Z. Kunszt and A. Signer, "Three-jet cross sections to next-to-leading order," *Nucl. Phys.* **B467** (1996) 399–442 [hep-ph/9512328].

[160] S. Catani and M. H. Seymour, "A general algorithm for calculating jet cross sections in NLO QCD," *Nucl. Phys.* **B485** (1997) 291–419 [hep-ph/9605323].

[161] S. Catani, S. Dittmaier, M. H. Seymour and Z. Trocsanyi, "The dipole formalism for next-to-leading order QCD calculations with massive partons," *Nucl. Phys.* **B627** (2002) 189–265 [hep-ph/0201036].

[162] D. A. Kosower, "Antenna factorization of gauge-theory amplitudes," *Phys. Rev.* **D57** (1998) 5410–5416 [hep-ph/9710213].

[163] J. M. Campbell, M. A. Cullen and E. W. N. Glover, "Four jet event shapes in electron positron annihilation," *Eur. Phys. J.* **C9** (1999) 245–265 [hep-ph/9809429].

[164] A. Gehrmann-De Ridder, T. Gehrmann and E. W. N. Glover, "Antenna Subtraction at NNLO," *JHEP* **09** (2005) 056 [hep-ph/0505111].

[165] A. Daleo, T. Gehrmann and D. Maitre, "Antenna subtraction with hadronic initial states," *JHEP* **04** (2007) 016 [hep-ph/0612257].

[166] R. Frederix, T. Gehrmann and N. Greiner, "Automation of the Dipole Subtraction Method in MadGraph/MadEvent," *JHEP* **09** (2008) 122 [arXiv:0808.2128 [hep-ph]].

[167] P. Nason and C. Oleari, "Next-to-leading-order corrections to the production of heavy-flavour jets in e+ e- collisions," *Nucl. Phys.* **B521** (1998) 237–273 [hep-ph/9709360].

[168] A. D. Martin, W. J. Stirling and R. S. Thorne, "MRST partons generated in a fixed-flavour scheme," *Phys. Lett.* **B636** (2006) 259–264 [hep-ph/0603143].

[169] A. D. Martin, W. J. Stirling, R. S. Thorne and G. Watt, "Parton distributions for the LHC," arXiv:0901.0002 [hep-ph].

[170] P. M. Nadolsky *et. al.*, "Implications of CTEQ global analysis for collider observables," *Phys. Rev.* **D78** (2008) 013004 [arXiv:0802.0007 [hep-ph]].

[171] M. Cacciari, M. Greco and P. Nason, "The p(T) spectrum in heavy-flavour hadroproduction," *JHEP* **05** (1998) 007 [hep-ph/9803400].

[172] S. Frixione and M. L. Mangano, "Heavy quark jets in hadronic collisions," *Nucl. Phys.* **B483** (1997) 321–338 [hep-ph/9605270].

[173] **TeV4LHC-Top and Electroweak Working Group** Collaboration, C. E. Gerber *et. al.*, "Tevatron-for-LHC Report: Top and Electroweak Physics," arXiv:0705.3251 [hep-ph].

[174] E. E. Boos, V. E. Bunichev, L. V. Dudko, V. I. Savrin and A. V. Sherstnev, "Method for simulating electroweak top-quark production events in the NLO approximation: SingleTop event generator," *Phys. Atom. Nucl.* **69** (2006) 1317–1329.

[175] **Tevatron Electroweak Working Group** Collaboration, "Combination of CDF and D0 Results on the Mass of the Top Quark," arXiv:0903.2503 [hep-ex].

[176] **CompHEP** Collaboration, E. Boos *et. al.*, "CompHEP 4.4: Automatic computations from Lagrangians to events," *Nucl. Instrum. Meth.* **A534** (2004) 250–259 [hep-ph/0403113].

[177] A. Pukhov, "CalcHEP 3.2: MSSM, structure functions, event generation, batchs, and generation of matrix elements for other packages," hep-ph/0412191.

[178] T. Gleisberg *et. al.*, "SHERPA 1.alpha, a proof-of-concept version," *JHEP* **02** (2004) 056 [hep-ph/0311263].

[179] W. Kilian, "WHIZARD 1.0: A generic Monte-Carlo integration and event generation package for multi-particle processes. Manual,". LC-TOOL-2001-039.

[180] M. L. Mangano, M. Moretti, F. Piccinini, R. Pittau and A. D. Polosa, "ALPGEN, a generator for hard multiparton processes in hadronic collisions," *JHEP* **07** (2003) 001 [hep-ph/0206293].

[181] A. Kanaki and C. G. Papadopoulos, "HELAC: A package to compute electroweak helicity amplitudes," *Comput. Phys. Commun.* **132** (2000) 306–315 [hep-ph/0002082].

[182] J. M. Campbell and R. K. Ellis, "Next-to-leading order corrections to W + 2jet and Z + 2jet production at hadron colliders," *Phys. Rev.* **D65** (2002) 113007 [hep-ph/0202176].

[183] Z. Nagy, "Next-to-leading order calculation of three-jet observables in hadron-hadron collision," *Phys. Rev.* **D68** (2003) 094002 [hep-ph/0307268].

[184] S. Frixione and B. R. Webber, "Matching NLO QCD computations and parton shower simulations," *JHEP* **06** (2002) 029 [hep-ph/0204244].

[185] P. Nason, "A new method for combining NLO QCD with shower Monte Carlo algorithms," *JHEP* **11** (2004) 040 [hep-ph/0409146].

[186] P. Nason and G. Ridolfi, "A positive-weight next-to-leading-order Monte Carlo for Z pair hadroproduction," *JHEP* **08** (2006) 077 [hep-ph/0606275].

[187] O. Latunde-Dada, S. Gieseke and B. Webber, "A positive-weight next-to-leading-order Monte Carlo for e+ e- annihilation to hadrons," *JHEP* **02** (2007) 051 [hep-ph/0612281].

[188] S. Alioli, P. Nason, C. Oleari and E. Re, "NLO vector-boson production matched with shower in POWHEG," *JHEP* **07** (2008) 060 [arXiv:0805.4802 [hep-ph]].

[189] K. Hamilton, P. Richardson and J. Tully, "A Positive-Weight Next-to-Leading Order Monte Carlo Simulation of Drell-Yan Vector Boson Production," *JHEP* **10** (2008) 015 [arXiv:0806.0290 [hep-ph]].

[190] D. B. Melrose, "Reduction of Feynman diagrams," *Nuovo Cim.* **40** (1965) 181–213.

[191] Z. Bern, L. J. Dixon and D. A. Kosower, "Dimensionally regulated pentagon integrals," *Nucl. Phys.* **B412** (1994) 751–816 [hep-ph/9306240].

[192] Z. Bern, L. J. Dixon, D. C. Dunbar and D. A. Kosower, "One-Loop n-Point Gauge Theory Amplitudes, Unitarity and Collinear Limits," *Nucl. Phys.* **B425** (1994) 217–260 [hep-ph/9403226].

[193] Z. Bern and A. G. Morgan, "Massive Loop Amplitudes from Unitarity," *Nucl. Phys.* **B467** (1996) 479–509 [hep-ph/9511336].

[194] Z. Bern, L. J. Dixon and D. A. Kosower, "Bootstrapping multi-parton loop amplitudes in QCD," *Phys. Rev.* **D73** (2006) 065013 [hep-ph/0507005].

[195] C. F. Berger, Z. Bern, L. J. Dixon, D. Forde and D. A. Kosower, "Bootstrapping one-loop QCD amplitudes with general helicities," *Phys. Rev.* **D74** (2006) 036009 [hep-ph/0604195].

[196] D. Forde, "Direct extraction of one-loop integral coefficients," *Phys. Rev.* **D75** (2007) 125019 [arXiv:0704.1835 [hep-ph]].

[197] A. Denner, S. Dittmaier, M. Roth and L. H. Wieders, "Electroweak corrections to charged-current e+ e- –¿ 4 fermion processes: Technical details and further results," *Nucl. Phys.* **B724** (2005) 247–294 [hep-ph/0505042].

[198] A. Denner and S. Dittmaier, "Reduction schemes for one-loop tensor integrals," *Nucl. Phys.* **B734** (2006) 62–115 [hep-ph/0509141].

[199] T. Binoth, J. P. Guillet, G. Heinrich, E. Pilon and C. Schubert, "An algebraic / numerical formalism for one-loop multi-leg amplitudes," *JHEP* **10** (2005) 015 [hep-ph/0504267].

[200] T. Binoth, J. P. Guillet and G. Heinrich, "Algebraic evaluation of rational polynomials in one-loop amplitudes," *JHEP* **02** (2007) 013 [hep-ph/0609054].

[201] R. Britto, B. Feng and P. Mastrolia, "The cut-constructible part of QCD amplitudes," *Phys. Rev.* **D73** (2006) 105004 [hep-ph/0602178].

[202] P. Mastrolia, "On triple-cut of scattering amplitudes," *Phys. Lett.* **B644** (2007) 272–283 [hep-th/0611091].

[203] R. Britto and B. Feng, "Integral Coefficients for One-Loop Amplitudes," *JHEP* **02** (2008) 095 [arXiv:0711.4284 [hep-ph]].

[204] R. Britto, B. Feng and P. Mastrolia, "Closed-Form Decomposition of One-Loop Massive Amplitudes," *Phys. Rev.* **D78** (2008) 025031 [arXiv:0803.1989 [hep-ph]].

[205] C. Anastasiou, R. Britto, B. Feng, Z. Kunszt and P. Mastrolia, "Unitarity cuts and reduction to master integrals in d dimensions for one-loop amplitudes," *JHEP* **03** (2007) 111 [hep-ph/0612277].

[206] R. K. Ellis, W. T. Giele and Z. Kunszt, "A Numerical Unitarity Formalism for Evaluating One-Loop Amplitudes," *JHEP* **03** (2008) 003 [arXiv:0708.2398 [hep-ph]].

[207] W. T. Giele, Z. Kunszt and K. Melnikov, "Full one-loop amplitudes from tree amplitudes," *JHEP* **04** (2008) 049 [arXiv:0801.2237 [hep-ph]].

[208] R. K. Ellis, W. T. Giele, Z. Kunszt and K. Melnikov, "Masses, fermions and generalized D-dimensional unitarity," arXiv:0806.3467 [hep-ph].

[209] G. Ossola, C. G. Papadopoulos and R. Pittau, "Reducing full one-loop amplitudes to scalar integrals at the integrand level," *Nucl. Phys.* **B763** (2007) 147–169 [hep-ph/0609007].

[210] G. Ossola, C. G. Papadopoulos and R. Pittau, "On the Rational Terms of the one-loop amplitudes," *JHEP* **05** (2008) 004 [arXiv:0802.1876 [hep-ph]].

[211] P. Mastrolia, G. Ossola, C. G. Papadopoulos and R. Pittau, "Optimizing the Reduction of One-Loop Amplitudes," *JHEP* **06** (2008) 030 [arXiv:0803.3964 [hep-ph]].

[212] G. Ossola, C. G. Papadopoulos and R. Pittau, "CutTools: a program implementing the OPP reduction method to compute one-loop amplitudes," *JHEP* **03** (2008) 042 [arXiv:0711.3596 [hep-ph]].

[213] C. F. Berger *et. al.*, "An Automated Implementation of On-Shell Methods for One- Loop Amplitudes," *Phys. Rev.* **D78** (2008) 036003 [arXiv:0803.4180 [hep-ph]].

[214] W. T. Giele and G. Zanderighi, "On the Numerical Evaluation of One-Loop Amplitudes: The Gluonic Case," arXiv:0805.2152 [hep-ph].

[215] T. Binoth *et. al.*, "Precise predictions for LHC using a GOLEM," arXiv:0807.0605 [hep-ph].

[216] T. Gleisberg and F. Krauss, "Automating dipole subtraction for QCD NLO calculations," *Eur. Phys. J.* **C53** (2008) 501–523 [arXiv:0709.2881 [hep-ph]].

[217] M. H. Seymour and C. Tevlin, "TeVJet: A general framework for the calculation of jet observables in NLO QCD," arXiv:0803.2231 [hep-ph].

[218] K. Hasegawa, S. Moch and P. Uwer, "Automating dipole subtraction," *Nucl. Phys. Proc. Suppl.* **183** (2008) 268–273 [arXiv:0807.3701 [hep-ph]].

[219] H. Murayama, I. Watanabe and K. Hagiwara, "HELAS: HELicity amplitude subroutines for Feynman diagram evaluations,". KEK-91-11.

[220] Z. Nagy and Z. Trocsanyi, "Next-to-leading order calculation of four-jet observables in electron positron annihilation," *Phys. Rev.* **D59** (1999) 014020 [hep-ph/9806317].